Center for Theoretical Physics
of the Polish Academy of Sciences

Super-Tonks-Girardeau effect in the low-dimensional Bose gases with competing interactions

Author
Maciej Marciniak

Supervisor
Krzysztof Pawłowski
Associate Professor

Thesis submitted to the Center for Theoretical Physics of the Polish Academy of Sciences
in accordance with the requirements for the degree of Doctor of Philosophy in Physics

Warsaw, 2025

Streszczenie

Jednym z fundamentalnych osiągnięć mechaniki kwantowej było odkrycie bozonów i fermionów, charakteryzujących się wyraźnie odmiennymi właściwościami statystycznymi. Przez dziesięciolecia własności tych dwóch typów cząstek stanowiły punkt wyjścia dla rozwoju wielu obszarów fizyki. Jednym z interesujących rezultatów tych badań było odkrycie głębokiego podobieństwa pomiędzy silnie odpychającymi się bozonami a nieoddziałującymi fermionami w jednowymiarowych układach. W układach bozonowych obecność silnych oddziaływań sprawia, że dwie cząstki praktycznie nigdy nie mogą znajdować się w tym samym miejscu, co skutecznie imituje działanie zakazu Pauliego charakterystycznego dla fermionów. To formalne podobieństwo prowadzi do zgodności energii oraz funkcji korelacji drugiego rzędu obu typów układów, co stało się podstawą do określenia takich stanów mianem „sfermionizowanych". Co istotne, podobieństwo to występuje nie tylko w przypadku silnie odpychających się bozonów, ale również w pewnych wysoko wzbudzonych stanach układów o bardzo silnych przyciągających oddziaływaniach. Te wysoce nieintuicyjne stany nazwano stanami super-Tonksa-Girardeau. Ich istnienie zostało potwierdzone eksperymentalnie poprzez przygotowanie sfermionizowanego stanu bozonów, a następnie gwałtowną zmianę charakteru oddziaływań z silnie odpychających na silnie przyciągające. Eksperymenty te wykazały zaskakującą stabilność takich układów oraz ich odporność na termalizację. W niniejszej rozprawie przedstawiono teoretyczne podstawy tego zjawiska oraz omówiono możliwość jego wykorzystania w realizacji tzw. procesu pompowania, umożliwiającego generowanie w kontrolowany sposób stanów wysoko wzbudzonych. Szczególną uwagę poświęcono silnie skorelowanym stanom wzbudzonym doskonałego gazu bozonowego, w których właściwości układu wykazują uderzające podobieństwo do zachowania nieoddziałujących fermionów w modelach o zredukowanej długości. W odróżnieniu jednak od „klasycznej" fermionizacji, w tym przypadku podobieństwo dotyczy energii i rozkładu pędów, przy jednoczesnych istotnych różnicach w funkcjach korelacji drugiego rzędu. W dalszej części pracy przeanalizowano konsekwencje nagłych zmian oddziaływań w układach bozonowych, w których obecne są dwa konkurujące ze sobą typy oddziaływań: silnie odpychające kontaktowe oraz nielokalne przyciągające. Wykazano, że pojawiające się w takich systemach stany samozwiązane można podzielić na dwie klasy, różniące się zachowaniem po gwałtownej zmianie

oddziaływań: (i) w przypadku dostatecznie silnego nielokalnego przyciągania układ pozostaje stabilny, a wśród stanów własnych nowego hamiltonianu pojawia się stan super-Tonksa-Girardeau; (ii) istnieją również stany samozwiązane, które ulegają dezintegracji - w ich przypadku nie obserwuje się obecności stanu super-Tonksa-Girardeau. W rozprawie zastosowano szeroki wachlarz metod badawczych, ze szczególnym uwzględnieniem analitycznych narzędzi teorii układów wielociałowych (w tym Ansatzu Bethego) oraz obliczeń ab initio, takich jak nowoczesne metody numeryczne oparte na sieciach tensorowych oraz ścisłą diagonalizację z użyciem metody Lanczosa. Najważniejsze wyniki zaprezentowanych badań to

- identyfikacja stanów doskonałego gazu bozonowego, charakteryzujących się identycznym rozkładem pędów jak układ nieoddziałujących fermionów, możliwych do uzyskania poprzez proces pompowania,
- oraz wykazanie, że część stanów związanych w układach z oddziaływaniami dipolowymi nie posiada odpowiednika w postaci analogicznego stanu super-Tonksa-Girardeau i po skokowej zmianie oddziaływań ulega dezintegracji.

Abstract

One of the foundational achievements of quantum mechanics was the discovery that particles fall into two distinct categories - bosons and fermions - each governed by fundamentally different statistical laws. For decades, the properties of these two types of particles have served as a foundation for the development of numerous fields in physics. One of the intriguing outcomes of these investigations was the discovery of a deep similarity between strongly repulsive bosons and non-interacting fermions in one-dimensional systems. In bosonic systems, the presence of strong repulsive interactions effectively prevents two particles from occupying the same position, thereby mimicking the Pauli exclusion principle characteristic of fermions. This formal resemblance leads to agreement in both the energy and the second-order correlation functions of the two systems, forming the basis for the concept of “fermionized” states.

Noteworthy, this similarity arises not only in the case of strongly repulsive bosons, but also in certain highly excited states of systems with strongly attractive interactions. These counterintuitive states are known as super-Tonks-Girardeau states. Remarkably, their existence has been experimentally confirmed by first preparing a fermionized bosonic state, and then suddenly quenching the interaction character from strongly repulsive to strongly attractive. These experiments revealed a surprising stability of such systems, as well as their resistance to thermalization.

This thesis presents the theoretical foundations of this phenomenon and explores its potential application in realizing the so-called pumping process, which enables the controlled generation of highly excited states. Particular attention is given to strongly correlated excited states of an ideal Bose gas, in which the properties of a system exhibit striking similarities to those of non-interacting fermions in models with reduced length. In contrast to “classical” fermionization, however, the observed similarities obey the energy and momentum distribution, while significant differences remain in the second-order correlation functions.

In the second part of this thesis, the consequences of sudden changes in interaction strength are analyzed for bosonic systems featuring two competing types of interactions: strongly repulsive contact interactions and long-range attractive

ones. It is shown that self-bound states arising in such systems can be classified into two distinct types based on their behavior after the quench: (i) for sufficiently strong nonlocal attraction, the system remains stable, and among the eigenstates of the post-quench Hamiltonian, a super-Tonks-Girardeau-like state appears; (ii) there also exist self-bound states that disintegrate after the quench - in which case no super-Tonks-Girardeau state is observed.

Throughout this dissertation, a broad range of research methods is employed, with particular emphasis on analytical many-body methods (including the Bethe Ansatz), as well as ab initio numerical methods, including modern tensor network techniques and exact diagonalization using the Lanczos algorithm.

The key results of the projects presented here include

- the identification of states of an ideal Bose gas that exhibit the same momentum distribution as non-interacting fermions, which can be generated through a pumping process;
- and the demonstration that some of the bound states in systems with dipolar interactions do not have a counterpart in the form of an analogous super-Tonks-Girardeau state and disintegrate following a sudden change in interactions.

List of Publications

The present thesis is mostly based on one publication and one preprint

[1] **Maciej Marciniak**, Maciej Łebek, Jakub Kopyciński, Wojciech Górecki, Rafał Ołdziejewski and Krzysztof Pawłowski
Super-Tonks-Girardeau Quench in the Extended Bose-Hubbard Model
Physical Review A **108**, 043304 (2023)

[2] **Maciej Marciniak**, Grigori E. Astrakharchik, Krzysztof Pawłowski and Bruno Juliá-Díaz,
Fermionizing the ideal Bose gas via topological pumping,
arXiv: 2504.19569

During PhD studies the author contributed also to other publications

[3] Jakub Kopyciński, Maciej Łebek, **Maciej Marciniak**, Rafał Ołdziejewski, Wojciech Górecki Krzysztof Pawłowski
Beyond Gross-Pitaevskii equation for 1D gas: quasiparticles and solitons
SciPost Phys. **12**, 023, (2022)

[4] Buğra Tüzemen, **Maciej Marciniak**, Krzysztof Pawłowski
Diminished quantum depletion and correlated droplets in one-dimensional dipolar Bose gas
Physical Review Research Letter **7**, L012057, (2025).
Buğra Tüzemen and Maciej Marciniak contributed equally to this work.zo.

Podziękowania

Na pierwszym miejscu pragnę podziękować mojemu promotorowi, Profesorowi Krzysztofowi Pawłowskiemu. Moje doświadczenie z fizyką teoretyczną zaczęło się od studenckiego stażu pod Jego kierunkiem. Od tego momentu niemal wszystko, czego miałem okazję się nauczyć, wynikało z tej współpracy. Dziękuję za wytyczenie tej inspirującej ścieżki. Droga, którą dzięki niej przebyłem, była wspaniałą przygodą, która do końca życia będzie owocować i otwierać przede mną nowe szlaki. Dziękuję za bycie wymarzonym przewodnikiem!

Szczególne podziękowania kieruję w stronę dwóch wybitnych badaczy, Profesora Bruno Juliá-Díaz oraz Profesora Grigorija E. Astrakharchika, od których nauczyłem się bardzo wiele. Współpraca z nimi naprowadziła mnie na wiele nowych torów myślowych, których odkrywanie zajmie mi jeszcze wiele lat. Dziękuję za bilet wstępu do tego niezwykłego świata.

Dziękuję również moim kolegom — doktorowi Buğrze Tüzemen'owi, doktorowi Jakubowi Kopycińskiemu, doktorowi Maciejowi Łebkowi, doktorowi Wojciechowi Góreckiemu i doktorowi Rafałowi Ołdziejewskiemu — współpasażerom, którzy chętnie dzielili się wskazówkami, doświadczeniami i wiele razy ostrzegali mnie przed ślepymi zaułkami. Dziękuję za ciągłe uaktualnianie mojej mapy.

Dziękuję również wszystkim osobom, które tworzą wspaniałą atmosferę Centrum Fizyki Teoretycznej PAN, które dzielnie mierzą się z codzienną, pozornie syzyfową pracą pilnowania, bym ja i inni badacze nie zagubili się w gąszczu biurokracji.

Pragnę także podziękować Narodowemu Centrum Nauki za finansowanie moich badań w ramach grantu nr 2019/34/E/ST2/00289.

Chciałbym również wspomnieć, że podczas pisania niniejszej rozprawy korzystałem ze wsparcia modelu językowego ChatGPT w redakcji i korekcie tekstu. Jego twórcom również bardzo dziękuję.

Chciałbym złożyć serdeczne podziękowania generałowi i astronaucie Mirosławowi Hermaszewskiemu, który od najmłodszych lat był dla mnie Bohaterem i wzorem do naśladowania. Podczas naszego spotkania wiele lat temu powiedziałem Generałowi, że w przyszłości zostanę kosmonautą i będę odkrywać nowe planety. Co prawda,

plan na razie nie został jeszcze zrealizowany, ale mam nadzieję, że niniejszy doktorat w pewnym, choćby symbolicznym stopniu, spełnia złożoną wówczas obietnicę zostania odkrywcą. Panie Generale, tę misję obiecuję kontynuować do końca moich dni. Mam nadzieję, że kibicuje mi Pan tam z góry. Generale, pamiętam i dziękuję!

Wreszcie — z całego serca dziękuję moim Najbliższym. Szczególne podziękowania kieruję do moich Rodziców, którzy od najmłodszych lat wspierali mnie na wszelkie możliwe sposoby w dążeniu do kariery naukowej. Mojej Mamie — za troskę o mój rozwój intelektualny, za danie mi ogromnej swobody przy jednoczesnym wpajaniu zasad dyscypliny. Mojemu Tacie — za zaszczepienie we mnie pasji do nauki i miłości do książek science fiction. Mamo, Tato — dziękuję za wszystko.

I w końcu — dziękuję mojej ukochanej Żonie. Mam nadzieję, że kiedyś będę mógł odwdzięczyć się Jej takim samym wsparciem i zrozumieniem. Każde Jej słowo i każdy Jej uśmiech są dla mnie bezcenne. Kochanie, dziękuję.

Contents

List of Figures

Chapter 1

Introduction

The research presented in this dissertation focuses on bosonic systems that, under certain conditions, can exhibit fermionic characteristics. In the introduction, I first recall the fundamental properties of fermions and bosons, and then proceed to the interacting many-body systems consisting of particles in one dimensional geometries — the main focus of this work.

1.1 100 years of History of Fermions and Bosons

The History of quantum mechanics is commonly said to have begun in 1900, with Max Planck's proposal of energy quantization as a way to explain the puzzling behavior of black-body radiation [1]. This moment marked the birth of what would become known as the Old Quantum Theory — a period marked by a flood of new ideas, many of which were not yet fully developed or understood, but which would later form the foundation of entire scientific and technological fields.

Among the most significant achievements of that era were the investigations of the statistical properties of photons carried out by Satyendra Nath Bose. His work [2], later extended by Albert Einstein, led to the concept of indistinguishable particles and the discovery of bosons. Another major breakthrough was Wolfgang Pauli's derivation of the exclusion principle, published exactly 100 years ago in [3], proposed to explain the curious patterns in electron shell occupation in atoms. This principle ultimately led to the formal identification of fermions.

The existence of these two types of particles — bosons and fermions — so similar and yet fundamentally different, appears to influence nearly every domain of physics.

This seemingly simple mathematical distinction introduces a kind of discontinuity — a "defect" in an otherwise elegant crystalline structure of physical laws. The far reaching consequences of this subtle difference appear in a wide range of fields, from the Standard Model and string theory to the pure quantum many-body theory.

The difference between fermions and bosons is perhaps most naturally explained through the lens of the many-body wavefunction — the central object in the Schrödinger equation [4, 5] — which essentially describes an amplitude of the probability of observing a particular configuration of particles

$$\Psi(r_1, r_2, \ldots, r_N) \tag{1.1}$$

where variables $\{r_j\}$ are the spatial positions of the particles. This function can be used to compute physically measurable quantities — called *observables* — through the application of appropriate operators $\hat{O}$, the contribution of Werner Heisenberg, Max Born, and Pascual Jordan for the foundations of quantum mechanics

$$\text{Physical observable } \mathcal{O} = \int \Psi^*(r_1, r_2, \ldots, r_N)\, \hat{O}\, \Psi(r_1, r_2, \ldots, r_N)\, \mathrm{dr_1 dr_2 \ldots dr_N}. \tag{1.2}$$

If the particles are indistinguishable, then swapping them must not alter any measurable physical quantity. In particular, the expected value of any operator must remain unchanged under exchange. This implies that as a result of swapping two particles the wavefunction can only acquire a global phase

$$\Psi(\ldots, r_i, \ldots, r_j, \ldots) = e^{i\varphi}\Psi(\ldots, r_j, \ldots, r_i, \ldots). \tag{1.3}$$

This simple rule appears to be relatively straightforward — at least as long as no two particles occupy the same position. However, if, for example, the positions of the i-th and j-th particles coincide $r_i = r_j$, a natural question arises: what happens if we perform the exchange operation twice? This leads to a relatively simple equation (1.4), yet one that carries far-reaching consequences

$$\Psi(\ldots, r_i, \ldots, r_j, \ldots) = e^{i\varphi}e^{i\varphi}\Psi(\ldots, r_i, \ldots, r_j, \ldots). \tag{1.4}$$

As one can see there $e^{2i\varphi} = 1$, and thus $e^{i\varphi} = \pm 1$. The case where $e^{i\varphi} = +1$ corresponds to a symmetric wavefunction, characteristic of bosons, while the other one implies antisymmetry typical for fermions. Antisymmetry has a profound consequence — namely, in the state discussed here $\Psi(\ldots, r_i, \ldots, r_j, \ldots) = -\Psi(\ldots, r_i, \ldots, r_j, \ldots)$, what implies that $\Psi(\ldots, r_i, \ldots, r_j, \ldots) = 0$. Consequently, as can be simply proven, no two indistinguishable fermions can occupy the same quantum state.

These considerations form a natural basis for further developments, such as the derivation of the *Bose-Einstein* and *Fermi-Dirac* statistical distributions, which describe the population of quantum states. They also underpin phenomena such as Bose-Einstein condensation and a wide range of other effects — many of which, while fascinating, lie beyond the scope of this particular work.

1.2 Theoretical approaches to one-dimensional bosonic systems

In the following decades, research on many-body systems continued. Among other efforts, numerous researchers proposed dozens of approaches to determine the exact form of the wavefunction for interacting bosons, along with key properties such as their associated energies. Particularly noteworthy in this context are the late 1950s and early 1960s — a period when the modern approach to many-body systems began to take shape, laying the foundations for the main currents of contemporary research in the field.

In chronological order, probably the first truly visionary approach to interacting quantum many-body systems was introduced by R. Jastrow in [6], where the author — building on earlier, not fully formalized suggestions by N. F. Mott and the work of R. B. Dingle [7] — proposed the so-called Jastrow Ansatz for the approximate description of systems of fermions and strongly interacting bosons. It is worth noting that this approach later became the foundation for one of the most widely used computational techniques today: variational Monte Carlo [8, 9]. A few years later, a somewhat similar approach, this time rooted in certain properties of the Bose-Einstein condensate (BEC), was independently developed in the works [10, 11], where the authors introduced what would later be known as the Gross–Pitaevskii equation — an effective, approximate framework for describing systems of weakly interacting bosons.

However, for our further discussion, two subsequent works are of particular importance — both of which consider a simplified case of N indistinguishable bosons of mass m, where the space is reduced to **one dimension** and the corresponding Hamiltonian is given by

$$\hat{H} = -\frac{\hbar^2}{2m}\sum_{j}^{N}\frac{\partial^2}{\partial x_j^2} + \sum_{j<j'}^{N} V(x_j - x_{j'}), \tag{1.5}$$

where x_j is the spatial position of the j-th particle and interaction potentials are given by $V(x - x')$.

The first is of M. Girardeau [12], in which author highlights an intriguing similarity between systems of strongly repulsive bosons, where interatomic interactions exhibit "impenetrable core" (i.e. $\int_{-\epsilon}^{\epsilon} V(x)\mathrm{dx} \rightarrow \infty$ for $\rho\epsilon < 1$ where ρ is the one-dimensional gas density) and the ground states of a systems of noninteracting fermions. As shown earlier in the context of the antisymmetry of the many-fermion wavefunction, two fermions cannot occupy the same position in space. Interestingly, bosonic systems with very strong short-range repulsive interactions (so-called *Tonks-Girardeau states*) exhibit a similar property. This resemblance leads to a number of shared features between the two types of systems. For instance, their energies are identical. Likewise, correlations that depend on the modulus of the wavefunction ($\Psi_{TG,B} = |\Psi_{GS,F}|$) are also the same in both cases. These considerations — providing an exact wavefunction for at least one value of the interaction parameter — represented the first step on the ladder.

Shortly afterwards, the breakthrough came with the works of E.H. Lieb and W. Liniger [13, 14], in which the authors brilliantly extended the method previously known as the Bethe Ansatz [15] to derive the exact wavefunction of a system of an arbitrary number of bosons interacting via repulsive contact forces of arbitrary strength, where the interatomic potential is given by $V(x - x') = g\delta(x - x')$, where $g > 0$ is called as a coupling constant. The model they solved — later named after them — belongs to the rare class of many-body quantum models considered exactly solvable.

I would like to conclude this generation of research with the final work in chronological order: [16], in which the author — J. B. McGuire — proposed the form of the wavefunction and the energies of certain eigenstates for a model identical to that of Lieb and Liniger, but involving attractive interactions ($g < 0$.

Finally, a third wave of discoveries emerged nearly four decades later. In 2005 a remarkable publication by G.E. Astrakharchik appeared [17], in which the author made a highly creative observation: the wavefunction of a bosonic system must coincide with the modulus of the fermionic wavefunction not only in the case of infinitely strong repulsive contact interactions (as it was in Tonks-Girardeau state) but also in the case of infinitely strong attractive interactions. In the latter scenario, where the ground state is given by the McGuire soliton, this correspondence holds

for a highly excited *super-Tonks-Girardeau state*, which nevertheless remains an eigenstate of the Hamiltonian.

This means that, theoretically, in one dimensional space, one could prepare a system of strongly repulsive bosons, suddenly switch the sign of the interaction to strong attraction, and — provided the post-quench attraction is sufficiently strong — the system would remain essentially unchanged for a long time, avoiding rapid thermalization [18, 19, 20, 21] and the associated collapse [22]. Counterintuitively, numerical predictions indicated that for relatively weak attractive interactions, such a system becomes unstable.

The work mentioned above plays the important role in this work: along with several follow-up studies that further developed the idea and clarified certain properties of the observed states [23, 24, 25, 26, 27, 28], will serve as a crucial starting point for my own investigations.

1.3 Experimental realization of ultracold many-body bosonic systems in low-dimensional geometries

First, however, I need to make a substantial leap and at least briefly outline the history of experimental research on strongly interacting bosons in reduced dimensions.

The first project that needs to be presented in this brief review is the one described in [29]. In this work, the authors used trapping techniques [30, 29] to create a very deep two-dimensional lattice, what resulted in the formation of an array of thousands of quasi-one-dimensional traps populated with atoms reproducing the bosonic characteristics. Later, experiments have been continuously conducted at several research centers [31], leading to, among other achievements, the experimental realization of states predicted in theoretical studies of Tonks–Girardeau gases [32, 33], the confinement of atoms in ring-shaped traps that naturally implement periodic boundary conditions [34], and the observation of prethermalization phenomena [35].

Finally, this remarkably rapid era of experimental testing of fundamental laws in one-dimensional systems — especially from the perspective of super-Tonks–Girardeau gases — was brought to a close in 2009, by the experiment [36]. In that beautiful study, the authors prepared a system of strongly repulsive

bosons, performed an interaction quench, and confirmed the existence of a stable super-TG phase. Crucially, when the interaction strength was gradually reduced from strongly attractive to moderately attractive values they also observed the collapse of the gas.

At that stage, it appeared that the nature of the super-Tonks–Girardeau states had been conclusively understood, with experimental observations showing excellent agreement with numerical simulations. However, later studies demonstrated that the collapse, previously considered a limiting factor, can in fact be mitigated under relatively accessible conditions.

A clue pointing to this can be found in a relatively recent experiment conducted by a research group from Stanford. The involved researchers lead by B. Lev performed a similar quench experiment involving ultracold atoms in a quasi-one-dimensional trap. Since 2009, however, there has been significant technological progress — researchers have learned not only how to trap and study atoms interacting via short-range forces, but also those with non-zero, strong dipole moments that can interact both via contact and non-local dipolar interactions [37, 38, 39, 40]. These new technical capabilities have enabled the exploration of more complex models. The aforementioned researchers took advantage of this progress, extending their study beyond purely contact interactions to include weak, seemingly negligible non-local repulsion as well.

As a result, despite the breaking of the system's integrability, the setup became sufficiently stable to avoid collapse during the transition from strongly attractive to intermediate interaction regimes and researchers were able to complete a full cycle: after the quench, they successfully returned adiabatically to a non-interacting atomic system, avoiding collapse and ultimately producing highly excited, intriguing quantum states. What must be highlighted, this experiment was not just a one-off success. In the following years, the same team conducted a series of similar experiments, gradually investigating various properties of the states to which they had suddenly gained access [41, 42].

1.4 Motivation

The experiments discussed in the previous section served as the primary motivation for two projects originating this dissertation. The further project — presented in

Chapter 3 — aimed to clarify the theoretical foundations of the pumping process reported in Ref. [43] and to explore the properties of the involved quantum states.

The latter focused more on non-local interactions and was closely related to a parallel line of research within our team, namely the study of phases of matter emerging in systems with coexisting contact and dipolar interactions. Its goal was to investigate how the super-Tonks-Girardeau quench influences self-bound quantum structures, such as quantum droplets.

Additionally, in a somewhat unexpected way, experiments with dipolar gases has a large impact on the choice of research methods used in this work: over the decades, a variety of approximate techniques have been developed to describe many-body bosonic systems — such as the previously mentioned Jastrow Ansatz or the Gross–Pitaevskii equation. These methods worked remarkably well in systems with only one type of short-range interactions.

However, it turned out that even a small modification — for example, introducing weak long-range interactions — could reveal phenomena that these established methods failed to predict. For instance, in the conventional condensate theory described by the "classical" GP equation, only two phases are typically allowed: uniform gas or a bright soliton [44]. But in reality, other exotic structures appear — sometimes considered a new phase of matter — such as quantum droplets [45, 46, 47, 48, 49, 50].

Although earlier approximate approaches were modified to account for the known effects of non-local interactions [45, 51, 52], the experience underscored the importance of caution. Given the delicate nature of the processes under investigation, we prefer the use of exact analytical methods wherever possible. In cases where this was not feasible, we turned to ab initio numerical techniques that rested on the fewest possible assumptions. Only upon this solid foundation we construct further approximations, consistently benchmarking their outcomes against predictions derived from the most robust theoretical frameworks available.

Chapter 2

Mathematical formalism and numerical methods

In the course of investigating the phenomena central to this work, I employed several numerical techniques, which are briefly outlined in the following sections. Some of these methods are not directly aligned with the mathematical formalism used in the main body of the discussion: for example, while the theoretical analysis is primarily conducted using the first-quantized representation and Bethe Ansatz framework, the numerical calculations rely on a second-quantized formalism. Therefore, the methods presented below are preceded by a concise introduction to the mathematical tools on which they are based.

2.1 Plane wave expansion

To explore the properties of few-body quantum systems that are intractable by analytical methods, this work among other numerical methods employs so-called *plane wave expansion*. Although this term does not fully reflect the complexity of the problem and, strictly speaking, refers only to the initial stage of the entire process, it will be used here to denote a broader computational procedure comprising three main stages: (i) reformulating the problem within the second-quantized formalism; (ii) efficiently constructing the Hamiltonian matrix and numerically computing a specified number of its eigenstates; and (iii) extracting the desired physical information from the obtained eigenstates. The following sections briefly outline each of these steps. I would like to highlight, that the following introductions obey the one-dimensional system.

1 Second quantization

The method described above is closely related to the second-quantized formalism, and the introduction will be conducted within this framework. Therefore, before presenting the technique itself, I briefly introduce the key concepts arising in this formalism. Second quantization can be naturally introduced by examining the structure and properties of the many-body wavefunction. As is well known, any single-particle wavefunction in the position (or, equivalently, momentum) representation can be expanded as

$$\Psi(x) = \sum_j c_j \, \varphi_j(x), \tag{2.1}$$

where c_j are the expansion coefficients and functions in $\{\varphi_j(x)\}$ span a complete orthonormal basis. In the case of many-body systems (i.e. wavefunctions depending on multiple coordinates), an analogous expansion can be carried out

$$\Psi(x_1, x_2, \ldots, x_N) = \sum_{\mathbf{j}} c_{\mathbf{j}} \, \Phi_{\mathbf{j}}(x_1, x_2, \ldots, x_N), \tag{2.2}$$

where, analogously, the set $\{\Phi_{\mathbf{j}}(x_1, x_2, \ldots, x_N)\}$ must form a complete basis for the N-particle Hilbert space, and the sum runs over multi-index $\mathbf{j}$. Notably, the multi-index $\mathbf{j}$ may include repeated values, corresponding to multiple occupations of the same single-particle orbital.

At this point, it is common to introduce a simplification based on particle indistinguishability. Since the wavefunction describing identical bosons must be symmetric under particle exchange, it is convenient to choose basis functions with the same symmetry. A typical choice is the symmetrized basis, given by the permanent of a matrix composed of single-particle orbitals

$$\Phi_{\mathbf{j}}(x_1, x_2, \ldots, x_N) = \mathcal{N} \operatorname{perm} \begin{bmatrix} \varphi_{\mathbf{j}_1}(x_1) & \varphi_{\mathbf{j}_1}(x_2) & \cdots & \varphi_{\mathbf{j}_1}(x_N) \\ \varphi_{\mathbf{j}_2}(x_1) & \varphi_{\mathbf{j}_2}(x_2) & \cdots & \varphi_{\mathbf{j}_2}(x_N) \\ \vdots & \vdots & \ddots & \vdots \\ \varphi_{\mathbf{j}_N}(x_1) & \varphi_{\mathbf{j}_N}(x_2) & \cdots & \varphi_{\mathbf{j}_N}(x_N) \end{bmatrix}, \tag{2.3}$$

where $\mathcal{N}$ is the normalization factor.

Fock states

A closer analysis of such symmetrized wavefunctions reveals an important insight: what truly matters is how many particles occupy each single-particle orbital. This

observation motivates the introduction of the so-called Fock states, which are labeled by the occupation numbers

$$|n_0, n_1, n_2, \dots\rangle. \tag{2.4}$$

In this notation, the number n_j indicates how many particles occupy the j-th single particle orbital.

Together with Fock states, it is necessary to introduce the bosonic creation and annihilation operators, $\hat{b}_j^\dagger$ and $\hat{b}_j$, which respectively create or annihilate a particle in the j-th orbital, following the relation

$$\hat{b}_j|n_0, n_1, \dots, n_j, \dots\rangle = \sqrt{n_j}\,|n_0, n_1, \dots, n_j - 1, \dots\rangle \tag{2.5}$$

$$\hat{b}_j^\dagger|n_0, n_1, \dots, n_j, \dots\rangle = \sqrt{n_j + 1}\,|n_0, n_1, \dots, n_j + 1, \dots\rangle. \tag{2.6}$$

For bosons, these operators satisfy the canonical commutation relations

$$[\hat{b}_j, \hat{b}_{j'}^\dagger] = \delta_{j,j'}. \tag{2.7}$$

Finally, any Fock state can be constructed from the vacuum state $|\text{vac}\rangle$ (containing no particles) by successive application of creation operators

$$|n_0, n_1, \dots\rangle = \prod_j \frac{(\hat{b}_j^\dagger)^{n_j}}{\sqrt{n_j!}}|\text{vac}\rangle. \tag{2.8}$$

Quantum field operators

The exact connection between first and second quantization can be most clearly illustrated by introducing the so-called quantum field operators: the annihilation operator $\hat{\Psi}(x)$ and the creation operator $\hat{\Psi}^\dagger(x)$, defined as

$$\hat{\Psi}(x) = \sum_j \varphi_j(x)\,\hat{b}_j, \quad \hat{\Psi}^\dagger(x) = \sum_j \varphi_j^*(x)\,\hat{b}_j^\dagger, \tag{2.9}$$

where $\{\varphi_j(x)\}$ form a complete single-particle basis, and $\hat{b}_j$, $\hat{b}_j^\dagger$ are the bosonic annihilation and creation operators associated with the j-th orbital. These field operators carry a natural physical interpretation: $\hat{\Psi}(x)$ annihilates, while $\hat{\Psi}^\dagger(x)$ creates a particle at position x. The commutation relation between these operators is given by $[\hat{\Psi}(x), \hat{\Psi}^\dagger(x')] = \delta(x - x')$.

Within this formalism, a first-quantized, spatial (coordinate) wavefunction — which gives the amplitude for finding particles at specific positions — can be extracted from a second-quantized, many-body Fock state via the following procedure

$$\Psi(x_1, x_2, \dots, x_N) \propto \langle\text{vac}|\,\hat{\Psi}(x_1)\hat{\Psi}(x_2)\cdots\hat{\Psi}(x_N)\,|n_0, n_1, \dots, n_M\rangle\,. \tag{2.10}$$

Finally, utilizing introduced formalism one can simply transform the Schrödinger equation — originally expressed as a complex differential equation — into an equivalent, but more tractable, problem: the numerical diagonalization of a Hamiltonian matrix within a chosen Fock basis.

Hamiltonian matrix

To lay the ground for this procedure, I will first introduce the general form of the many-body Hamiltonian that will be analyzed in the subsequent chapters. In the position-space representation, this operator takes the form

$$\hat{H} = -\frac{\hbar^2}{2m}\sum_{j=1}^{N}\frac{\partial^2}{\partial x_j^2} + \sum_{j<j'}^{N} V(x_j - x_{j'}), \tag{2.11}$$

where $\hbar$ is the Dirac constant, m is the particle mass and $V(x_j - x_{j'})$ stands for the interaction potential between particles.

This differential operator plays the central role int the quantum mechanics. It governs the time evolution of quantum systems, as the wavefunction must satisfy the Schrödinger equation

$$i\hbar\frac{d\Psi(t, x_1, ..., x_N)}{dt} = \hat{H}\Psi(t, x_1, ..., x_N), \tag{2.12}$$

it defines the mean energy of quantum states

$$E = \langle\hat{H}\rangle = \int \mathrm{d}x_1 \ldots \mathrm{d}x_N, \Psi^*(x_1, \ldots, x_N)\hat{H}\Psi(x_1, \ldots, x_N), \tag{2.13}$$

and, through the time-independent Schrödinger equation, determines the stationary states of the system.

The procedure of transforming the Hamiltonian into its matrix representation involves constructing an object of the form presented in Eq. (2.14)

$$\hat{H} = \begin{bmatrix} H_{\mathbf{11}} & H_{\mathbf{12}} & H_{\mathbf{13}} & \ldots \\ H_{\mathbf{21}} & H_{\mathbf{22}} & H_{\mathbf{23}} & \ldots \\ H_{\mathbf{31}} & H_{\mathbf{32}} & H_{\mathbf{33}} & \ldots \\ \vdots & \vdots & \vdots & \ddots \end{bmatrix}, \tag{2.14}$$

where the matrix elements are given by

$$H_{\mathbf{jk}} = \int_{-\infty}^{\infty} dx_1 \ldots dx_N \, \phi^*_{\mathbf{j}}(x_1, x_2, \ldots, x_N) \, \hat{H} \, \phi_{\mathbf{k}}(x_1, x_2, \ldots, x_N) = \langle \mathbf{j} | \, \hat{H} \, | \mathbf{k} \rangle \, . \tag{2.15}$$

As can be shown, the eigenvectors of this Hamiltonian matrix correspond to the coefficients of the eigenfunctions of $\hat{H}$ expressed in the chosen basis. That is,

$$\hat{H} = VDV^{-1}, \tag{2.16}$$

where D is a diagonal matrix containing the eigenvalues (energies) E_n, and V is a matrix whose columns are the eigenvectors

$$\hat{H}\,\vec{v}_n = E_n\,\vec{v}_n. \tag{2.17}$$

Although the procedure for constructing the Hamiltonian matrix outlined above is conceptually straightforward, it becomes computationally expensive as the system size grows. A more efficient and general approach exploits the symmetries of the system and employs the formalism of quantum field operators.

Specifically, by making use of the indistinguishability of particles and the algebra of field operators, the Hamiltonian can be expressed in second quantized form. This involves decomposing the Hamiltonian into parts corresponding to single-particle and two-particle processes (and also higher-order processes if needed, i.e., in the case of Hamiltonian including three-particle terms).

In the system of interest, we observe the single-particle "processes" represented by the kinetic energy term

$$\hat{H}_K = -\frac{\hbar^2}{2m}\sum_{j=1}^{N}\frac{\partial^2}{\partial x_j^2}, \tag{2.18}$$

and two-particle processes arising from interatomic interactions

$$\hat{H}_V = \frac{1}{2}\sum_{j,j'=1}^{N} V(x_j - x_{j'}). \tag{2.19}$$

By using the field operators $\hat{\Psi}(x)$ and $\hat{\Psi}^\dagger(x)$, these terms can be rewritten in second quantized form as

$$\hat{K} = -\frac{\hbar^2}{2m}\int_{\mathcal{S}} \mathrm{dx}\ \hat{\Psi}^\dagger(x)\frac{\partial^2}{\partial x^2}\hat{\Psi}(x), \tag{2.20}$$

and

$$\hat{V} = \int_{\mathcal{S}} \mathrm{dx}\ \ \mathrm{dx}\,'\,\hat{\Psi}^\dagger(x)\hat{\Psi}^\dagger(x')V(x-x')\hat{\Psi}(x')\hat{\Psi}(x), \tag{2.21}$$

where $\mathcal{S}$ denotes the full spatial domain of the system. These operator expressions serve as the starting point for constructing the many-body Hamiltonian matrix directly in the Fock basis, making numerical implementation far more efficient and scalable.

2 Single particle basis

At the latest, at this point we encounter a fundamental question: which single-particle orbital basis should we choose? In practice, a common strategy is to select a basis such that at least one part of the Hamiltonian matrix becomes diagonal. This is often achieved by choosing the eigenfunctions of the single-particle component of the full Hamiltonian. For example, in a system where particles are confined in a harmonic potential with the single-particle Hamiltonian given by

$$\hat{H}_{\text{h.o.}} = -\frac{\hbar^2}{2m}\frac{d^2}{dx^2} + \frac{1}{2}m\omega^2 x^2, \tag{2.22}$$

an appropriate choice of basis would be the eigenfunctions of the harmonic oscillator

$$\varphi_{j,\text{h.o.}}(x) = \mathcal{N}\, e^{-\frac{m\omega x^2}{2\hbar}} H_j\left(\sqrt{\frac{m\omega}{\hbar}}x\right), \tag{2.23}$$

where H_j denotes the j-th Hermite polynomial and $\mathcal{N}$ is a normalization constant.

In the case more relevant to our studies — namely, a system of particles confined in a box with periodic boundary conditions — it is optimal to use plane wave eigenstates of the kinetic energy operator

$$\varphi_j(x) = \frac{1}{\sqrt{L}} e^{i\frac{2\pi j}{L}x}. \tag{2.24}$$

Applying such states ensures that the kinetic part of the Hamiltonian is represented by a diagonal matrix and automatically enforces the periodic boundary conditions (PBC) on the wavefunction.

Conservation of the total momentum

The chosen basis has another significant advantage: the single-particle orbitals are eigenstates of the momentum operator, meaning they possess precisely defined momenta. As a result, the many-body basis states constructed from them also have well-defined total momentum. Since the total Hamiltonian does not contain any terms that change the total momentum of the system, it commutes with the total momentum operator. Without delving into the mathematical formalism, this implies that the Hamiltonian matrix will be sparse.

This feature becomes especially apparent when computing the Hamiltonian matrix elements. In chosen *momentum* basis, the kinetic and interaction parts of the

Hamiltonian given in Eq. 2.20 take the forms

$$\begin{aligned}\hat{K} &= -\frac{\hbar^2}{2m}\int_{\mathcal{S}} dx\, \hat{\Psi}^\dagger(x)\frac{\partial^2}{\partial x^2}\hat{\Psi}(x) = \frac{\hbar^2}{2mL}\sum_{j,j'}\left(\frac{2\pi j'}{L}\right)^2 \int_0^L dx\, e^{i\frac{2\pi(j'-j)}{L}x}\hat{b}_j^\dagger \hat{b}_{j'} \\ &= \sum_j \frac{2\pi^2\hbar^2 j^2}{mL^2}\hat{n}_j = \sum_j K_j \hat{n}_j,\end{aligned} \tag{2.25}$$

and

$$\begin{aligned}\hat{V} &= \frac{1}{2}\int_0^L dx \int_0^L dx'\, \hat{\Psi}^\dagger(x)\hat{\Psi}^\dagger(x')V(x-x')\hat{\Psi}(x')\hat{\Psi}(x) \\ &= \frac{1}{2L}\sum_{p',q',q,p}\hat{b}_{p'}^\dagger \hat{b}_{q'}^\dagger \hat{b}_q \hat{b}_p \iint_{-L/2}^{L/2} dx\, dx'\, e^{i\frac{2\pi}{L}\left((p-p')x+(q-q')x'\right)}V(x-x').\end{aligned} \tag{2.26}$$

where $\hat{n}_j = \hat{b}_j^\dagger \hat{b}_j$ is the occupation operator. As expected, the kinetic energy operator is diagonal in that basis. The interaction term, however, has a more complex structure. Fortunately, due to the conservation of total momentum, two-particle scattering processes must conserve the overall momentum (mathematically, this manifests through the fact that the exponential integral $\int_{-L/2}^{L/2} e^{i\frac{2\pi}{L}jx}dx$ is nonzero only for $j=0$). This constraint simplifies the interaction term and allow us to write it as

$$\hat{V} = \frac{1}{2L}\sum_{q,p}\sum_k \hat{b}_{p-k}^\dagger \hat{b}_{q+k}^\dagger \hat{b}_q \hat{b}_p \iint_{-L/2}^{L/2} dx\, dx'\, e^{i\frac{2\pi}{L}k(x-x')}V(x-x') = \frac{1}{2}\sum_{k,k',q} V_q\, \hat{b}_{k+q}^\dagger \hat{b}_{k'-q}^\dagger \hat{b}_{k'}\hat{b}_k, \tag{2.27}$$

where $V_q = \frac{1}{L}\int_{-L/2}^{L/2} dx \int_{-L/2}^{L/2} dx'\, e^{i\frac{2\pi}{L}q(x-x')}V(x-x')$ is the Fourier transform of the interaction potential. Before proceeding further, it is useful to take a second look at the last term in Eq. (2.27). Its interpretation is as follows: the interaction occurs between two particles, initially occupying the k-th and k'-th orbitals. As a result of the interaction, the particles undergo scattering and are transferred to new orbitals, namely the $(k+q)$-th and $(k'-q)$-th, respectively. The apparent asymmetry in the final states is not an issue. Since the summation runs over all possible values of the initial orbitals k and k', the Hamiltonian accounts for scattering into all possible final states.

Importantly, the coefficient V_q can be interpreted as a transition amplitude that determines how frequently particles scatter into orbitals shifted by q from their initial positions. The larger the absolute value of V_q, the higher the probability that the scattering process will result in a transition to a given final state. Another key point is that the scattering amplitude depends only on the displacement q, not on the specific initial orbitals. This implies that the "probability" of scattering from

$k = 0$, $k' = 4$ to $k = -1$, $k' = 5$ is identical to the "probability" of scattering from $k = 100$, $k' = 104$ to $k = 99$, $k' = 105$.

Orbital cutoff

Another important aspect related to the diagonalization method described above is the necessity of choosing an appropriate size for the computational basis. As can be easily demonstrated, a plane wave basis, in order to be considered complete, must include an infinite number of orbitals. Naturally, such a condition cannot be fulfilled in numerical simulations. Therefore, it becomes necessary to introduce a cutoff by selecting a maximal orbital function $\varphi_{k_{max}}(x)$ beyond which no further basis states are considered. This is equivalent to assuming that all higher-energy orbitals have zero occupation.

Fortunately, as long as we are primarily interested in the ground state and low-energy excitations, even for relatively small cutoffs k_{max} this truncation does not lead to significant discrepancies from physical reality. It can be shown that orbitals with high indices correspond to high kinetic energies. Consequently, the probability of particle occupation in such high-energy orbitals is very low.

An example of how the ground state energy varies with the orbital cutoff for systems composed of two and three particles in one dimensional PBC box of the length L, interacting via a Dirac delta potential $V(x - x') = g\delta(x - x')$ is illustrated in Fig. 2.1.

Effective interatomic potential

A closer analysis of Fig. 2.1(c,d) reveals an adverse tendency: as the number of particles increases, the required cutoff k_{max} also grows, resulting in a rapid growth of the Hilbert space required to perform the calculations. This behavior is strongly tied to the nature of the used interaction potential. To better understand the source of this issue, let us consider the Fourier transform of the potential shown in Fig. 2.2(a). As seen in the figure, the Fourier transform of a Dirac delta function is a uniform distribution in the momentum representation. This implies that scattering events between particles interacting via such a potential can populate single-particle states with arbitrarily high energies — particles initially occupying low-energy orbitals (e.g. $k = k' = 0$) can scatter with equal probability into final states such as $k = 1$, $k' = -1$ and $k = 100$, $k' = -100$. Consequently, accurately capturing the physics of such systems requires a very high orbital cutoff.

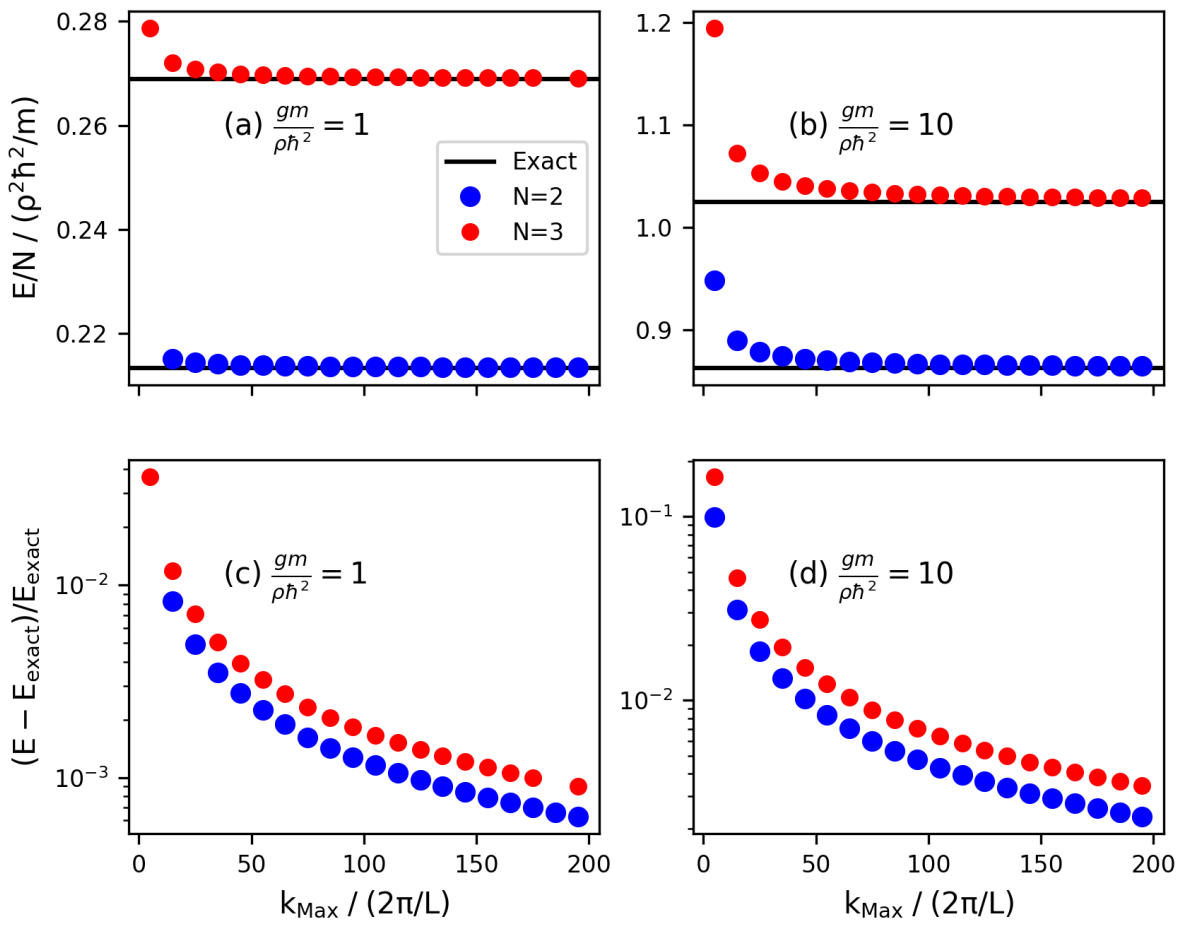

Figure 2.1: (a,b) Ground state energy of a system of with $N = 2, 3$ particles interacting via a Dirac delta potential $V(x - x') = g\delta(x - x')$, confined in a box with periodic boundary conditions, as a function of the orbital cutoff (i.e., the maximum single-particle orbital allowed to be occupied). (c,d) Comparison between the numerically obtained energy and the exact analytical result. Here, $\rho = N/L$ is the one-dimensional gas density.

To mitigate this issue and accelerate computations, the Dirac delta potential can be replaced by a narrow Gaussian function $V(x-x') = g\frac{1}{\sigma\sqrt{2\pi}}e^{-\frac{(x-x')^2}{2\sigma^2}}$. This modification significantly restricts the range of scattering processes (see Fig. 2.2(a)), allowing for a substantial reduction in the size of the computational basis. Importantly, this substitution does not noticeably alter the structure of the wavefunctions or the energies of the states of interest (see Fig. 2.2(b)).

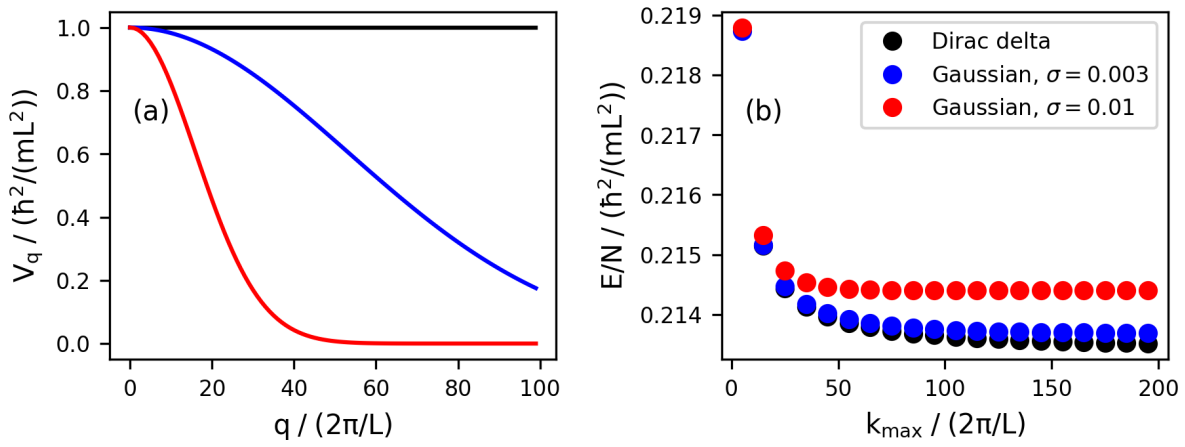

Figure 2.2: (a) Fourier transforms of two types of potentials used to model contact interactions. As shown, the Fourier transform of the Dirac delta function is a uniform distribution, whereas the Fourier transform of a Gaussian function in position space is a Gaussian in momentum space. (b) Comparison of ground state energies for systems with different interaction types as a function of orbital cutoff. It can be observed that the energy converges more rapidly when Gaussian potentials are used.

3 Diagonalization methods and Lanczos algorithm

After constructing the Hamiltonian matrix, the next step is to determine its eigenstates. This can be achieved using well-established, highly optimized, and parallelizable exact diagonalization methods, which are particularly effective for small and dense matrices. Alternatively, in the case of sparse matrices, it is advantageous to employ approximate techniques such as the Arnoldi or Lanczos algorithms [53, 54]. The aforementioned Lanczos approach is an iterative method that can be used to effectively approximate a few largest or smallest eigenvalues and corresponding eigenvectors of hermitian matrices. In the numerical computations underlying the results presented in the following chapter, I employ that approach, whose key principles are briefly outlined below.

Particularly, given a Hermitian matrix H and a starting normalized vector v_1, the Lanczos algorithm constructs an orthonormal basis $\{v_1, v_2, \ldots, v_m\}$ of the Krylov subspace

$$\mathcal{K}_m(H, v_1) = \text{span}\{v_1, Hv_1, H^2v_1, \ldots, H^{m-1}v_1\}. \tag{2.28}$$

Within this subspace, the matrix H is projected onto a much smaller $m \times m$ tridiagonal matrix T_m, whose eigenvalues approximate those of H. The iterative procedure generates the basis vectors and tridiagonal matrix elements using the recurrence relations

$$\begin{aligned} \beta_{j+1} v_{j+1} &= H v_j - \alpha_j v_j - \beta_j v_{j-1}, \\ \alpha_j &= \langle v_j | H | v_j \rangle, \\ \beta_{j+1} &= \| H v_j - \alpha_j v_j - \beta_j v_{j-1} \|, \end{aligned} \tag{2.29}$$

with initial conditions $v_0 = 0$, $\beta_1 = 0$, and v_1 chosen as an arbitrary normalized vector. The resulting tridiagonal matrix T_m can then be diagonalized using standard methods dedicated to that type of matrices. Its eigenvalues provide approximations to the extreme eigenvalues of H, and the eigenvectors can be used to reconstruct approximations to the eigenvectors of H in the original space. What need to be highlighted, the approximations are the better the more iterative steps were done and, subsequently, the larger is the tridiagonal matrix (see Fig. 2.3).

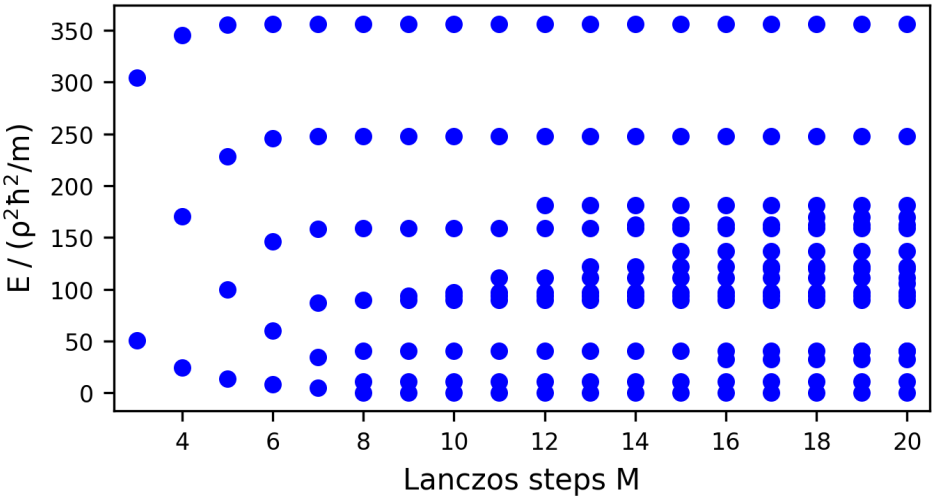

Figure 2.3: Distribution of energies obtained via diagonalization using the Lanczos algorithm, shown as a function of the number of Lanczos steps M.

4 Correlation functions

Given an eigenvector of the Hamiltonian, one can straightforwardly extract various physical properties of the system. Of particular importance are the second-order correlation functions, defined as

$$G_2(x, x') = \iint_S dx_3 \dots dx_N \, |\Psi(x, x', x_3, x_4, \dots, x_N)|^2 = \langle \hat{\Psi}^\dagger(x) \hat{\Psi}^\dagger(x') \hat{\Psi}(x') \hat{\Psi}(x) \rangle, \tag{2.30}$$

where the integration is performed over the entire configuration space $\mathcal{S}$ and which can be interpreted as the conditional probability of finding a particle at position x' given that another particle is located at x. The corresponding operator takes the form

$$\hat{G}_2(x,x') = \hat{\Psi}^\dagger(x)\hat{\Psi}^\dagger(x')\hat{\Psi}(x')\hat{\Psi}(x) = \sum_{j,j',k,k'} \varphi^*_{j'}(x)\varphi^*_{k'}(x')\varphi_k(x')\varphi_j(x)\,\hat{b}^\dagger_{j'}\hat{b}^\dagger_{k'}\hat{b}_k\hat{b}_j. \tag{2.31}$$

The value of the correlation function is obtained by evaluating the expectation value of this operator in the given many-body eigenstate $|\Psi\rangle$

$$G_2(x,x') = \langle\Psi|\,\hat{G}_2(x,x')\,|\Psi\rangle\,. \tag{2.32}$$

Importantly, in systems with periodic boundary conditions, the correlation function depends only on the relative distance between the points x and x'. In such cases, it is customary to express it as a function of a single variable

$$G_2(x,x') = G_2(x-x',0) = G_2(x). \tag{2.33}$$

2.2 Density matrix renormalization group

The Density Matrix Renormalization Group (DMRG) method is one of the most powerful and widely used techniques for investigating the ground states of discrete one-dimensional quantum systems, particularly when interactions are limited to short ranges (i.e., between sites separated by at most a few lattice spacings). Originally introduced in [55, 56], the method has since been significantly developed, most notably through its formulation in terms of tensor network notation, which allows for a compact and efficient representation of quantum many-body states.

In this section, I briefly outline the core principles of the DMRG algorithm, specifically in the context of the problems to which it has been applied in this thesis: the calculation of the ground state of a systems of few bosons confined in one-dimensional lattices with open-boundary conditions described by Bose-Hubbard Hamiltonian

$$\hat{H} = J\sum_{j=0}^{M}\left(\hat{b}^\dagger_{j+1}\hat{b}_j + h.c.\right) + \frac{U}{2}\sum_{j=0}^{M}\hat{n}_j(\hat{n}_j - 1), \tag{2.34}$$

where operators $\hat{b}_j$, $\hat{b}^\dagger_j$ and $\hat{n}_j$ indicates annihilation, creation and occupation operators at j-th lattice node. However, given the vast amount of theoretical and

practical knowledge surrounding this method, for a more in-depth treatment the reader is encouraged to consult one of the many pedagogically excellent reviews, such as [57, 58, 59, 60, 61], as well as the documentation of the numerical libraries [62, 63, 64].

1 Tensor diagram notation

The working principle of the Density Matrix Renormalization Group can be explained in two distinct ways. Historically, the original formalism was rooted in fundamental quantum mechanical concepts such as density matrices, operator representations and partial trace. However, more recent approaches usually use the language of tensor networks, in which quantum states and operators are represented graphically as interconnected blocks. Since modern tutorials and numerical frameworks use almost exclusively the latter representation, I will also follow this path.

Moving forward, the success of the Tensor Diagram Notation (TDN) lies in its ability to represent objects such as vectors, matrices, and higher-order tensors as simple blocks annotated with appropriate indices, as illustrated in Fig. 2.4. Furthermore, by introducing the concept of tensor contraction, this notation allows for an intuitive graphical representation of fundamental algebraic operations, such as matrix multiplication or taking the matrix trace.

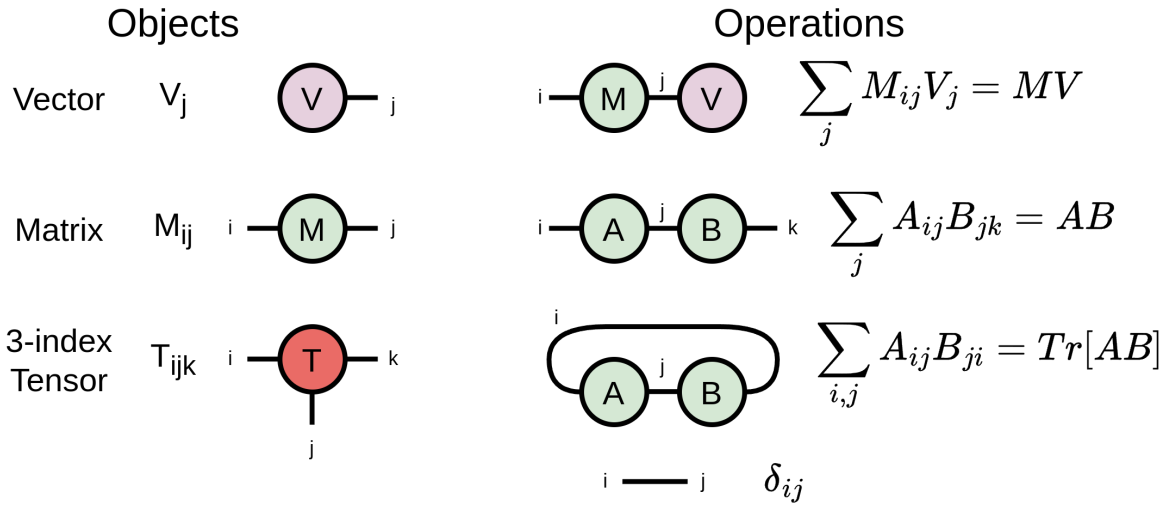

Figure 2.4: Basic objects (left column) and operations (right column) that appears in Tensor Diagram Notation.

2 Matrix product state and matrix product operator

To demonstrate how TDN can be used to represent quantum states and operators, let me begin with the most basic form of this approach. Formally, any quantum state describing a discrete system — e.g. a group of N atoms on a lattice with N_s sites — can be expressed in terms of a basis of Fock states as follows

$$|\Psi\rangle = \sum_{\sigma_1,\ldots,\sigma_{N_s}} \psi_{\sigma_1,\ldots,\sigma_{N_s}} |\sigma_1,\ldots,\sigma_{N_s}\rangle\,, \tag{2.35}$$

where σ_i denotes the local degree of freedom at site i (e.g. occupation number), and $\psi_{\sigma_1,\ldots,\sigma_{N_s}}$ is the amplitude associated with the configuration $\{\sigma_i\}$. This high-rank tensor $\psi_{\sigma_1,\ldots,\sigma_{N_s}}$ can be represented in the form of a *matrix product state* (MPS) as follows

$$|\Psi\rangle = \sum_{\sigma_1,\ldots,\sigma_{N_s}} U^{\sigma_1} U^{\sigma_2} \cdots U^{\sigma_{N_s}} |\sigma_1,\ldots,\sigma_{N_s}\rangle\,, \tag{2.36}$$

where each U^{σ_i} is interpreted as a matrix (or more precisely, a rank-2 or rank-3 tensor) corresponding to a fixed physical index σ_i. More concretely, the tensor U^{σ_i} has components $U^{\sigma_i}_{\alpha_{i-1},\alpha_i}$, where α_{i-1} and α_i are referred to as *virtual* or *bond* indices, and σ_i is the *physical* or *visible* index.

Graphically, this decomposition corresponds to expressing the full rank-N_s tensor $\psi_{\sigma_1,\ldots,\sigma_{N_s}}$ as a network of N_s interconnected rank-2 and rank-3 tensors (see Fig. 2.5). The horizontal links represent contractions over virtual indices (i.e. matrix multiplications), while the vertical legs correspond to the physical indices of the system. What needs to be highlighted, any quantum state can be written in the MPS form [59].

Singular value decomposition

To fully understand the idea behind the Matrix Product State formalism and to highlight its most important advantages, it is necessary to introduce a key mathematical operation — Singular Value Decomposition (SVD) — which plays a crucial role in the following sections. Specifically, the singular value decomposition of an $m \times n$ complex matrix $\mathbf{M}$ is a factorization of the form

$$M = USV^\dagger \tag{2.37}$$

where U and V are unitary matrices of dimensions $m \times m$ and $n \times n$, respectively, and S is a diagonal matrix of size $m \times n$ with real, non-negative entries on the diagonal.

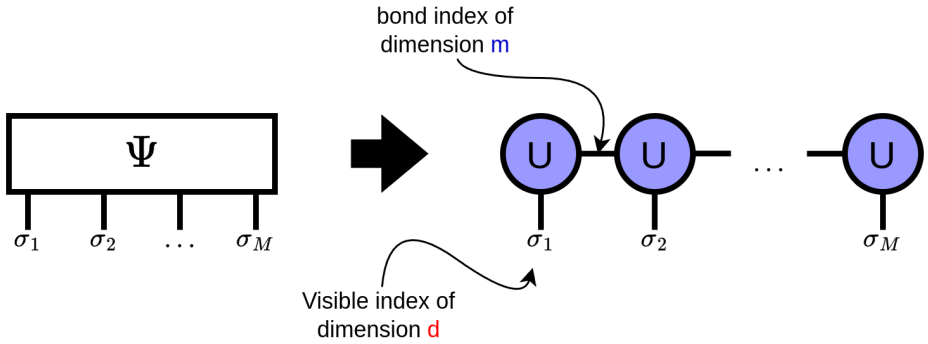

Figure 2.5: Tensor diagram representation of a quantum state in the Matrix Product State form. Vertical *legs* correspond to physical (visible) indices σ_j, which encode the local configuration of the quantum state, while horizontal bonds denote virtual (hidden) indices connecting adjacent tensors. These virtual indices allow the high-rank wavefunction tensor Ψ to be efficiently represented as a tensor train.

Importantly, SVD can be used for efficient information compression. By rewriting the matrix M as

$$M = \sum_{j=1}^{r} U_j S_{j,j} V_j^\dagger, \tag{2.38}$$

where U_j and $V_j^\dagger$ represent the $j-th$ column or row of matrices U and $V^\dagger$ respectively, it becomes clear that the contribution of each combination of vectors U_j and V_j to the structure of M is determined by the corresponding singular value $S_{j,j}$. This means that by retaining only the largest singular values (and the corresponding columns of U and V), one can efficiently approximate the original matrix using a smaller number of vectors. While this truncation does not always result in a significant reduction in size, it has been shown to work remarkably well for the one-dimensional systems of interest here — specifically, those with *gaped Hamiltonians* — yielding very effective compression.

To demonstrate how SVD can be used to construct MPS representations, let us walk through the process in more detail. Referring back to Eq. (2.35), consider decomposing the tensor $\psi_{\sigma_1,\ldots,\sigma_{N_s}}$

$$\psi_{\sigma_1,\ldots,\sigma_{N_s}} = \Psi_{\sigma_1,(\sigma_2,\ldots,\sigma_{N_s})} = \sum_{\alpha_1} U_{\sigma_1,\alpha_1} S_{\alpha_1,\alpha_1} V^\dagger_{\alpha_1,(\sigma_2,\ldots,\sigma_{N_s})} = \sum_{\alpha_1} U_{\sigma_1,\alpha_1} \psi^{(\alpha_1)}_{\sigma_2,\ldots,\sigma_{N_s}}, \tag{2.39}$$

where $\psi^{(\alpha_1)}_{\sigma_2,\ldots,\sigma_{N_s}}$ denotes the remaining part of the tensor after the first decomposition. Next, the same procedure can be recursively applied to the remaining tensor

$$\psi_{\sigma_2,\ldots,\sigma_{N_s}} = \Psi_{\sigma_2,(\sigma_3,\ldots,\sigma_{N_s})} = \sum_{\alpha_2} U_{\sigma_2,\alpha_2} S_{\alpha_2,\alpha_2} V^\dagger_{\alpha_2,(\sigma_3,\ldots,\sigma_{N_s})} = \sum_{\alpha_2} U_{\sigma_2,\alpha_2} \psi^{(\alpha_2)}_{\sigma_3,\ldots,\sigma_{N_s}}. \tag{2.40}$$

This procedure can be continued for each subsequent site in the chain until the full tensor is decomposed into the MPS form

$$\psi_{\sigma_1,\ldots,\sigma_{N_s}} = \sum_{\alpha_1,\ldots,\alpha_{N_s-1}} U_{\sigma_1,\alpha_1} U_{\alpha_1,\sigma_2,\alpha_2} \cdots U_{\alpha_{N_s-2},\sigma_{N_s-1},\alpha_{N_s-1}} U_{\alpha_{N_s-1},\sigma_{N_s}}. \tag{2.41}$$

It is important to note that in the general case — without applying truncated SVD or exploiting any symmetries of the system — the dimensions of the tensors U^σ will grow as $(1,d)$, (d,d^2), (d^2,d^3), ..., (d^2,d), $(d,1)$. This means that the number of parameters required to describe a quantum state grows exponentially with the number of lattice sites, which is suboptimal compared to storing the full wavefunction as a single tensor.

Examples of MPS

Since understanding of tensor-network notation is crucial for DMRG algorithm, below I present examples of few characteristic quantum many-body states appearing in the context of the Bose-Hubbard model, expressed in the matrix product state formalism. First, let us consider the Fock state corresponding to a single atom localized at the first site of a lattice with $N_s = 3$ nodes, namely $|\Psi\rangle = |100\rangle$. Since it is a product state, its MPS representation has bond dimension equal to 1, and all "tensors" reduce to scalars

$$U^{[\sigma_1=0]} = 0, \quad U^{[\sigma_1=1]} = 1; \quad U^{[\sigma_2=0]} = 1, \quad U^{[\sigma_2=1]} = 0; \quad U^{[\sigma_3=0]} = 1, \quad U^{[\sigma_3=1]} = 0. \tag{2.42}$$

More complicated version of a previous example is the so-called W state, where the single atom can occupy any lattice site

$$|W_3\rangle = \frac{1}{\sqrt{3}} \left(|100\rangle + |010\rangle + |001\rangle \right). \tag{2.43}$$

Its MPS representation is given by the following matrices

$$\begin{aligned}
&\text{Site 1 } (1\times 2 \text{ matrices}): \quad U^{[\sigma_1=0]} = \begin{bmatrix} 1 & 0 \end{bmatrix}, \quad U^{[\sigma_1=1]} = \begin{bmatrix} 0 & 1 \end{bmatrix}, \\
&\text{Site 2 } (2\times 2 \text{ matrices}): \quad U^{[\sigma_2=0]} = \begin{bmatrix} 0 & 1 \\ -\frac{1}{\sqrt{2}} & 0 \end{bmatrix}, \quad U^{[\sigma_2=1]} = \begin{bmatrix} -\frac{1}{\sqrt{2}} & 0 \\ 0 & 0 \end{bmatrix}, \\
&\text{Site 3 } (2\times 1 \text{ matrices}): \quad U^{[\sigma_3=0]} = \begin{bmatrix} -\frac{\sqrt{2}}{\sqrt{3}} \\ 0 \end{bmatrix}, \quad U^{[\sigma_3=1]} = \begin{bmatrix} 0 \\ \frac{1}{\sqrt{3}} \end{bmatrix}.
\end{aligned} \tag{2.44}$$

Importantly, the structure presented above generalizes naturally to a lattice with more sites. For example, the analogous state in lattice with $N_s = 4$ sites $|W_4\rangle$ is

described by

$$\begin{aligned}
&\text{Site 1 } (1\times 2 \text{ matrices}): \quad U^{[\sigma_1=0]} = \begin{bmatrix} 1 & 0 \end{bmatrix}, \quad U^{[\sigma_1=1]} = \begin{bmatrix} 0 & 1 \end{bmatrix}, \\
&\text{Site 2 } (2\times 4 \text{ matrices}): \quad U^{[\sigma_2=0]} = \begin{bmatrix} 0 & 1 & 0 & 0 \\ -\frac{1}{\sqrt{2}} & 0 & \frac{1}{\sqrt{2}} & 0 \end{bmatrix}, \quad U^{[\sigma_2=1]} = \begin{bmatrix} -\frac{1}{\sqrt{2}} & 0 & -\frac{1}{\sqrt{2}} & 0 \\ 0 & 0 & 0 & 1 \end{bmatrix}, \\
&\text{Site 3 } (4\times 2 \text{ matrices}): \quad U^{[\sigma_3=0]} = \begin{bmatrix} -\frac{\sqrt{2}}{\sqrt{3}} & 0 \\ 0 & -1 \\ 0 & 0 \\ 0 & 0 \end{bmatrix}, \quad U^{[\sigma_3=1]} = \begin{bmatrix} 0 & 0 \\ \frac{1}{\sqrt{3}} & 0 \\ 0 & 0 \\ 0 & 0 \end{bmatrix}, \\
&\text{Site 4 } (2\times 1 \text{ matrices}): \quad U^{[\sigma_4=0]} = \begin{bmatrix} \frac{\sqrt{3}}{2} \\ 0 \end{bmatrix}, \quad U^{[\sigma_4=1]} = \begin{bmatrix} 0 \\ -\frac{1}{2} \end{bmatrix}.
\end{aligned} \tag{2.45}$$

Left- and right-orthogonality

When discussing matrix product states, one shall discuss so called left- and right orthogonality of tensors. Basically, as long as we operate only on the whole matrix product states it is not important, but problem arises when we want to “divide“ tensor train into two parts. Lets take a look at the state

$$|\Psi\rangle = \sum_{\sigma} A^{\sigma_1} A^{\sigma_2} ... A^{\sigma_{N_s-1}} A^{\sigma_{N_s}} |\sigma_1 \sigma_2 ... \sigma_{N_s-1} \sigma_{N_s}\rangle \tag{2.46}$$

This state can be written also in the form “split“ into two parts - A and B

$$|\Psi\rangle = \sum_{\alpha_l} |\alpha_l\rangle^A |\alpha_l\rangle^B \tag{2.47}$$

where

$$|\alpha_l\rangle^A = \sum_{\sigma_1,...,\sigma_l} (A^{\sigma_1} ... A^{\sigma_l})_{1,\alpha_l} |\sigma_1 ... \sigma_l\rangle \tag{2.48}$$

$$|\alpha_l\rangle^B = \sum_{\sigma_{l+1},...,\sigma_{N_s}} (A^{\sigma_{l+1}} ... A^{\sigma_{N_s}})_{\alpha_l,1} |\sigma_{l+1} ... \sigma_{N_s}\rangle \tag{2.49}$$

At this point there appear the unexpected issue: it would be beneficial to heave both of these states orthonormal, i.e. ${}^A\langle\alpha_{l'}|\alpha_l\rangle^A = {}^B\langle\alpha_{l'}|\alpha_l\rangle^B = \delta_{l,l'}$. From the definition, these values are given by

$${}^A\langle\alpha_{l'}|\alpha_l\rangle^A = \sum_{\sigma_1,...,\sigma_l} (A^{\sigma_l\dagger} ... A^{\sigma_1\dagger} A^{\sigma_1} ... A^{\sigma_l})_{\alpha'_l,\alpha_l} \tag{2.50}$$

$${}^B\langle\alpha_{l'}|\alpha_l\rangle^B = \sum_{\sigma_{l+1},...,\sigma_{N_s}} (A^{\sigma_l} ... A^{\sigma_1} A^{\sigma_1\dagger} ... A^{\sigma_l\dagger})_{\alpha'_l,\alpha_l} \tag{2.51}$$

For this reason, when a bipartition of the state is expected, it is beneficial to represent the tensors belonging to subsystem A in a left-orthogonal and belonging to subsystem B in a right-orthogonal form. Specifically, for sites $j \leq l$, all tensors satisfy the condition $\sum_{\sigma_j} A^{\sigma_j \dagger} A^{\sigma_j} = I$, while for sites $j > l$, the tensors satisfy $\sum_{\sigma_j} A^{\sigma_j} A^{\sigma_j \dagger} = I$. This ensures the orthogonality of the MPS around the cut. Graphically, this orthogonality can be represented as the contraction of appropriate tensor trains yielding the identity matrix (see Fig. 2.6).

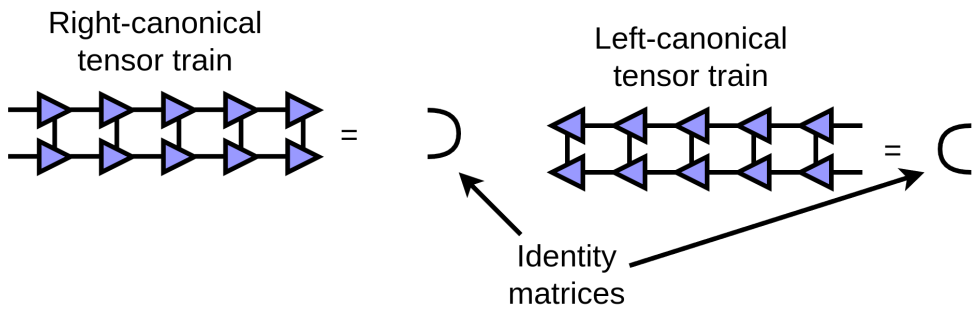

Figure 2.6: Graphical presentation of the right- and left-orthogonal tensors.

Matrix product operator

Analogously to quantum states, quantum mechanical operators can also be represented in the tensor train form.

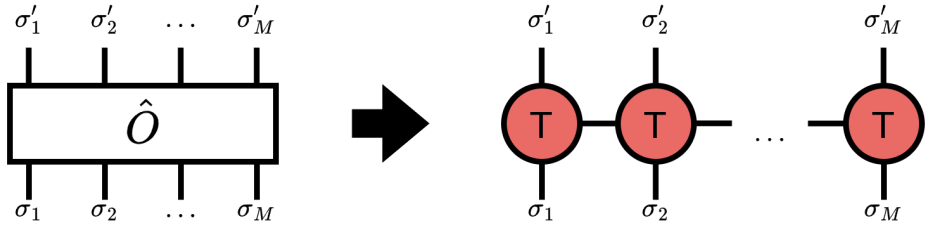

Figure 2.7: Tensor diagram representation of a quantum operator expressed in the Matrix Product Operator form.

Formally, any operator $\hat{O}$ acting on an M-site Hilbert space can be written as

$$\hat{O} = \sum_{\sigma'_1,\ldots,\sigma'_M} \sum_{\sigma_1,\ldots,\sigma_M} O^{\sigma'_1,\ldots,\sigma'_M}_{\sigma_1,\ldots,\sigma_M} \left|\sigma'_1,\ldots,\sigma'_M\right\rangle \left\langle\sigma_1,\ldots,\sigma_M\right|, \tag{2.52}$$

where the coefficient tensor $O^{\sigma'_1,\ldots,\sigma'_M}_{\sigma_1,\ldots,\sigma_M}$ can be decomposed into a product of local tensors as

$$O^{\sigma'_1,\ldots,\sigma'_M}_{\sigma_1,\ldots,\sigma_M} = \sum_{\{\alpha\}} T^{\sigma'_1,\alpha_1}_{\sigma_1} T^{\sigma'_2,\alpha_2}_{\alpha_1,\sigma_2} \cdots T^{\sigma'_M,}_{\alpha_{M-1},\sigma_M}, \tag{2.53}$$

where $\{\alpha\}$ denotes the set of auxiliary bond indices. This tensor network structure is depicted graphically in Fig. 2.7.

3 Finite system DMRG

Having introduced the basic concepts, we are ready to outline the finite-size DMRG algorithm. At this point, it is worth mentioning the distinction between the classical and modern approaches to DMRG. Historically, the process began with the so-called infinite DMRG; however, in contemporary implementations, this step is usually omitted [58, 59].

Step 1: optimization and adaptation of first bond

As a first step, one need to prepare an initial version of the quantum state. In the code implementation used in the later parts of this project, the DMRG algorithm begins from the left side of the lattice. Therefore, in the initial state, all tensors corresponding to visible indices greater than one should be right-orthogonal (see Fig. 2.8(a)).

The MPS is then divided into two parts: the left part containing sites 1 and 2, and the remaining part of the chain. This operation results in two new tensor trains with an additional unconnected index α_2, which was previously the bond index between the original tensors. Next, the tensors corresponding to sites 1 and 2 are contracted over their shared bond, forming a single object denoted as B_{12}.

Then, the effective "Hamiltonian" that will be used to optimize the tensor B_{12} needs to be constructed. To do so, the part of the MPS corresponding to sites 3, 4, 5,... is used to average out the Hamiltonian contributions from the higher-index sites. As a result, the effective Hamiltonian depends only on six indices, as illustrated in Fig. 2.8(b).

The effective Hamiltonian can then be used to optimize the tensor B_{12}, i.e., to minimize the total energy of the system by selecting appropriate values for this tensor. This optimization can be efficiently performed using iterative eigensolvers

such as the Lanczos or Davidson algorithm [65]. The result of this procedure is a new tensor, denoted as B'_{12}, which minimizes the total energy (see Fig. 2.8(c)).

Once the optimized tensor B'_{12} is obtained, it is necessary to restore the matrix product state form. This is typically achieved using the truncated singular value decomposition. In this procedure, the tensor is decomposed into three components: a left-orthogonal matrix U (with orthogonality guaranteed by the properties of the SVD), a diagonal matrix S containing the singular values, and another right-orthogonal matrix V.

At this stage, the most important aspect of the DMRG algorithm takes place: data compression by truncations in SVD. Specifically, by retaining only the most significant singular values in the matrix S, one can effectively reduce the bond dimension (this procedure is discussed in more detail in Sec. 2). Finally, to maintain concise notation, the truncated matrix S is then absorbed into the right tensor, and the whole MPS is reconstructed into a single tensor train.

Optimization and adaptation of remaining bonds

After restoring the MPS form, the algorithm proceeds by repeating a similar procedure for the pair of MPS tensors associated with the second bond index (tensors with visible indices i_2 and i_3). First, these two tensors are merged to define a new bond tensor B_{23}. Next, B_{23} is optimized to minimize the total energy of the effective Hamiltonian resulting in new tensor B'_{23}.

Once the improved bond tensor is obtained, it is factorized using a truncated singular value decomposition to compress the state, restore the MPS form and adapt the bond dimension. Finally, to prepare for the optimization of the next bond, the singular value matrix S_{23} is merged with right hand side matrix and the structure of a MPS is restored.

The procedure outlined in the previous steps is then systematically repeated for subsequent bonds, following the scheme illustrated in Fig. 2.9. Upon reaching the final bond of the system, the direction of the sweep is reversed, and the optimization is continued in the opposite direction. This sweeping procedure is iterated until the assumed convergence criteria — typically defined in terms of changes in energy and entanglement entropy — are satisfactorily met.

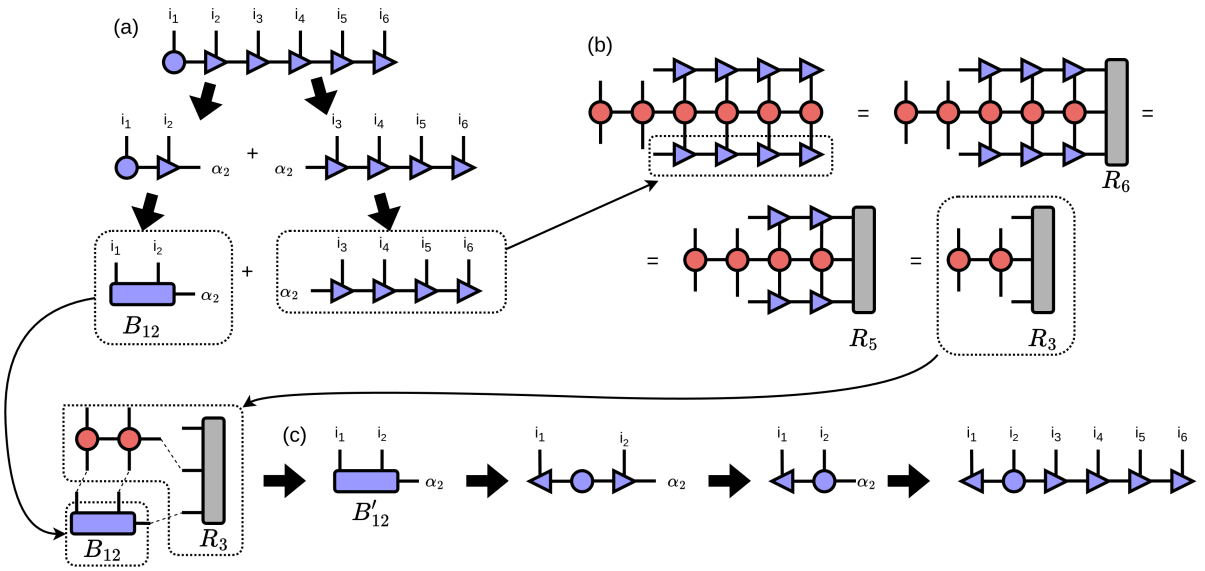

Figure 2.8: Schematic representation of the stages involved in optimizing the first bond using the DMRG algorithm. (a) The initial Matrix Product State is partitioned into two segments. The tensors corresponding to sites 1 and 2 are then contracted over their shared bond to form a rank-3 tensor B_{12}. (b) The remaining part of the MPS is used to construct the effective Hamiltonian acting on B_{12}. This is done by averaging the operators acting on sites beyond index 2 in the state of sites $i = 2, 3, \ldots$. (c) The effective Hamiltonian is then used to optimize B_{12}, minimizing the total energy of the system. The optimized tensor is denoted as B'_{12}. Next, a truncated singular value decomposition is performed on B'_{12}, retaining only the number of singular values specified by the maximum bond dimension and truncation error threshold. The diagonal matrix of singular values is then absorbed into the tensor associated with the right-hand side of the bond. Finally, the updated tensors for sites 1 and 2 are reconnected with the remaining sites, restoring the structure of the full MPS.

4 Practical aspects of DMRG applications

Following the theoretical introduction, the aim of this section is to discuss practical aspects of the numerical calculations. In the systems of interest (Bose-Hubbard model), key physical parameters include the number of lattice sites N_s, the number of particles N, and the coefficients U and J appearing in the Hamiltonian. To this list, one can also add the maximum assumed number of atoms that can simultaneously occupy a single lattice site (`maxOcc`).

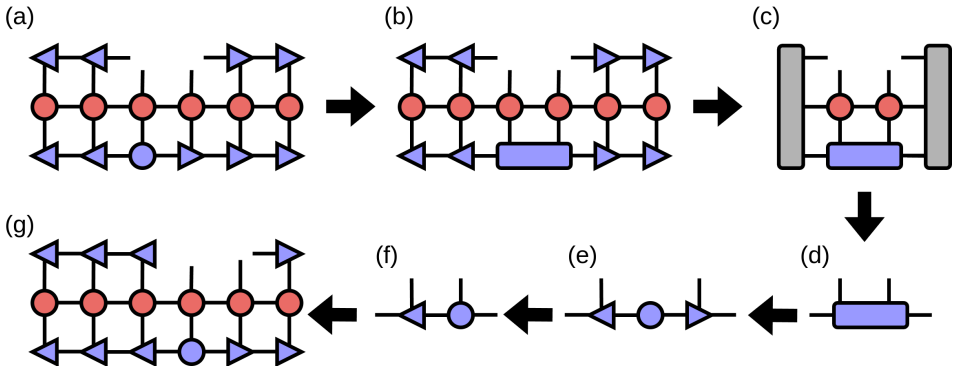

Figure 2.9: A diagrammatic illustration of the DMRG procedure is presented using tensor network notation. Initially, (a) the matrix product state is brought into a form that all tensors to the left of the bond being optimized are left-orthogonal, while those to the right are right-orthogonal. Next, (b) the two tensors adjacent to the targeted bond are contracted, and (c) the remaining tensors on the left and right are also contracted. Subsequently, (d) the energy is minimized by optimizing the bond tensor. This is followed by (e) a truncated singular value decomposition, where the state is compressed by retaining only the most significant singular values. Finally, (f,g) the optimized tensor is decomposed and the state is restored to the matrix product state form. After that, the procedure is repeated for the adjacent bond.

The other important numerical parameters are the initial state used to start the entire procedure, the number of sweeps, and parameters controlling the accuracy: `Largest bond dimension in the system` and the `Largest accepted truncation error`. Since two latter conditions typically act in opposition, they are often used separately: one must choose whether to prioritize higher accuracy by adapting the size of the computational basis to the problem (by fixing maximal allowed truncation error), or to focus on computational resources, potentially accepting reduced precision (by defining maximal bond dimension). It is worth noting that in large-scale simulations, these constraints are usually varied throughout the process. Initially, a lower precision is often acceptable in order to quickly perform a rough optimization of the in initial state, while later the basis size is increased to achieve the desired level of accuracy.

In Fig. 2.10, I present an example illustrating a simple ground state computation process, initiated with all particles occupying the first N sites. As can be seen there, the figure consists of three panels: (a), where `maxDim` = 5; (b), where `maxDim` = 10; and (c), where `maxDim` = ∞, what implies that in the latter case the truncation error equals zero. As can be observed, in all cases the occupation distribution reached

a form close to the final state after only three sweeps. Importantly, visually all three final states appear almost identical, which suggests that the system is well approximated even when using a maximum bond dimension as small as $\texttt{maxDim} = 5$.

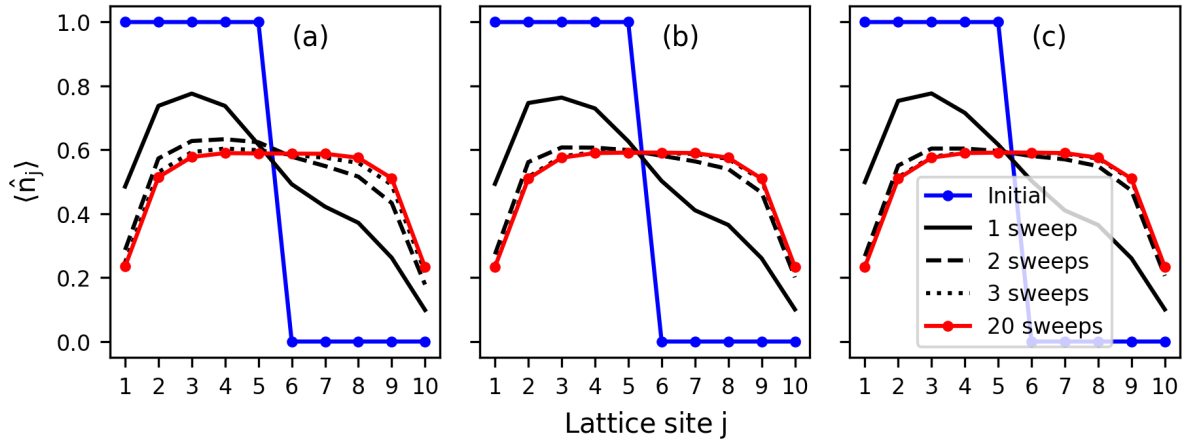

Figure 2.10: The process of obtaining the ground state of the Bose–Hubbard model using the Density Matrix Renormalization Group algorithm is illustrated here. Three distinct cases with different maximum bond dimensions are presented: (a) $\mathrm{maxDim} = 5$, (b) $\mathrm{maxDim} = 10$, and (c) $\mathrm{maxDim} = \infty$. As shown, the average number of atoms occupying the lattice sites $\langle \hat{n}_i \rangle$ changes gradually and converges to the final distribution after only three sweeps. Notably, even for $\mathrm{maxDim} = 5$, the differences compared to the case without any numerical restrictions are barely noticeable. In this example, we consider a system of $N = 5$ bosons in a lattice with $N_s = 10$ sites, where the Hamiltonian parameters are set to $J = U = 1$. Additionally, the maximum on-site occupation is set to $\mathrm{maxOcc} = \mathrm{N}$, and the truncation error was minimized as much as possible for the chosen bond dimension.

This observation finds confirmation in Fig. 2.11, which shows how the energy, entanglement entropy, and truncation error converge over successive sweeps. What can be seen is that both the energy and the entanglement entropy measured at the central bond stabilize after approximately three sweeps. Importantly, in the problem under consideration, the differences between the system with a maximum bond dimension of $\texttt{maxDim} = 10$ and the one without any bond dimension restriction are almost negligible in terms of energy and entropy. This is further supported by the plot of the largest truncation error: for $\texttt{maxDim} = 10$, it remains below 10^{-5} throughout all sweeps.

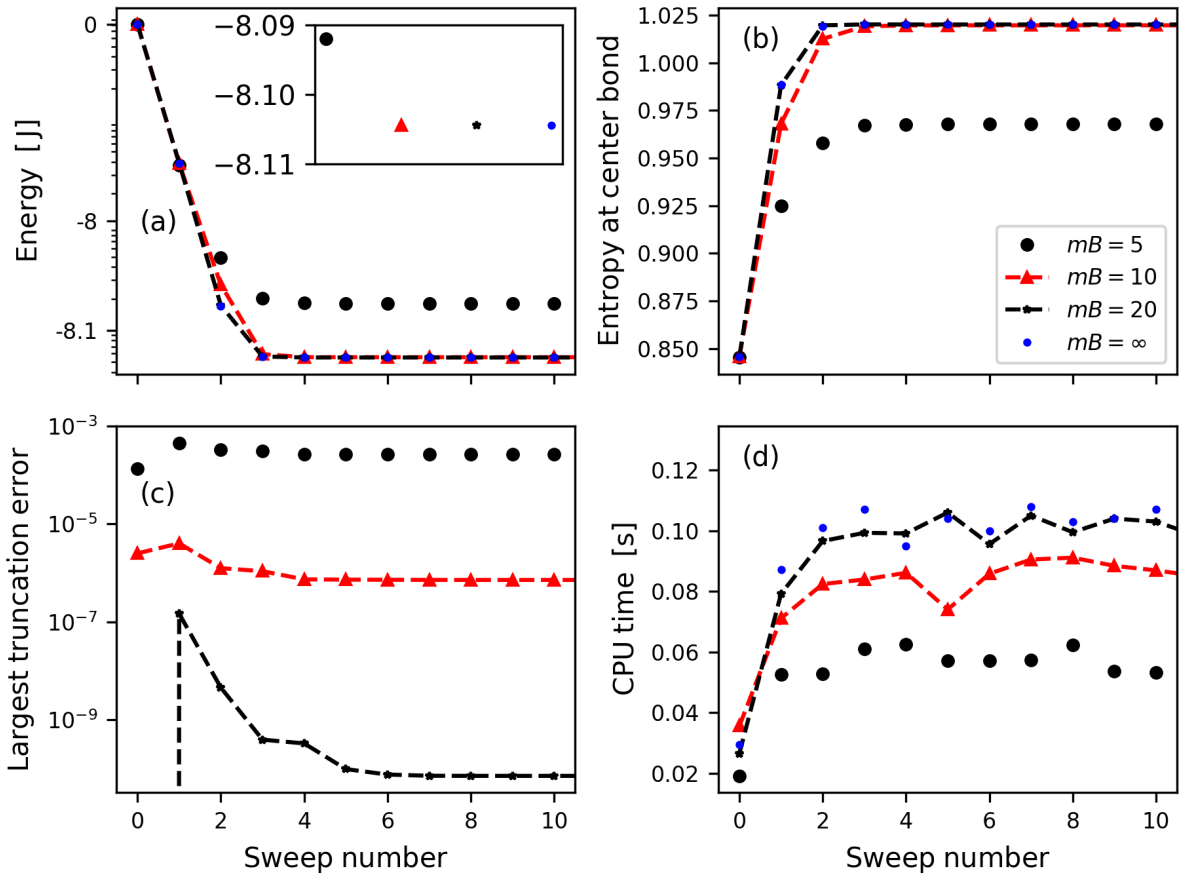

Figure 2.11: Key system parameters changes during the ground state search via the DMRG algorithm are presented here. As shown in panel (a), the energy converges relatively quickly for all maximum bond dimensions. In the inset, the final energies obatined by DMRG are presented. Notably, the final energy for $\mathrm{maxDim} = 10$ is already very close to that of the unrestricted case. A similar trend is observed in panel (b), where the entanglement entropy at the central bond is shown. Panel (c) displays the largest truncation error occurring during each sweep, clearly illustrating the differences in numerical precision depending on the chosen maxDim. Finally, panel (d) shows the average CPU time required for a single sweep, highlighting the trade-off between computational cost and precision. The von Neumann entropy was evaluated here with the natural logarithm base.

The figure 2.11 also includes an additional panel illustrating the time required to perform a full single sweep. While the exact values may vary depending on the hardware used, the overall trends and relative proportions are expected to hold. As can be observed, after an initial increase, where the base and entropy grows, the

durations of individual sweeps stabilize once the system converges. The time per sweep depends on the maximum bond dimension, although this dependence is not linear.

To finalize the description of the basic parameters that can be varied in practical implementations of DMRG, I present Fig. 2.12, which shows the dependence of the energy, maximum bond dimension, and average sweep time on the maximum occupation number. As the specific numerical data was presented here, it must be highlighted that to perform calculations I used iTensor library [66].

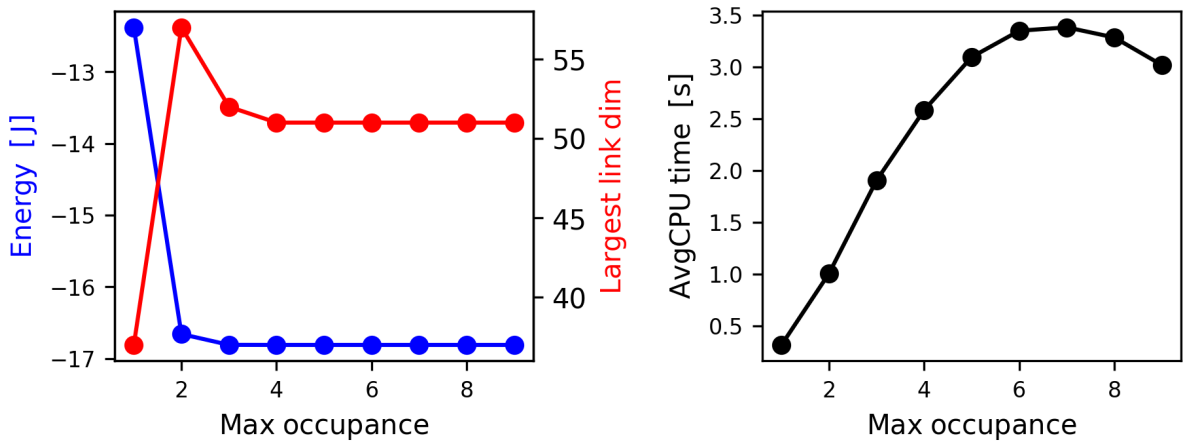

Figure 2.12: Panel (a) shows the ground state energy and the largest bond dimension obtained via the DMRG algorithm for the Bose–Hubbard Hamiltonian, computed with varying values of the maximum on-site occupation number (maxOcc). Panel (b) presents the corresponding average CPU time per single sweep for each case. As observed, the energy converges rapidly, indicating that for this system, the required maxOcc can be significantly smaller than the total number of particles. The results correspond to a system of $N = 10$ bosons in a lattice with $N_s = 20$ sites and open boundary conditions. The Hamiltonian parameters are set to $U = J = 1$.

DMRG: aspects left untouched

As can be seen, the DMRG procedure has been discussed here only to a very limited extent: the exploitation of conserved quantum numbers, system symmetries, methods for optimal parameter tuning, or parallelization techniques, have been omitted. These topics were left out as — as mentioned earlier — there exists a vast amount of literature, from educational resources to highly specialized studies

[58, 59, 67, 68, 66], in which experts in the field have comprehensively addressed these issues.

2.3 Summary

This chapter was devoted to the description of the two main numerical methods employed in the present thesis. However, depending on the specific requirements of individual tasks, despite the plane wave expansion and DMRG, several additional techniques were applied. These include, in particular, *imaginary time evolution*, used mostly for finding the ground states, and the *time-dependent variational principle* (TDVP) [69, 70, 71], which was utilized to simulate the time evolution of states obtained via the DMRG algorithm. As these methods played a secondary role in this study, they are not discussed here in detail.

Chapter 3

Super-Tonks-Girardeau effect in models with single type of interaction potential

The primary aim of this chapter is to establish a theoretical foundation for studies over the super-Tonks–Girardeau (sTG) effect. The core material presented here was developed during a research project documented in Ref. [72], conducted under the guidance of Prof. Bruno Juliá-Díaz, Prof. Grigory E. Astrakharchik, and Prof. Krzysztof Pawłowski, whose insights and supervision significantly shaped the final structure and scope of the work. While this project provides the central results discussed below, the chapter is also supplemented by an extensive conceptual introduction to the topic. This additional content was included with the intention of enhancing the educational value of the thesis and making the chapter accessible as a potential entry point for researchers interested in the field of super-Tonks–Girardeau effect.

3.1 Single atom and Dirac delta potential

The essence of sTG effect can be captured by a very simple model: a single particle of mass m in an infinitely long one-dimensional box. At the center of this box, there is a very narrow potential, which can be approximated by a Dirac delta function. The Hamiltonian of this model takes the form

$$\hat{H} = -\frac{\hbar^2}{2m}\frac{\partial^2}{\partial x^2} + g\delta(x), \tag{3.1}$$

where x is the spatial position of the particle and g is the potential coefficient.

To determine the eigenstates of this system, it is convenient to divide space into two regions: one on the left and the other on the right of the delta potential

$$\Psi(x) = \begin{cases} \Psi_L(x), \text{ if x} < 0 \\ \Psi_R(x), \text{ if x} > 0. \end{cases} \tag{3.2}$$

As one can see, the domains of both, the left- and right hand side functions exclude point with nonzero potential. It means that both satisfy the Schrödinger equation for a free particle in a one dimensional space $-\frac{\hbar^2}{2m}\frac{\partial^2}{\partial x^2}\Psi_{L(R)}(x) = E\Psi_{L(R)}(x)$, what implies that

$$\Psi(x) = \begin{cases} \Psi_L(x) = A_L e^{\kappa x} + B_L e^{-\kappa x}, & \text{if x} < 0 \\ \Psi_R(x) = A_R e^{\kappa x} + B_R e^{-\kappa x}, & \text{if x} > 0 \end{cases} \tag{3.3}$$

where the exponent is directly related to the energy via the expression $\kappa = \sqrt{-2E}$.

The relations between the parameters in the wavefunctions can be determined by analyzing the connections between the left- and right-side solutions. First and foremost, the wavefunction must be continuous across the entire space $\Psi_L(0) = \Psi_R(0) = \Psi(0)$. Additionally, one might expect the wavefunction to be smooth (expect its first derivative to also be continuous). However, in the model investigated here the Hamiltonian includes a Dirac delta potential and, consequently, there occurs discontinuity in the first derivative of the wavefunctions. The relationship between the derivatives on the left and right side of potential can still be established by integrating the Schrödinger equation around the point $x = 0$

$$-\frac{\hbar^2}{2m}\int_{-\epsilon}^{\epsilon}\frac{\partial^2}{\partial x^2}\Psi(x)\ \mathrm{dx} + g\int_{-\epsilon}^{\epsilon}\delta(x)\Psi(x)\ \mathrm{dx} = E\int_{-\epsilon}^{\epsilon}\Psi(x)\ \mathrm{dx}\,. \tag{3.4}$$

For $\epsilon \to 0$ the right hand side in Eq. (3.4) vanishes, resulting in the equation that define relations between derivatives of the functions and potential coefficient

$$\frac{\hbar^2}{2m}\frac{\partial}{\partial x}\Psi_R(x)|_{x=0} - \frac{\hbar^2}{2m}\frac{\partial}{\partial x}\Psi_L(x)|_{x=0} = g\Psi(0). \tag{3.5}$$

Applying these two boundary conditions to equation 3.3 yields

$$\begin{cases} A_L + B_L = A_R + B_R \\ \kappa(A_R - A_L + B_L - B_R) = \frac{2mg}{\hbar^2}(A_R + B_R) \end{cases} \tag{3.6}$$

what, after a simple transformation reduces to

$$\begin{cases} B_L = \frac{\hbar^2\kappa}{mg}(A_R - A_L) - A_L \\ B_R = \frac{\hbar^2\kappa}{mg}(A_R - A_L) - A_R. \end{cases} \tag{3.7}$$

At this point, I will introduce an additional constraint on the wavefunction. Since the latter part of this text will focus on states that are symmetric with respect to the delta potential, I will also here restrict the scope of study to states satisfying the condition $\Psi(x) = \Psi(-x)$, introducing an additional relation between the coefficients in the wavefunction: $A_R = B_L$ and $A_L = B_R$. By combining these with the two previously stated conditions, one obtain

$$B_R = \frac{\kappa - \tilde{g}}{\kappa + \tilde{g}} A_R \tag{3.8}$$

and consequently

$$\Psi(x) = \mathcal{N}(e^{-\kappa|x|} + \frac{\kappa - \tilde{g}}{\kappa + \tilde{g}} e^{\kappa|x|}), \tag{3.9}$$

where $\tilde{g} = \frac{mg}{\hbar^2}$ and $\mathcal{N}$ is the normalization factor.

Under these conditions, the wavefunction is found to take one of two qualitatively distinct forms. If the energy of the system is negative $E < 0$, the exponent κ is a real and positive number. As a consequence, by investigating Eq. (3.9) one can find, that the term proportional to $e^{\kappa|x|}$ will diverges at $x \to \pm\infty$. To avoid this non-physical situation it is necessary to ensure that coefficient scaling this exponential part equals zero. The only one option to ensure that is to choose $\kappa = \tilde{g}$.

It has two implications: (i) states of this form can be obtained only for negative values of the potential coefficient, i.e. for $\tilde{g} < 0$; (ii) for each negative potential coefficient, there exists a unique state characterized by the parameter κ, with the corresponding energy equal to

$$E = -\frac{\kappa^2}{2} = -\frac{m^2 g^2}{2\hbar^4} \tag{3.10}$$

and the wavefunction given by

$$\Psi(x) = \sqrt{\kappa} e^{-\kappa|x|}. \tag{3.11}$$

In this case, the particle is in a so-called *bound state*, where the probability of finding particle at some point x decays exponentially with distance from the potential.

The second family of solutions — characterized by positive energies $E \geq 0$ — corresponds to so-called *unbound* states, also referred to as *scattering* or *free* ones.

In these states, exponent κ is imaginary. Consequently, the expression multiplying one of the exponents in Eq. (3.9) is the complex number with unitary amplitude and can be written as

$$\frac{ik - \tilde{g}}{ik + \tilde{g}} = e^{2i\theta(k,g)}. \tag{3.12}$$

where $ik = \kappa, k \in \mathrm{Re}$. By substituting this formulation into equation Eq. (3.9), one can obtain a simplified version of the unbound wavefunction

$$\Psi(x) = \mathcal{N} e^{i\theta(k,\tilde{g})} \cos(k|x| + \theta(k, \tilde{g})). \tag{3.13}$$

As one can see in Eq. (3.13), the probability density of finding an atom, given by $|\Psi(x)|^2 = |\mathcal{N}|^2 \cos^2(k|x| + \theta(k, g))$, does not vanish with increasing distance from the potential. Consequently, this type of wavefunction cannot be normalized. However, despite this inconvenience, the model serves as a good approximation for certain real-life processes and can be effectively used to illustrate the phenomena that constitute the main subject of this work.

1 Duality of eigenstates in the infinite potential limits

Let me now discuss in more details the ground state of the aforementioned system. Broadly speaking, four distinct cases can be distinguish (see Fig. 3.1):

(i) for negative values of potential coefficient the ground state is a bound state, with the wavefunction given by $\Psi_0(x, \tilde{g} < 0) = \sqrt{\kappa} e^{-\kappa|x|}$ (for brevity, the parameter $\tilde{g}$ was included as an argument of the function, and an index was added to Ψ_0 to indicate that it represents the ground state);

(ii) for zero potential ($\tilde{g} = 0$) in the lowest-energy state, the particle is uniformly distributed across all space. The wavefunction is constant $\Psi_0(x, \tilde{g} = 0) \propto 1$ with corresponding energy $E = 0$;

(iii) for positive and finite values of $\tilde{g} > 0$, the ground-state wavefunction is symmetric and still asymptotically approaches a constant value as $x \to \pm\infty$, but it develops a *cusp* at $x = 0$. The depth of this cusp $D(\tilde{g})$ defined as

$$D(\tilde{g}) = \frac{\max|\Psi(\mathrm{x}, \tilde{\mathrm{g}})| - |\Psi(\mathrm{x} = 0, \tilde{\mathrm{g}})|}{\max|\Psi(\mathrm{x}, \tilde{\mathrm{g}})|} = 1 - \cos(\theta(k, \tilde{g})) \tag{3.14}$$

increases with $\tilde{g}$; that is, for $\tilde{g}' > \tilde{g}$, wavefunction follows the relation $D(\tilde{g}') > D(\tilde{g})$;

(iv) for $\tilde{g} \to \infty$ the extreme case occurs. In that limit, depth of the cusp tends to unity $D(\tilde{g} \to \infty) \to 1$ and in the wavefunction at $x = 0$ there appears the so-called *node*, meaning the wavefunction equals zero at the point $\Psi_0(0, \tilde{g} \to \infty) = 0$.

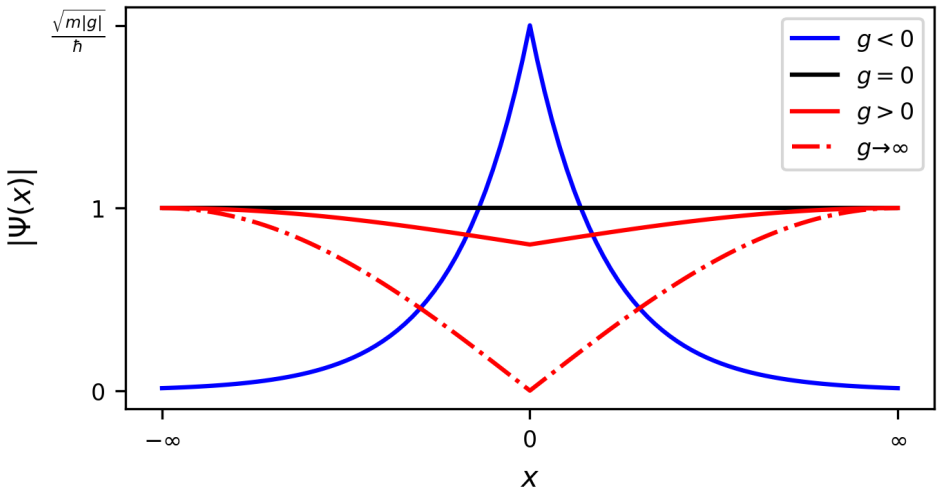

Figure 3.1: The ground states of the Hamiltonian (3.1) corresponding to four distinct values of the potential coefficient $\tilde{g} = (mg)/\hbar^2$. States corresponding to $\tilde{g} \geq 0$ were normalized in a way to set their maximum value to unity.

The latter case will play an important role in the following analysis. Therefore, even though this feature of the system aligns with our physical intuition, I will examine it in a more precise way. Fundamentally, the emergence of a node is a consequence of the boundary conditions. As shown in equation Eq. (3.5), the derivatives of the wavefunction are proportional to the expression $\tilde{g}\Psi(x = 0)$. This implies that any nonzero value of $\Psi(x = 0)$ would result in the derivatives of the wavefunction on both sides becoming infinite. For wavefunctions expressed as plane waves, this would correspond to infinite energy, which is clearly unphysical. Therefore, the only way to avoid this divergence is to require that for infinitely repulsive potentials $\Psi(x = 0, \tilde{g} \to \infty) = 0$.

What is particularly important is that the ground-state eigenfunction of the system in the limit $\tilde{g} \to \infty$ is also the first symmetric excited eigenstate $\Psi_{1S}(x)$ of the Hamiltonian with $\tilde{g} \to -\infty$! Mathematically, this can be simply proven using the same approach as for the $\tilde{g} \to \infty$ case. However, to gain a deeper understanding of this crucial phenomenon, it can be helpful to examine the physical properties of some excited states in more details.

To do so, let us repeat the analysis performed for the ground state, this time applied to the first symmetric excited eigenstate $\Psi_{1S}(x, \tilde{g})$ (see Fig. 3.1):

(i) for a system without a potential barrier ($\tilde{g} = 0$), this wavefunction is smooth (as potential coefficient is zero, there is no discontinuance in the first derivative) and maintains two nodes;

(ii) when the potential coefficient is positive ($\tilde{g} > 0$), a cusp appears at $x = 0$, similar to that observed in the ground state;

(iii) As $\tilde{g} \to \infty$, this excited-state wavefunction also tends to zero at the origin $\Psi_{1S}(0, \tilde{g} \to \infty) \to 0$ (in a system there are three nodes).

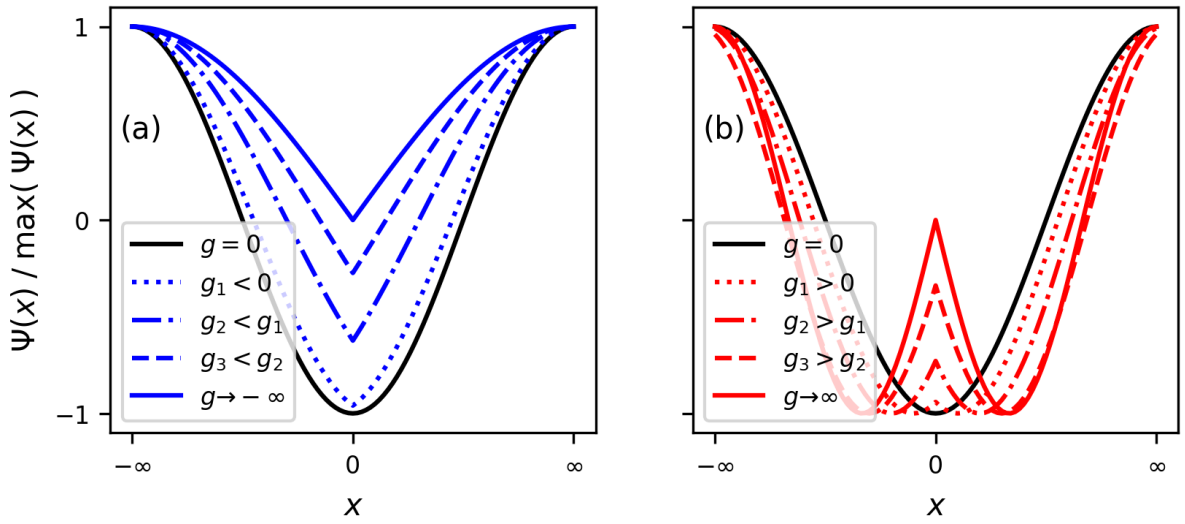

Figure 3.2: First symmetric excited eigenstates of Hamiltonian Eq. (3.1) for (a) negative (attractive) and (b) positive (repulsive) potential coefficients. Wavefunctions were normalized in a way to set their maximum value to unity.

The behavior becomes even more interesting for negative values of $\tilde{g}$. As mentioned earlier, for any $\tilde{g} < 0$, there can be only one bound eigenstate — namely, the ground state. This implies that all excited states for $\tilde{g} < 0$ must be scattering states. When applying the boundary conditions (as discussed in the previous section), one finds that the excited eigenfunctions exhibit a *peak* at $x = 0$.

Moreover, this peak becomes sharper for increasingly negative values of potential coefficient. This result in the probability density near of the point $x = 0$ being... lower for more attractive potentials $|\Psi_{1S}(x = 0, \tilde{g}')|^2 < |\Psi_{1S}(x = 0, \tilde{g})|^2$ for $\tilde{g}' < \tilde{g}$. Consequently, in the limit $\tilde{g} \to -\infty$, the excited-state wavefunction converges to the same form as the ground state wavefunction $\Psi_{1S}(x, \tilde{g} \to -\infty) \to \Psi_0(x, \tilde{g} \to \infty)$.

This counterintuitive feature of a system invites us to perform a simple thought experiment. Imagine an experimental setup consisting of an extremely long one-dimensional tube containing a single atom. Inside the tube, there is a narrow potential barrier, whose amplitude $\tilde{g}$ can be precisely controlled (see Fig. 3.3(a)).

Now, suppose we prepare the system with a very strong barrier, i.e. $\tilde{g} \to \infty$, and the atom occupying the ground state. Starting from this point, if we gradually decrease the potential parameter down to $\tilde{g} \to -\infty$, we would observe that the atom becomes increasingly localized around the potential, as it is expected for a bound ground state.

However, if we instead abruptly switch the potential from $\tilde{g} \to \infty$ to $\tilde{g} \to -\infty$ (this process is called as a *quench*), the system does not have time to adjust. In this case, the atom "jumps" into the excited state $\Psi_{1S}(x, \tilde{g} \to -\infty)$, which, remarkably, is structurally identical to the original state. After that process, the system remains stable in this excited state for a long time (see Fig. 3.3(b)). What is particularly important is that this feature generalizes to higher excited states as well. Using the same reasoning, one can find that $\Psi_{1S}(x, \tilde{g} \to \infty) = \Psi_{2S}(x, \tilde{g} \to -\infty)$, $\Psi_{2S}(x, \tilde{g} \to \infty) = \Psi_{3S}(x, \tilde{g} \to -\infty)$ and generally $\Psi_{NS}(x, \tilde{g} \to \infty) = \Psi_{(N+1)S}(x, \tilde{g} \to -\infty)$.

2 Periodic boundary conditions

Phenomena discussed in the previous sections are not limited to systems with an infinite spatial domain. Qualitatively, the same features also arise in a system where an atom is confined within a finite box of length L ($x \in (-L/2, L/2]$) with periodic boundary conditions. This setup offers several advantages over the infinite-space case. For instance, unbound states in system with finite length remain normalizable. Consequently, from this point onward I will focus primarily on this kind of systems.

With regard to the wavefunctions, the periodicity of the system imposes two additional boundary conditions that constrain their behavior at the edges of the box. Specifically, the wavefunction must be continuous and smooth at $x = \pm L/2$

$$\begin{cases} \Psi(-\frac{1}{2}L) = \Psi(\frac{1}{2}L) \\ \frac{\partial}{\partial x}\Psi(x)|_{x=-L/2} = \frac{\partial}{\partial x}\Psi(x)|_{x=L/2}. \end{cases} \tag{3.15}$$

Applying these constraints to the general formula for the wavefunction given by equation Eq. (3.9), one can find that the first condition is always satisfied, as we have restricted ourselves to symmetric functions. The second condition, however, has a

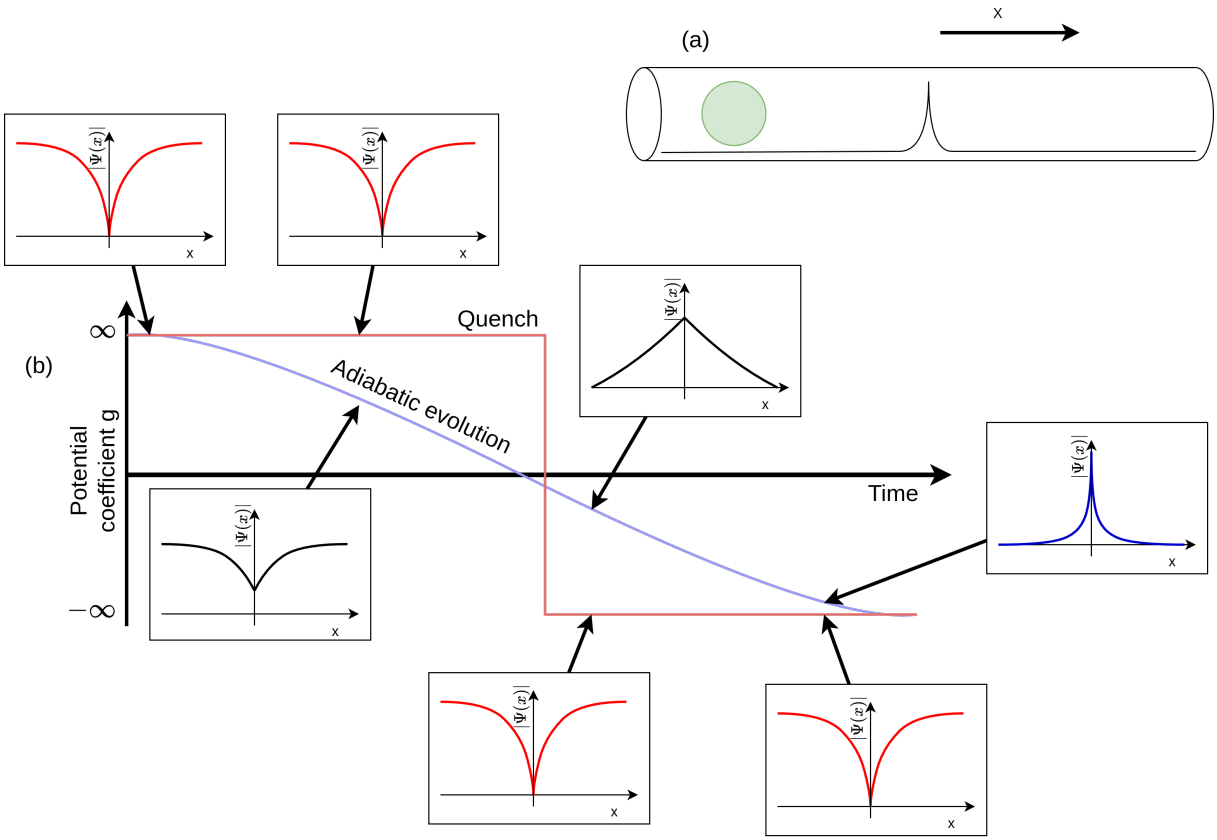

Figure 3.3: Schematic representation of (a) the experimental setup discussed in Sec. 1; (b) the changes occurring in the gas during two types of processes discussed there. In the case of an adiabatic transition, the wavefunction follows the ground state, gradually evolving toward the bound state. In contrast, an abrupt quench of the interaction strength preserves the structure of the initial state, effectively mapping it directly onto the first excited state of the post-quench Hamiltonian.

significant impact on the wavefunction. The derivative of the wavefunction is of the form of

$$\frac{\partial}{\partial x}\Psi(x) = -\frac{x}{|x|}\kappa\left(e^{-\kappa|x|} - \frac{\hbar^2\kappa - gm}{\hbar^2\kappa + gm}e^{\kappa|x|}\right) \tag{3.16}$$

and, after substituting it into Eq. (3.15), determines the allowed values for the parameter κ (where $\kappa = \sqrt{-2E}$)

$$\frac{\kappa - \tilde{g}}{\kappa + \tilde{g}} = e^{-\kappa L} \tag{3.17}$$

This expression can be used to simplify the notation used in Eq. (3.9). After substituting the equality from Eq. (3.17) into the general formula given by Eq. (3.9)

one obtain

$$\Psi(x) = \mathcal{N}(e^{-\kappa|x|} + e^{\kappa(|x|-L)}) \tag{3.18}$$

The remaining properties of the wavefunctions do not change significantly. The states can still be classified into two qualitatively distinct families: bound states with negative energies and unbound states with positive energies. However, in contrast to the case of an infinite line, there are some important differences.

Let us begin with the self-bound states. As before, the exponent κ is a positive real number. This leads to the exponential term $e^{\kappa|x|}$ in the wavefunction given by equation Eq. (3.18), which grows rapidly with the distance from $x = 0$. In the infinite system, this divergence had to be avoided by eliminating the growing exponential through an appropriate choice of κ. In the finite system, however, this is no longer an issue. The space is limited, so both growing and decaying exponentials can be included, resulting in a wavefunction of the form

$$\Psi(x) = \mathcal{N}e^{-\kappa L/2}(e^{-(\kappa(|x|-L/2))} + e^{\kappa(|x|-L/2)}) = \mathcal{N}' \cosh\Big(\kappa\Big(|x| - \frac{L}{2}\Big)\Big) \tag{3.19}$$

As the coefficient κ is real, equation Eq. (3.17) has only one solution what determines that there is only one bound state for every negative value of potential coefficient g.

In the second family of states, corresponding to non-negative energies, exponent is imaginary $\kappa = ik$. The wavefunctions are given as

$$\Psi(x) = \mathcal{N}\cos(k(|x| - L/2)). \tag{3.20}$$

This time, the wavefunction can be normalized. As the relation occurs

$$\int_0^L \cos^2(k(|x| - L/2))dx = \frac{L}{2}\left(1 + \frac{\sin(kL)}{kL}\right) \tag{3.21}$$

the normalization factor is given by

$$\mathcal{N} = \left(\frac{L}{2} + \frac{\sin(kL)}{2k}\right)^{-1/2}. \tag{3.22}$$

It must be highlighted that additional boundary conditions clearly define the allowed values of the coefficient k Eq. (3.23)

$$Lk = -\tilde{g}\cot(Lk/2). \tag{3.23}$$

As can be seen from equation Eq. (3.23), for any value of the potential coefficient $\tilde{g}$, there are infinitely many roots. The structure of the equation — one can think

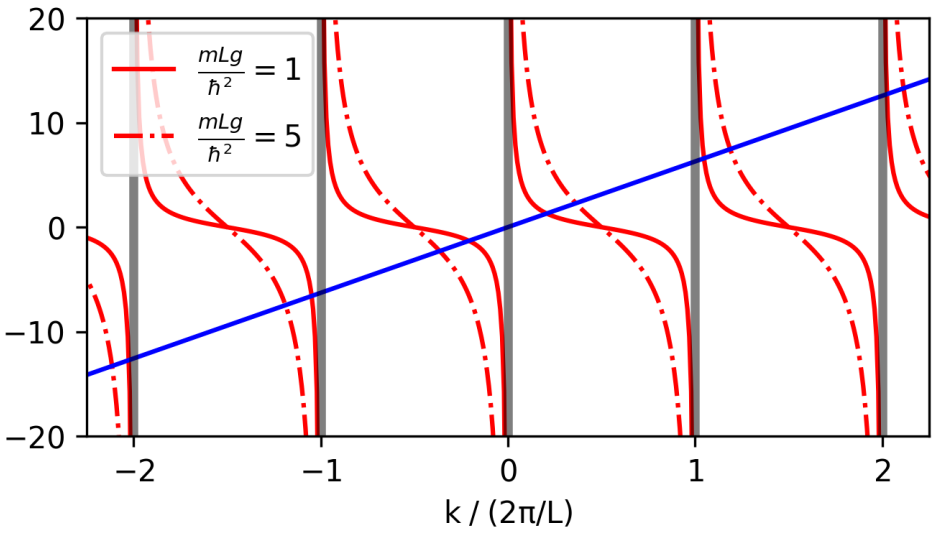

Figure 3.4: Graphical representation of Eq. (3.23), defining allowed values of momenta in the system with a single Dirac delta potential. The blue line depicts the left-hand side of the equation, while the red curves represent the right-hand side. As shown, the intersection points determining the allowed momentum values shift with changing g. Due to the periodicity of the right-hand side, there are infinitely many solutions: in each interval $k_n \in \left[\frac{2\pi}{L}n, \frac{2\pi}{L}(n+1)\right)$, exactly one solution exists. The spectrum of allowed momenta is symmetric under momentum inversion.

of it as searching for the crossing points between a straight line and the cotangent function (see Fig. 3.4) — allows to conclude that there will be exactly one root in each interval defined as $k_n \in [\frac{2\pi}{L}n, \frac{2\pi}{L}(n+1))$. Consequently, for every value of the potential parameter $\tilde{g}$, there are infinitely many eigen-energies; however, their distribution is no longer continuous. The differences between adjacent energy levels are finite. For instance, in the case of a system with $\tilde{g} = 0$, the allowed energies are given by $E_0 = 0, E_1 = \frac{4\pi^2\hbar^2}{mL^2}, E_2 = \frac{16\pi^2\hbar^2}{mL^2}, \ldots$, with the general form $E_n = \frac{4\pi^2\hbar^2 n^2}{mL^2}$ where n is an integer number.

3 Pumping procedure

The exact relations between potential coefficient and energy introduced in previous section allow to examine the aforementioned phenomenon from a different perspective. Let us consider the energy spectrum shown in Fig. 3.5. As seen there, for each value of $\tilde{g}$, there are many possible energy levels. However, the spectrum is organized into distinct branches.

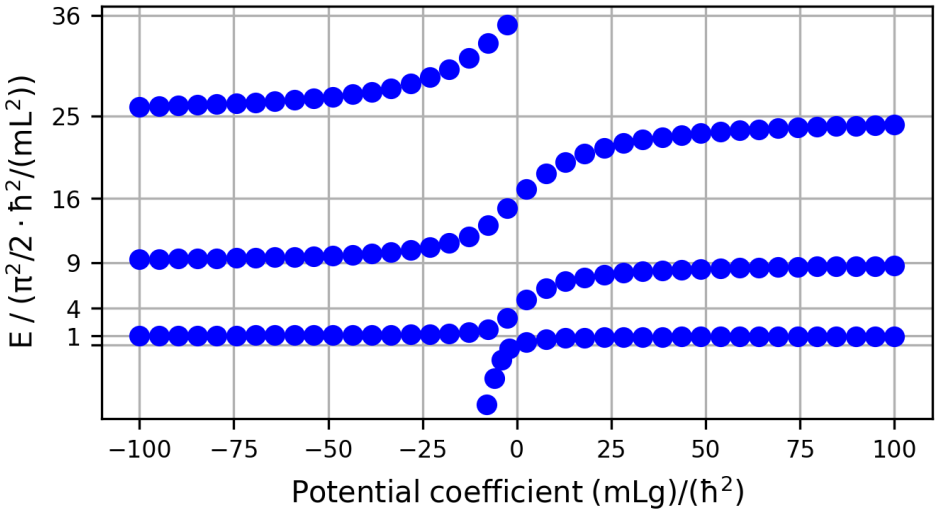

Figure 3.5: Energy spectrum of a single atom within a 1D periodic box. The distinct energy branches are visible.

The existence of these branches plays the important role in our investigations. Within each branch, for any two values $\tilde{g} \neq \tilde{g}'$, as $\tilde{g}' \to \tilde{g}$, the corresponding energies and eigenstates converge ($E(\tilde{g}') \to E(\tilde{g})$ and $\Psi(\tilde{g}', x) \to \Psi(\tilde{g}, x)$) (intuitively, this can be understood in the sense that the branches remain "continuous" for interaction strengths ranging from $g = -\infty$ to $g = \infty$). This implies that it is possible to adiabatically evolve between any two eigenstates belonging to the same energy branch by gradual change the potential coefficient.

For instance, the ground state corresponding to the system without any potential $\Psi_0(x, \tilde{g} = 0)$ is connected through a continuous branch to the ground state of the system with an infinitely repulsive barrier $\Psi_0(x, \tilde{g} \to \infty)$. It means that by gradually increasing potential strength from $\tilde{g} = 0$ to $\tilde{g} \to \infty$, one can adiabatically transform the former state into the latter one. Similarly, the first excited eigenstate of the system at $\tilde{g} \to -\infty$ is connected to the first excited state at $\tilde{g} = 0$. Therefore, a smooth transformation of $\tilde{g}$ enables an adiabatic transition between these two states ($\Psi_{1S}(x, \tilde{g} \to -\infty)$ and $\Psi_{1S}(x, \tilde{g} = 0)$) as well.

Moreover, by inspecting the structure of the eigenfunctions and allowed momenta in the limits $\tilde{g} \to \pm\infty$ it becomes evident that the ground state of the system at $\tilde{g} \to \infty$ corresponds to the first excited eigenstate of the system at $\tilde{g} \to -\infty$. Likewise, the first excited state at $\tilde{g} \to \infty$ corresponds to the second excited eigenstate at

$\tilde{g} \to -\infty$, and so forth

$$\begin{cases} \Psi_0(x, g \to \infty) = \Psi_1(x, g \to -\infty) \\ \Psi_1(x, g \to \infty) = \Psi_2(x, g \to -\infty) \\ \dots \\ \Psi_n(x, g \to \infty) = \Psi_{n+1}(x, g \to -\infty). \end{cases} \tag{3.24}$$

This observation implies that, by combining adiabatic evolution with sudden quenches of the interaction parameter, it is possible to transfer between any two eigenstates from any branches (for example, from $\psi_0(\tilde{g} = 0)$ to $\psi_1(\tilde{g} = 0)$). This non-typical procedure – combining adiabatic and quench dynamics resulting in an overall increase in the system's energy will be refereed to as the *pumping* procedure. The schematic representation of that process is presented in Fig. 3.6.

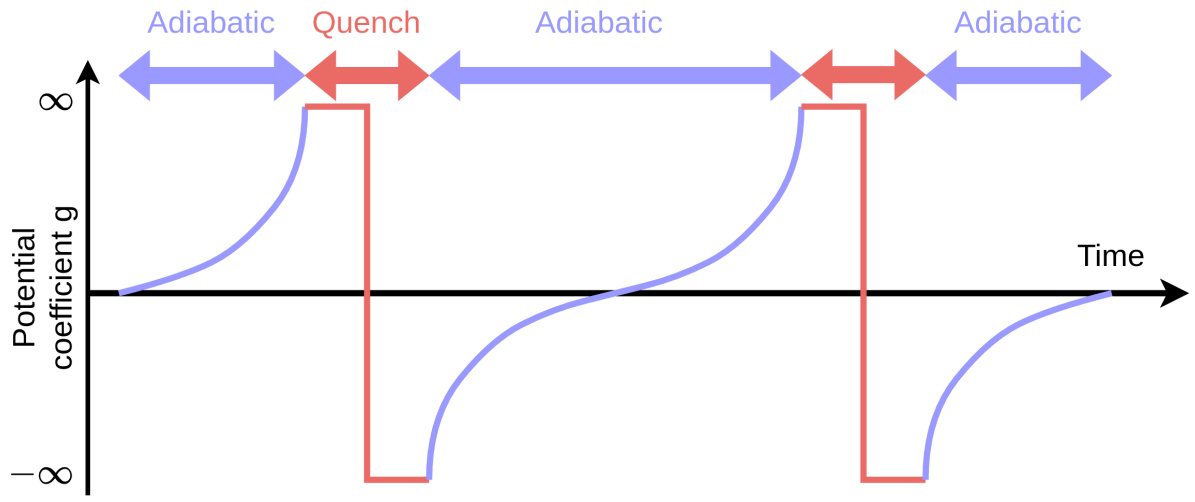

Figure 3.6: Schematic presentation of the *pumping* procedure.

4 Apparent hyper-repulsiveness of post-quench states

In this section, I would like to introduce in more detail one of the widely discussed phenomena related to the states that appear during the pumping process. Namely, the states arising immediately after a quench from $\tilde{g} \to \infty$ to $\tilde{g} \to -\infty$ exhibit behavior typical for state where the potential appears "more repulsive" than it was for $\tilde{g} \to \infty$.

To illustrate what the “repulsiveness“ means, let me first examine the ground state of the system. Its energy grows as the potential coefficient increases (for $\tilde{g}' > \tilde{g} \rightarrow E(\tilde{g}') > E(\tilde{g})$), while the probability of finding particle near (in the distance no larger than some small length $0 < d \ll L$) the location of the delta potential $P(d, \tilde{g})$ decreases (see left side of Fig. 3.7)

$$P(d, \tilde{g}) = \int_{-d}^{d} |\Psi(x, \tilde{g})|^2 dx = |\mathcal{N}|^2 \frac{\sin(kL) - \sin(kL + 2dk) + 2dk}{2k}. \tag{3.25}$$

This behavior aligns with naive expectations: stronger repulsion leads to higher energy and particle avoidance of the space near the potential. However, this intuition appears to break down when considering excited states for finite but strongly negative values of $\tilde{g}$. Specifically, we find that despite quenching into a regime with an attractive potential, the energy continues to increase, and, at the same time, the probability of finding the atom near the delta potential continues to decrease (see the right hand side of Fig. 3.7).

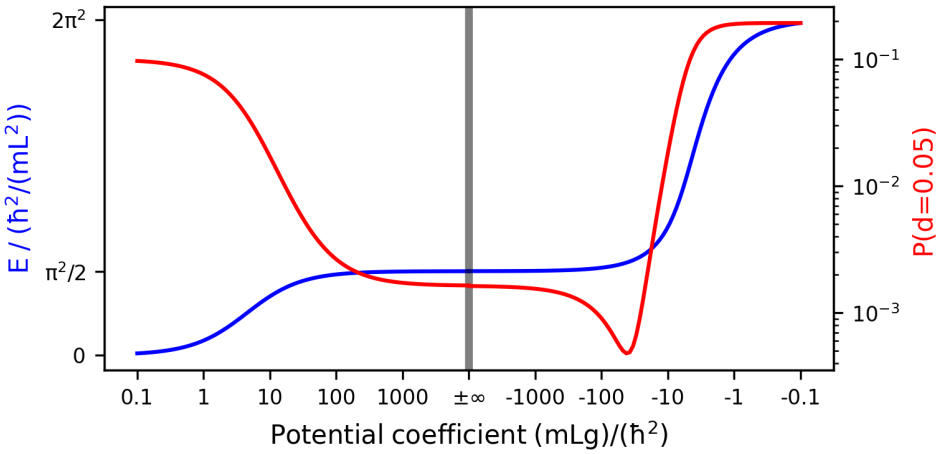

Figure 3.7: The energy (blue line) and the probability of finding an atom in the vicinity of the delta potential (red line, Eq. (3.25)), are plotted over the course of the first cycle of pumping. In the initial phase of the process, for positive $\tilde{g}$, an increase in the interaction strength is accompanied by a rising energy and a decreasing probability of finding the atom near the potential $P(d)$ (here I present probability of finding particle in the range $|x| \leq (d = 0.05L)$; for definition see Eq. (3.25)). Surprisingly, the quench does not disrupt this trend. After the quench — when a strong but attractive potential is applied — the growing potential results in a continued increase in energy and a further decrease in the probability of finding the atom near the potential.

This phenomenon in closely related to the subject of several studies in the past [73, 25, 36, 26]. Researchers found there that for excited states with strong but finite repulsive potentials the system behaves similarly to the ground state of a system with a potential in the form of an infinite rectangular barrier (see Fig. 3.8)

$$V_{RB}(x) = \begin{cases} \infty, \ |x| < d \\ 0 \ \text{ elsewhere.} \end{cases} \tag{3.26}$$

In the case of periodic systems this model can be considered as the single particle in a infinite rectangular quantum well of width $L - 2d$, where the eigenstates are of the form of

$$\Psi_{RB}(x) = \begin{cases} \sqrt{\frac{2}{L-2d}} \cos\left(\frac{\pi}{L-2d}\left(\frac{L}{2} - |x|\right)\right), \ \text{if } |\mathrm{x}| > \mathrm{d} \\ 0 \ \text{ elsewhere} \end{cases} \tag{3.27}$$

and the energy $E_{RB} = \frac{\pi^2\hbar^2}{2mL^2}$.

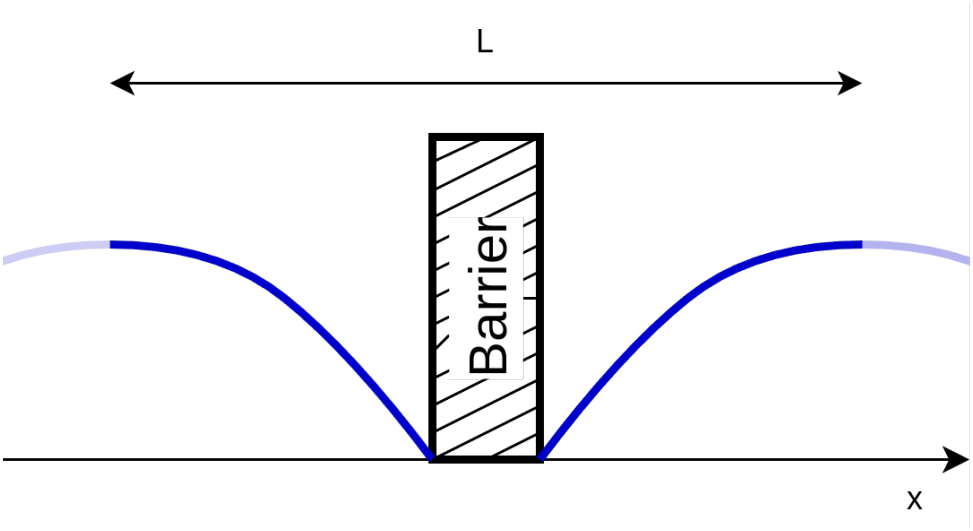

Figure 3.8: Infinite rectangular barrier and the corresponding ground state (blue line) in the 1D system with PBC of the length L. The groundstate is given by Eq. (3.27).

To understand the rudiment of the similarities between these two models it is beneficial to analyze the structure of the wavefunction of a model with delta potential in three cases: (i) the ground state for strong but finite $\tilde{g}$, (ii) the case of infinitely strong repulsion, and (iii) the first excited state obtained through topological pumping immediately after a quench.

From a mathematical standpoint, there are qualitative differences between these states and the infinite rectangular barrier. However, quantitatively, the differences

with the state after quench are not significant. For states belonging to the first excited branch, the wavefunction develops two nodes near $x = 0$. As long as $\tilde{g}L < -10$, the probability of finding the atom between these nodes is extremely small (see Fig. 3.7). This behavior is reminiscent of the infinite rectangular barrier, where the probability of finding the particle inside the barrier is zero and the wavefunction vanishes (has two nodes) at the barrier edges.

This observed similarity can be more rigorously confirmed by computing the fidelity (i.e. the squared overlap) between the state of interest and the ground state of the rectangular barrier, with the barrier width chosen to match the distance between the nodes

$$F = \left| \int_0^L \Psi^*_{RB}(x)\Psi(x)\ \mathrm{dx} \right|^2 \tag{3.28}$$

As shown in Fig. 3.9, for large and negative potential coefficient, the fidelity is high, indicating that the two states are indeed closely related. However, for intermediate values of $\tilde{g}$, where the probability of finding the atom between the nodes increases, this correspondence breaks down. An analogous behavior can also be observed for higher excited states, where similar node structures and effective barrier-like behavior emerge under strong repulsive interactions.

3.2 Few-body systems

The general statements made in the previous section can be extended to more complex systems, in which, instead of a single particle in an external potential, we consider a few-body system of bosons interacting via contact two-body interactions. In this section, I argue that the phenomena discussed earlier can also be observed in such models.

1 Two particles

To begin with, let me focus on a system of two indistinguishable bosons of mass m, confined in a one-dimensional trap of length L with periodic boundary conditions. The particles interact via a contact (delta-function) potential, meaning the interaction potential is nonzero only when the two point-like particles occupy the same position in space. The Hamiltonian describing this system is given by

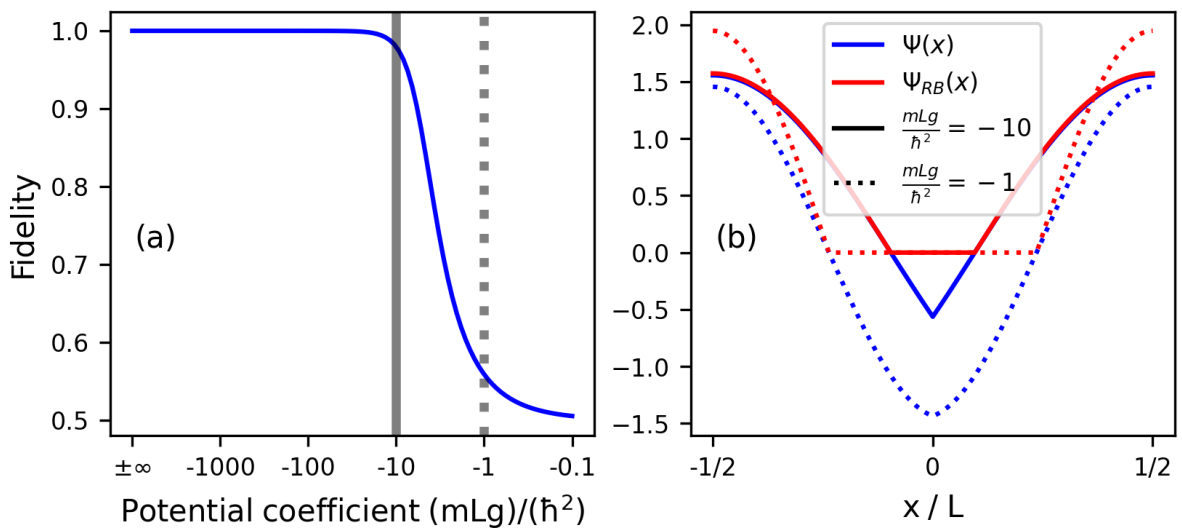

Figure 3.9: A comparison between the first excited state emerging during the pumping process and the ground state of a system with an infinite rectangular barrier, where the width of the barrier is equal to the distance between the nodes of the wavefunction $\Psi(x)$. Panel (a) presents the squared overlap between these two states, illustrating their degree of similarity. In panel (b), the wavefunctions corresponding to two different values of the potential strength are shown, demonstrating how these functions converge as the attraction becomes stronger. It can be observed that for $\tilde{g} = -10L$ (solid lines), the fidelity approaches unity and the corresponding wavefunctions are nearly indistinguishable. In contrast, for $\tilde{g} = -L$, where the fidelity is significantly lower, notable differences between the wavefunctions become apparent.

Eq. (3.29)

$$\hat{H} = -\frac{\hbar^2}{2m}\frac{\partial^2}{\partial x_1^2} - \frac{\hbar^2}{2m}\frac{\partial^2}{\partial x_2^2} + g\delta(x_1 - x_2), \tag{3.29}$$

where g, referred to as the *coupling constant*, characterizes the interaction strength. It is worth noting that since our study is related to the field of ultra-cold gases, the parameter g is closely associated to the scattering length. Additionally, from this point on, to simplify the notation, I define the space in which atoms can be such that $x_1, x_2 \in [0, L)$.

The eigenstates of the Hamiltonian (3.29) are generally functions of two spatial coordinates, namely $\hat{H}\Psi(x_1, x_2) = E\Psi(x_1, x_2)$. We investigate the system of two bosons, so consequently the wavefunction must be symmetric according to the

exchange of the particles $\Psi(x_1, x_2) = \Psi(x_2, x_1)$ and, due to periodic boundary conditions, must fulfill the condition that $\Psi(x_1 + L, x_2) = \Psi(x_1, x_2 + L) = \Psi(x_1, x_2)$.

Center of mass separation

Fortunately, to find the exact form of wavefunction it is not nessesary to solve the full two-dimensional differential equation. By introducing new coordinates: the center-of-mass position $X = \frac{x_1+x_2}{2}$ and the relative distance between particles $x = x_2 - x_1$, and substituting them into Eq. (3.29), the Hamiltonian separates into two independent parts, each acting on a different Hilbert space

$$\hat{H} = \hat{H}_X + \hat{H}_x, \tag{3.30}$$

where

$$\hat{H}_X = -\frac{\hbar^2}{4m}\frac{\partial^2}{\partial X^2}, \text{ and } \hat{\mathrm{H}}_\mathrm{x} = -\frac{\hbar^2}{\mathrm{m}}\frac{\partial^2}{\partial \mathrm{x}^2} + \mathrm{g}\delta(\mathrm{x}) \tag{3.31}$$

operate on the center-of-mass and relative coordinates, respectively. This allows us to write the full eigenfunction in a product form

$$\Psi(x_1, x_2) = \Phi\Big(\frac{x_1 + x_2}{2}\Big)\varphi(x_2 - x_2) = \Phi(X)\varphi(x), \tag{3.32}$$

where $\hat{H}_X\Phi(X) = E_X\Phi(X)$, $\hat{H}_x\varphi(x) = E_x\varphi(x)$ and the total energy equals $E = E_X + E_x$. In this model, the center-of-mass wavefunctions are a plane waves of the form

$$\Phi_n(X) = \frac{1}{\sqrt{L}}e^{i\frac{2\pi n}{L}X} \tag{3.33}$$

with corresponding energies given by $E_{X,n} = \frac{4\pi^2\hbar^2n^2}{mL^2}$, where n is the integer number enumerating the state. Since we are primarily interested in ultracold systems, we typically focus on cases where the center of mass occupies the lowest orbital (i.e. $n = 0$), yielding zero center-of-mass energy.

Relative wavefunction

The relative wavefunction $\varphi(x)$ is more involved. Fortunately, the Hamiltonian governing it is identical in form to the one discussed above (see Sec. 3.1), where a single atom in a box of the length L with a delta potential was considered. The only noteworthy difference here is that although the length of the box is the same L, the relative position between atoms can take values in the range $x \in (-L, L]$. Negative values correspond to situations where $x_2 < x_1$, while positive values represent the opposite case.

Based on previously established results, one can find that this system also supports two families of eigenstates: one corresponding to negative energies E_x and the other to positive energies. However, the interpretation of these states differs slightly in the two-particle context.

For negative energies, the wavefunction $\varphi(x)$ decays exponentially (or more precisely, takes the form of a hyperbolic cosine, which still implies localization) with respect to the relative coordinate x. This decay, however, does not indicate localization of the individual atoms themselves. Although the particles remain close to each other, the center-of-mass wavefunction is completely delocalized. As a result, the system behaves as a *self-bound* pair that can exist anywhere within the available space. The one-dimensional gas density, defined as the average number of atoms per unit length is therefore uniform $\rho(x) = \frac{N}{L}$, and the probability of finding a particle is equal throughout the system.

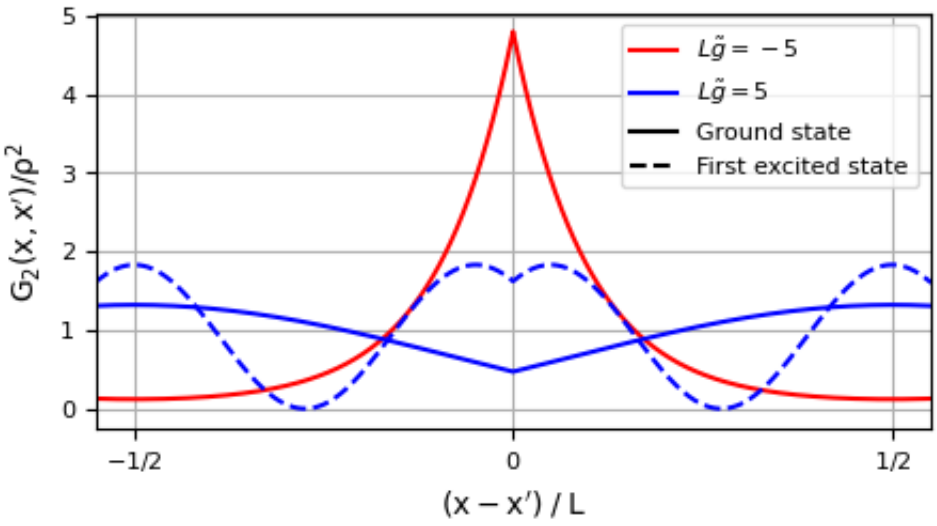

Figure 3.10: Second-order correlation functions for three distinct eigenstates of a system consisting of $N = 2$ atoms interacting via contact interactions in a periodic box. As shown, the correlation functions differentiate between self-bound states (red curve) and non-self-bound (scattering) states (blue curves). Notably, the excited eigenstates exhibit nodes in their wavefunctions, which manifest as zeros in the second-order correlation functions. According to the definition of the second-order correlation function, this indicates that in the excited states, the probability of simultaneously finding one atom at position x and the other at a separation corresponding to a node is exactly zero. Here, $\rho = N/L$ and $\tilde{g} = (gm)/\hbar^2$

For unbound (positive-energy) states, the situation is qualitatively similar: although the gas density remains uniform, the internal structure of the system is nontrivial.

Distinction between self-bound and scattering states becomes apparent when examining the second-order correlation function, which can be interpreted as a conditional probability of finding one particle at position x, given that the other is at x' (see Fig. 3.10). In the case of two atomic system this function is defined as a squared relative wavefunction

$$G_2(x_1, x_2) = |\Psi(x_1, x_2)|^2 = |\varphi(x_1 - x_2)|^2. \tag{3.34}$$

Pumping procedure

Despite the differences between this model and the system with a single atom discussed in Sec. 3.1, the present system also supports a form of pumping. The energy spectrum (see Fig. 3.11) closely resembles that of the single-atom case. In particular, for a fixed center-of-mass orbital, the energy spectrum exhibits clearly visible branches, which are similar to those observed in the aforementioned one-body system.

By combining it with the following sequence of equalities between certain wavefunctions

$$\begin{cases} \Phi_0(X)\varphi_0(x, \tilde{g} \to \infty) = \Phi_0(X)\varphi_1(x, \tilde{g} \to -\infty), \\ \Phi_0(X)\varphi_1(x, \tilde{g} \to \infty) = \Phi_0(X)\varphi_2(x, \tilde{g} \to -\infty), \\ \quad \vdots \\ \Phi_0(X)\varphi_n(x, \tilde{g} \to \infty) = \Phi_0(X)\varphi_{n+1}(x, \tilde{g} \to -\infty) \end{cases} \tag{3.35}$$

it become evident that implementation of a pumping procedure should be feasible also in that setup.

2 Three particles

Up to this point, the process of pumping and the properties of the states involved have appeared elegant and straightforward. However, we have yet to explain what actually is *Tonks–Girardeau gas* that appears in the title of this thesis. In this section, I aim to increase the complexity of the models under consideration and finally address this gap. Naturally, this added complexity will also introduce some complications to the simple picture of pumping process presented so far.

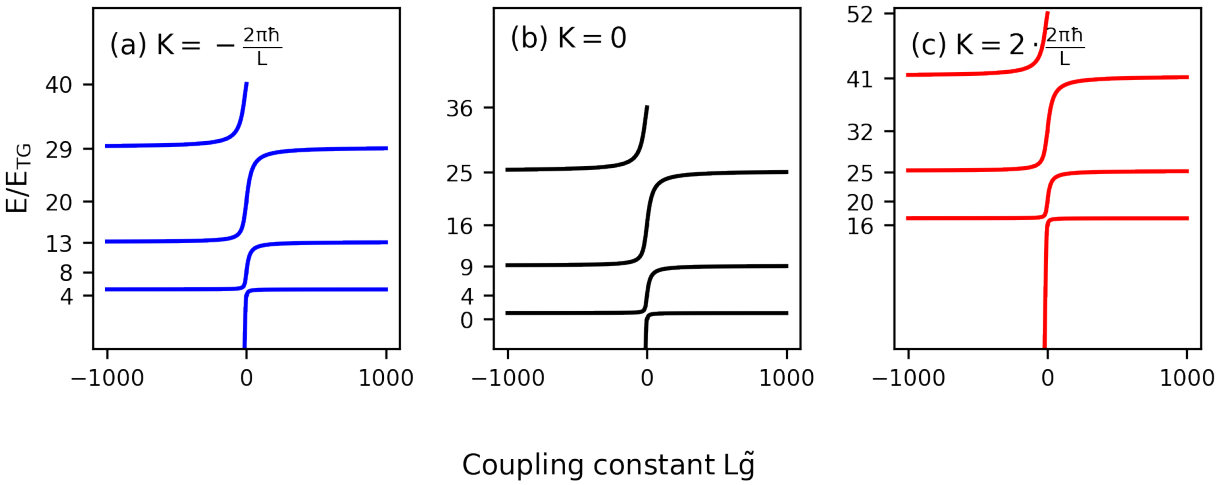

Figure 3.11: The energy spectrum of a system composed of $N = 2$ atoms interacting via contact interactions in a periodic boundary condition box is shown as a function of the interaction strength. The spectrum closely resembles that of a single-particle system; however, a key distinction is the ability to shift the entire spectrum upward by introducing a nonzero total momentum $K \neq 0$. Here, $E_{TG} = \frac{\pi^2\hbar^2 N(N^2-1)}{6mL^2}$ and $\tilde{g} = \frac{mg}{\hbar^2}$.

The first noteworthy difference between the many-body systems and a single atom with the external potential appears for $N = 3$ indistinguishable bosons (in the model with $N = 2$ after separating center of mass motion, the general picture was identical to the predictions made for a single atom). The Hamiltonian of a system of interest is given by

$$\hat{H} = -\frac{\hbar^2}{2m}\sum_{j=1}^{N=3}\frac{\partial^2}{\partial x_j^2} + g\sum_{1\leq i<j}^{N=3}\delta(x_i - x_j), \tag{3.36}$$

where m is the mass of a single particle and g is the coupling constant. As before, positive values of g correspond to repulsive interactions, while negative to attractive ones.

The model we have chosen — namely, bosons interacting via a Dirac delta potential in a box with PBC — offers a significant advantage: it allows for a relatively straightforward determination of the eigenenergies and eigenfunctions $\Psi(x_1, x_2, x_3)$. To achieve this, it is convenient to employ the so-called Bethe Ansatz.

3 Bethe Ansatz

To introduce the basic idea behind the Bethe Ansatz, it is important to realize that the particles described by Hamiltonian (3.36) behave as free ones for the majority of the space. They only "feel each other" when two of them collide. This implies that one can divide the coordinate space into sectors where no two particles occupy the same position. Namely, if we restrict the analysis to regions where the particle positions are ordered (e.g. $x_1 < x_2 < x_3$), the wavefunction in each such sector satisfies the free Schrödinger equation. The interactions are then encoded in the boundary conditions at the hyperplanes where two particles coincide (i.e. $x_i = x_j$), imposed by the contact (delta) interaction.

Due to the absence of interactions within individual sectors, the corresponding wavefunction in each sector takes the form of a *Bethe wavefunction*

$$\Psi(x_1, x_2, x_3) = \sum_P A(P) e^{i(\lambda_{P1} x_1 + \lambda_{P2} x_2 + \lambda_{P3} x_3)}, \tag{3.37}$$

where summation runs over all possible permutations P of a set of $N = 3$ integers.

In that formulation, the problem reduces to determining the allowed values of *rapidities* λ_j and the corresponding amplitudes $A(P)$. There are several methods for achieving this. Here, I will present one approach, which is closely related to the method introduced in the case of a single atom interacting with a delta potential.

Rapidites

To understand the structure of eigenstates in that model, one must consider the implications of periodic boundary conditions. For a system of three particles, the many-body wavefunction satisfies

$$\Psi(x_1 + L, x_2, x_3) = \Psi(x_1, x_2 + L, x_3) = \Psi(x_1, x_2, x_3 + L) = \Psi(x_1, x_2, x_3), \tag{3.38}$$

reflecting the translational invariance of the system. Substituting the Bethe Ansatz wavefunction given in Eq. (3.37) into this condition leads to the appearance of global phase factors

$$\begin{aligned} \Psi(x_1, x_2, x_3) &= \sum_P A(P) e^{i(\lambda_{P1} x_1 + \lambda_{P2} x_2 + \lambda_{P3} x_3)} \\ &= \Psi(x_1 + L, x_2, x_3) = e^{i\lambda_{P1} L} \sum_P A(P) e^{i(\lambda_{P1} x_1 + \lambda_{P2} x_2 + \lambda_{P3} x_3)}, \end{aligned} \tag{3.39}$$

where $e^{i\lambda_{P1} L}$ does not have to be equal to unity, since the rapidities λ_j are not restricted to be integer multiples of $\frac{2\pi}{L}$.

This additional phase can be simply interpreted: when a particle with Lieb's quasi-momentum λ_j completes a full loop around the ring, it accumulates a phase $e^{i\lambda_j L}$. However, due to the presence of interactions, the particle traversing trough system scatters off other particles. Each scattering event introduces a two-body phase shift governed by the S-matrix

$$S(\lambda_j, \lambda_l) = \frac{\lambda_j - \lambda_l - i\tilde{g}}{\lambda_j - \lambda_l + i\tilde{g}}. \tag{3.40}$$

In a full loop, each particle scatters with every other particles (once passing each one), leading to a total accumulated phase

$$\prod_{l=1,\, l\neq j}^{N} S(\lambda_j, \lambda_l) = \prod_{l=1,\, l\neq j}^{N} \left(\frac{\lambda_j - \lambda_l - i\tilde{g}}{\lambda_j - \lambda_l + i\tilde{g}} \right). \tag{3.41}$$

This phase must match the global phase $e^{i\lambda_j L}$ imposed by periodicity, leading to the set of so-called *Bethe equations*

$$e^{i\lambda_j L} = \prod_{l=1,\, l\neq j}^{N} S(\lambda_j, \lambda_l), \quad \text{for } j = 1, \ldots, N. \tag{3.42}$$

Explicitly, for the three-particle case, this gives

$$\begin{cases} e^{i\lambda_1 L} = S(\lambda_2, \lambda_1) S(\lambda_3, \lambda_1), \\ e^{i\lambda_2 L} = S(\lambda_1, \lambda_2) S(\lambda_3, \lambda_2), \\ e^{i\lambda_3 L} = S(\lambda_1, \lambda_3) S(\lambda_2, \lambda_3). \end{cases} \tag{3.43}$$

Logarithmic formulation of the Bethe equations

In the form presented in Eq. (3.43), the equations are relatively complex and challenging to solve numerically. To simplify their numerical treatment, it is convenient to rewrite them in terms of the scattering phase shift $\theta(k)$, defined as

$$S(\lambda_j, \lambda_l) = e^{i\theta(\lambda_j - \lambda_l)}, \quad \theta(\lambda_j - \lambda_l) = -2 \arctan\left(\frac{\lambda_j - \lambda_l}{\tilde{g}} \right). \tag{3.44}$$

Substituting into Eq. (3.42) and taking the logarithm yields

$$\lambda_j L = 2\pi I_j - \sum_{l=1}^{N} \theta(\lambda_j - \lambda_l), \tag{3.45}$$

where I_j are known as *Bethe quantum numbers*, which takes a form of an array of distinct integers (or half-integers for even N) that characterize the solution.

For brevity, I will present the set of Bethe equations relevant for determining the rapidities associated with the ground state in the regime of repulsive interactions. In the three-particle case, the ground state corresponds to the Bethe numbers $I = \{-1, 0, 1\}$, leading to the following system of equations

$$\begin{cases} L\lambda_1 = -2\pi - 2\arctan\left(\frac{\lambda_1-\lambda_2}{\tilde{g}}\right) - 2\arctan\left(\frac{\lambda_1-\lambda_3}{\tilde{g}}\right), \\ L\lambda_2 = \quad 2\arctan\left(\frac{\lambda_2-\lambda_1}{\tilde{g}}\right) - 2\arctan\left(\frac{\lambda_2-\lambda_3}{\tilde{g}}\right), \\ L\lambda_3 = \quad 2\pi + 2\arctan\left(\frac{\lambda_3-\lambda_1}{\tilde{g}}\right) + 2\arctan\left(\frac{\lambda_3-\lambda_2}{\tilde{g}}\right). \end{cases} \tag{3.46}$$

It is straightforward to verify that in this case, the symmetry of the system ensures $k_2 = 0$, and the remaining rapidities satisfy $k_3 = -k_1$. Solving this system yields the rapidities for the ground state, which can then be used to construct the full wavefunction and determine physical observables such as energy and momentum.

Amplitudes A(P)

When rapidities are known, let us focus on the amplitudes $A(P)$. To determine these coefficients, it is crucial to recognize that the exchange of any two particle indices is equivalent to the scattering of one particle off another. Consequently, there arise relation

$$A(..., k, j, ...) = S(\lambda_j, \lambda_k)A(..., j, k, ...). \tag{3.47}$$

This approach alone does not allow for the direct determination of the values of all coefficients $A(P)$, but it can be used to derive relations between the amplitudes corresponding to different permutations. For example, in the case of $N = 3$ bosons, utilizing that relation leads to

$$\begin{cases} A(213) = S(\lambda_2, \lambda_1)A(123) \\ A(132) = S(\lambda_3, \lambda_2)A(123) \\ A(231) = S(\lambda_3, \lambda_1)S(\lambda_2, \lambda_1)A(123) \\ A(312) = S(\lambda_3, \lambda_1)S(\lambda_3, \lambda_2)A(123) \\ A(321) = S(\lambda_3, \lambda_2)S(\lambda_3, \lambda_1)S(\lambda_2, \lambda_1)A(123). \end{cases} \tag{3.48}$$

The value of the final coefficient can be determined by applying normalization to the function. Subsequently, the resulting expression for the coefficients can be derived in the following form

$$A(P) = \prod_{1\le i<j\le N} \left(1 + \frac{i\tilde{g}}{\lambda_{Pi} - \lambda_{Pj}}\right). \tag{3.49}$$

Wavefunction representation in the full spatial domain

The final step — while not strictly necessary, but convenient for latter part of the work — is to generalize Eq. (3.37) so that it applies not only to a single segment but to the entire configuration space. After performing the appropriate algebra, one can derive that

$$\Psi(x_1, x_2, x_3) = \mathcal{N} \sum_P \prod_{k>l} \left(1 - \frac{i\tilde{g}\,\mathrm{sign}(x_k - x_l)}{\lambda_{Pk} - \lambda_{Pl}}\right) e^{i(\lambda_{P1}x_1 + \lambda_{P2}x_2 + \lambda_{P3}x_3)}. \tag{3.50}$$

4 Tonks-Girardeau states

Let me now discuss in more detail the properties of the states derived in the previous section. This time, I will omit the relatively trivial cases of non-interacting atoms and finite values of repulsive forces. The focus here will be on the case where $\tilde{g} \to \infty$. In that regime, one observes that for every state, the rapidities approach

$$\lambda_j \xrightarrow{g\to\infty} \frac{2\pi}{L} I_j, \tag{3.51}$$

what are the allowed values of momenta of a single atoms confined in a PBC box of the length L. Subsequently, wavefunction reduces to

$$\begin{aligned}\Psi(x_1, x_2, x_3) &\xrightarrow{g\to\infty} \\ &\xrightarrow{g\to\infty} \mathcal{N} i \sum_P \left(\frac{\tilde{g}^3\,\mathrm{sign}(x_2 - x_1)\,\mathrm{sign}(x_3 - x_1)\,\mathrm{sign}(x_3 - x_2)}{(\lambda_{P2} - \lambda_{P1})(\lambda_{P3} - \lambda_{P1})(\lambda_{P3} - \lambda_{P2})}\right) e^{i\frac{2\pi}{L}(I_1 x_{P1} + I_2 x_{P2} + I_3 x_{P3})}\end{aligned} \tag{3.52}$$

and, after all

$$\lim_{g\to\infty} \Psi_\lambda(\mathbf{x}) = \frac{1}{\sqrt{N! L^N}} \sum_P \mathrm{sign}\big(\mathrm{P}\big) \exp\left(\mathrm{i} \sum_{\mathrm{m}=1}^{\mathrm{N}} \mathrm{x_m} \frac{2\pi}{\mathrm{L}} \mathrm{I_{Pm}}\right) \prod_{\mathrm{k>l}} \left(-\mathrm{isign}(\mathrm{x_k} - \mathrm{x_l})\right). \tag{3.53}$$

The last term appearing in the wavefunction is independent of the permutation and, as such, can be factored out of the summation

$$\lim_{g\to\infty} \Psi_\lambda(\mathbf{x}) = \left(\prod_{k>l} \left(-i\mathrm{sign}(\mathrm{x_k} - \mathrm{x_l})\right)\right) \cdot \frac{1}{\sqrt{N! L^N}} \sum_P \mathrm{sign}\big(\mathrm{P}\big) \exp\left(\mathrm{i} \sum_{\mathrm{m}=1}^{\mathrm{N}} \mathrm{x_m} \frac{2\pi}{\mathrm{L}} \mathrm{I_{Pm}}\right). \tag{3.54}$$

Noninteracting fermions

The function Eq. (3.54) shares several similarities with the eigenstates of a system of free fermions. Specifically, free fermions, due to the Pauli exclusion principle, cannot occupy the same single-particle orbitals. Consequently, in the ground

state of noninteracting atoms, they occupy the N lowest-lying single-particle orbitals, characterized by the lowest energy. Moreover, their wavefunction must be antisymmetric, which makes it convenient to express it as

$$\Psi_F(x_1, x_2, x_3) = \mathcal{N} \begin{vmatrix} \varphi_1(x_1) & \varphi_1(x_2) & \varphi_1(x_3) \\ \varphi_2(x_1) & \varphi_2(x_2) & \varphi_2(x_3) \\ \varphi_3(x_1) & \varphi_3(x_2) & \varphi_3(x_3) \end{vmatrix} \tag{3.55}$$

what in the more compact form can be written as

$$\Psi_F(x_1, x_2, x_3) = \mathcal{N} \sum_P \mathrm{sign}\Big(\mathrm{P}\Big) \exp\left(\mathrm{i} \sum_{\mathrm{m}=1}^{\mathrm{N}} \mathrm{x_m} \lambda_{\mathrm{Pm}}\right) \tag{3.56}$$

where $\lambda_j = \frac{2\pi j}{L}$.

By comparing it with the wavefunction of infinitely strongly repulsive bosons one can simply realize that the structure of these states is similar, namely

$$\Psi_\lambda(x_1, x_2, x_3) = S(x_1, x_2, x_3)\Psi_{\lambda,F}(x_1, x_2, x_3) \tag{3.57}$$

where $S(\mathbf{x}) = \prod_{k>l} (-i\mathrm{sign}(\mathrm{x_k} - \mathrm{x_l}))$ or, as it is more commonly referred to, the ground state of infinitely repulsive bosons —known as the famous *Tonks-Girardeau state* — is of the form

$$\Psi_{TG}(x_1, x_2, x_3) = |\Psi_{GS,F}(x_1, x_2, x_3)|. \tag{3.58}$$

Tonks-Girardeu state properties

This similarity has significant implications. In particular, since the rapidites of bosons in the Tonks-Girardeau state are identical to the momenta of free fermions, the energies of these states equal, namely $E_{\mathrm{TG}} = E_{GS,F}$. Moreover, similarities also arise in the case of certain correlation functions. Specifically, in the correlations depending only on the module of wavefunction $|\Psi(\mathbf{x})|$, like second-order correlations, there exists an exact mapping (see Fig. 3.12)

$$G_{TG,2}(x, x') = G_{F,2}(x, x'). \tag{3.59}$$

The existence of this simple relation is extremely useful in computing correlations for systems with large numbers of atoms.

Noteworthy, it was not possible to introduce this relation and the term Tonks-Girardeau state earlier. Although we investigated a system with $N = 2$ atoms, no such simple mapping exists. Due to the periodicity of the boundary conditions, only states with an odd number of particles exhibit exact mapping between fermionic and bosonic wavefunctions [74].

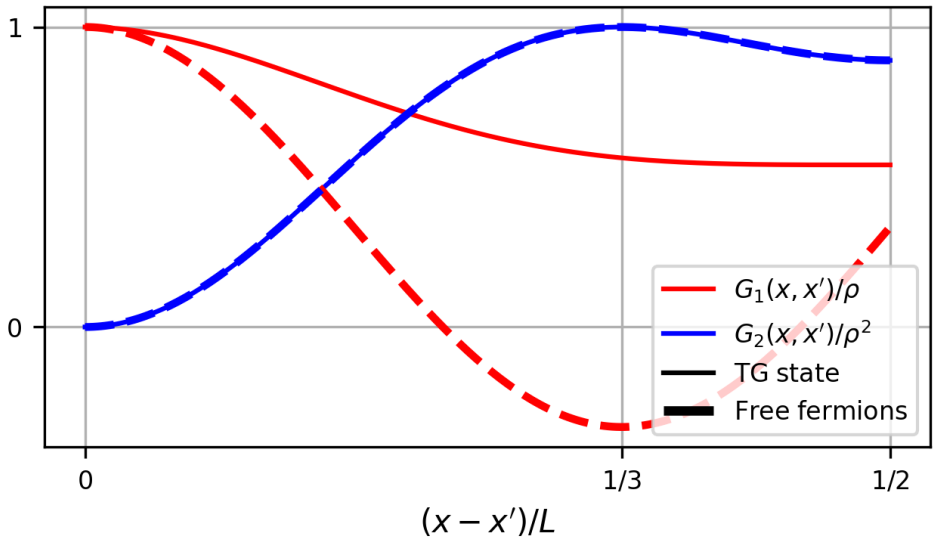

Figure 3.12: Comparison of the first- and second-order correlation functions of a system consisting of $N = 3$ infinitely repulsive bosons and noninteracting fermions.

5 Fully and partially self-bound states

In the previous sections, we focused primarily on systems with repulsive (i.e. positive) interatomic potentials, where particles remained unbound. We now turn to the regime of attractive interactions, $\tilde{g} < 0$, which gives rise to qualitatively distinct behavior. In particular, the system supports the formation of self-bound many-body states.

Returning to Eq. (3.42), one observe that for $\tilde{g} < 0$, the rapidities are no longer restricted to be real-valued; they can acquire complex components. The emergence of complex rapidities signals the formation of bound clusters within the system, i.e. many-body states whose wavefunctions decay exponentially with the relative distance between particles, analogous to single-particle bound states discussed earlier. Below I classify the eigenstates into three main categories, providing illustrative examples of each:

(i) Despite the attractive interaction, even in that regime there exist eigenstates where all rapidities remain real. These states, referred to as not-self-bound (NSB), do not form clusters and resemble their counterparts in the repulsive regime. Remarkably, for a given set of Bethe quantum numbers, the number of NSB states remains unchanged as the sign of $\tilde{g}$ is reversed. These states can be obtained by solving the Bethe equations as in the repulsive case.

(ii) In contrast, fully self-bound states are those in which all particles form a single bound cluster. The most prominent example is the *McGuire soliton* [16], which constitutes the ground state of the system in the attractive regime. For a three-particle system, the corresponding rapidities take the form

$$\begin{cases} \lambda_1 = K - ig, \\ \lambda_2 = K, \\ \lambda_3 = K + ig, \end{cases} \tag{3.60}$$

where K denotes the total center-of-mass momentum. The associated eigenfunction exhibits exponential decay in the relative coordinates. The energy of this state is given by $E_{MG} = \frac{\hbar^2}{2m}K^2 - \frac{g^2 m}{24\hbar^2}N(N^2-1)$, representing the lowest-energy configuration for $g < 0$.

(iii) A third class of eigenstates — partially self-bound (PSB) states — arises when only a subset of the particles form a bound cluster, while the remaining particles are effectively unbound. For instance, in a three-body system, two particles may form a bound pair while the third remains delocalized. The corresponding rapidities take a mixed form, for example such as

$$\begin{cases} \lambda_1 = k/2 - ig/2, \\ \lambda_2 = k/2 + ig/2, \\ \lambda_3 = q, \end{cases} \tag{3.61}$$

where λ_1 and λ_2 form a bound pair and λ_3 corresponds to the "free" particle. The analytical characterization of such states is significantly more involved and generally requires numerical methods.

These states are particularly problematic from the perspective of pumping procedure, and they likely prevent the implementation of reverse processes of *re-pumping*. Their energies are equal to $E = \frac{\hbar^2}{2m}(\lambda_1^2 + \lambda_2^2 + \lambda_3^2) = \frac{\hbar}{m}\frac{k^2+2q^2-g^2}{4}$ and can become degenerate with, and even cross, those of the NSB states, as illustrated in Fig. 3.13.

While such crossings do not affect significantly the pumping process from a theoretical standpoint, they introduce instabilities in realistic experimental settings. These instabilities can lead to the collapse of an initially prepared NSB state due to the spontaneous formation of partially self-bound configurations.

Historically, this instability was a key reason why the possibility of implementing a pumping cycle remained unrecognized for many years. Early studies on

super-Tonks–Girardeau states, both numerical [17] and experimental [36], reported a rapid collapse of the super-Tonks-Girardeau state in the regime of the intermediately attractive interactions, reinforcing the belief that such pumping procedures were infeasible.

A major breakthrough occurred with the use of dysprosium atoms [43], which interact not only via contact interactions but also via weak, nonlocal dipolar forces. These dipolar interactions introduce a weak effective long-range repulsion into the system, which helps stabilize the dynamics and enables the successful execution of several pumping cycles in the laboratory. However, the precise theoretical understanding of how this additional repulsion modifies the system's behavior remains an open question and requires further investigation.

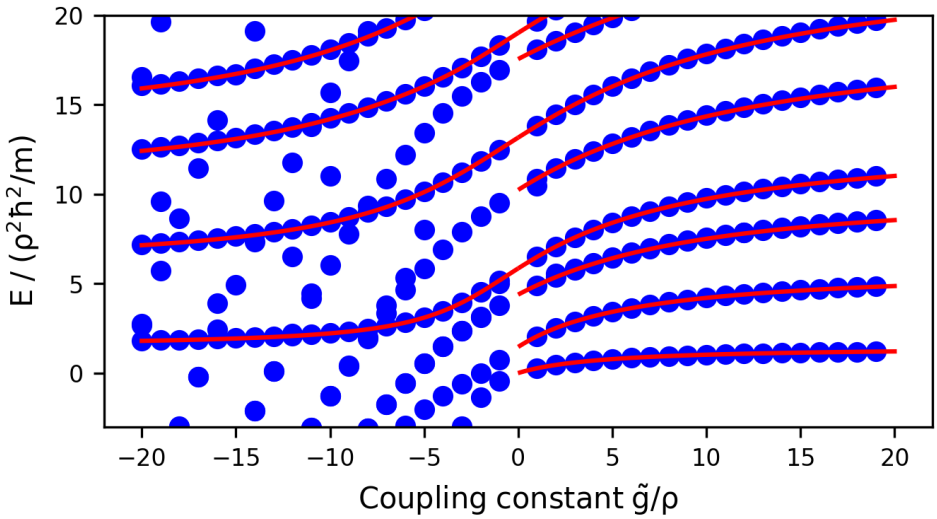

Figure 3.13: The energy spectrum of a system consisting of $N = 3$ bosons interacting via contact interactions. A detailed analysis reveals three distinct types of eigenstates: (i) non-self-bound states, (ii) partially bound states where two particles form a bound pair, and (iii) fully self-bound states where all three particles are mutually bound. Blue dots represent the energies obtained via exact diagonalization (see Sec. 2.1) with a momentum cutoff set to $k_{\max} = 200$, while red lines indicate the energies of the non-self-bound states computed using the Bethe Ansatz.

3.3 Lieb-Liniger model

In this section, I will extend scope of studies from few- to many-body systems. I focus on a system consisting of N indistinguishable bosons of mass m confined in a one-dimensional box of length L with periodic boundary conditions. As in the previous sections, the particles interact via short-range forces modeled by a Dirac delta potential. This system, known as the Lieb-Liniger model [13, 14], has been the subject of extensive study and is one of the few quantum many-body systems considered exactly solvable. From a physical perspective, the Hamiltonian of this model is given by

$$\hat{H} = -\frac{\hbar^2}{2m}\sum_{j=1}^{N}\frac{\partial^2}{\partial x_j^2} + g\sum_{j<j'}^{N}\delta(x_j - x_{j'}), \tag{3.62}$$

where g is the coupling constant. Using the Bethe Ansatz (discussed earlier in Sec. 3), it is possible to show that all non-self-bound (NSB) eigenstates of this Hamiltonian are of the form of[75, 76]

$$\Psi_\lambda(\mathbf{x}) = A_\lambda \sum_P \exp\left(i\sum_{m=1}^{N} x_m \lambda_{Pm}\right)\prod_{k>l}\left(1 - \frac{i\tilde{g}\,\mathrm{sign}(\mathrm{x_k} - \mathrm{x_l})}{\lambda_{Pk} - \lambda_{Pl}}\right), \tag{3.63}$$

with normalization factor given by

$$A_\lambda = \frac{\prod_{k>l}(\lambda_k - \lambda_l)}{\sqrt{N!\det(M_\lambda)\prod_{k>l}((\lambda_k - \lambda_l)^2 + \tilde{g}^2)}} \tag{3.64}$$

where elements of the matrix M are defined as

$$[M_\lambda]_{kl} = \delta_{kl}\left(L + \sum_{m=1}^{N}\frac{2\tilde{g}}{\tilde{g}^2 + (\lambda_k - \lambda_m)^2}\right) - \frac{2\tilde{g}}{\tilde{g}^2 + (\lambda_k - \lambda_l)^2} \tag{3.65}$$

with corresponding energies E and total momenta P given as

$$E_\lambda = \frac{\hbar^2}{2m}\sum_{i=1}^{N}\lambda_j^2 \quad \text{and} \quad \mathrm{P}_\lambda = \hbar\sum_{\mathrm{j}=1}^{\mathrm{N}}\lambda_{\mathrm{j}}. \tag{3.66}$$

The properties of these states depend on a set of N parameters $\{\lambda_i\}$, known as Lieb's quasimomenta or rapidities. A significant advantage of LL model is that these values can be relatively easily computed by solving a set of nonlinear equations, where $j-th$ rapidity is given by Eq. (3.67)

$$L\lambda_j = 2\pi I_j - 2\sum_{i=1}^{N}\arctan\left(\frac{\lambda_j - \lambda_i}{\tilde{g}}\right). \tag{3.67}$$

As one can see, the Lieb's quasimomenta depend not only on the length of the system and the interaction strength, but also on a set of N Bethe quantum numbers, denoted $\{I_i\}$. For systems with an even (odd) number of particles, these Bethe numbers form a set of distinct integers (half-integers). Crucially, for any given set of Bethe numbers $\mathbf{I}$, there exists a unique set of rapidities $\boldsymbol{\lambda}$, and consequently a unique eigenstate of the system. This means that the Bethe numbers can be used to unambiguously label the eigenstates of the Hamiltonian (3.62).

The notation involving Bethe numbers is convenient also for a different reason. In particular, the distribution of these numbers determines the total momentum of the system. As can be shown,

$$P = \hbar \sum_j \lambda_{j=1}^N = \frac{2\pi\hbar}{L} \sum_{j=1}^N I_j - \frac{2\hbar}{L} \sum_{i,j=1}^N \arctan\left(\frac{\lambda_j - \lambda_i}{\tilde{g}}\right). \tag{3.68}$$

As the arc tangent function is antisymmetric, the last term in Eq. (3.68) vanishes and the total momentum is proportional to the sum of Bethe numbers

$$P = \frac{2\pi\hbar}{L} \sum_{j=1}^N I_j. \tag{3.69}$$

This implies that, since we are primarily interested in states with total momentum equal to zero $P = 0$, we can restrict our analysis to those states for which the sum of the Bethe numbers is zero.

1 Pumping procedure in LL model

Utilizing the exact expressions for the energies and wavefunctions introduced above, it is possible to demonstrate that the pumping procedure can also be applied in this setup. To illustrate this, let us begin by examining the energy spectrum of a system with $N = 5$ atoms. As shown in Fig. 3.14, for every set of Bethe numbers, there exist two energy branches: one corresponding to positive and the other to negative values of the coupling constant. It can be simply proven that adiabatic evolution between any two states belonging to the same branch is possible by continuously varying the coupling constant.

Moreover, an sTG quench allows for the transformation of a state obtained in the $\tilde{g} \to \infty$ limit into a state characterized by the same set of Bethe numbers in the $\tilde{g} \to -\infty$ regime. To demonstrate this, let us examine the behavior of the rapidities in these two limits. As seen in equation Eq. (3.67), the coupling constant appears

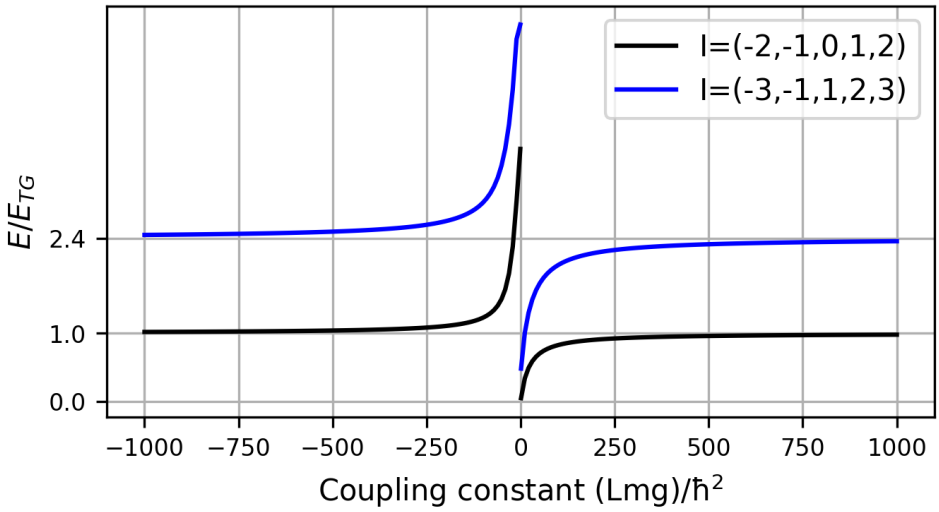

Figure 3.14: Energies of two distinct eigenstates of the Lieb-Liniger Hamiltonian with $N = 5$ particles as a functions of the coupling constant $\tilde{g}$. For both sets of Bethe quantum numbers, the energy spectra exhibit two disconnected branches corresponding to attractive ($\tilde{g} < 0$) and repulsive ($\tilde{g} > 0$) interactions. Notably, in the limit $|\tilde{g}| \to \infty$, the energies of the left and right branches converge to the same value. Here, $E_{\mathrm{TG}} = \frac{\pi^2\hbar^2 N(N^2-1)}{6mL^2}$.

only in the denominator of the arctangent function. Substituting large values of $\tilde{g} \to \pm\infty$ causes these terms to vanish, regardless of the sign of the interaction. As a result, the Lieb's quasimomenta and energy remain effectively unchanged across the quench, namely

$$\lambda_j \xrightarrow{\tilde{g}\to\pm\infty} \frac{2\pi}{L} I_j. \tag{3.70}$$

Since the rapidities are identical in both cases, the corresponding wavefunctions are also the same. Referring to Eq. (3.63), we can see that in the limit of strong interactions, the wavefunction simplifies to

$$\Psi_\lambda(\mathbf{x}) \xrightarrow{\tilde{g}\to\pm\infty} \tilde{g}^{\frac{N(N-1)}{2}} \mathcal{N} \sum_P \exp\left(i \sum_{m=1}^{N} x_m \lambda_{Pm}\right) \prod_{k>l} \left(-\frac{i\,\mathrm{sign}(\mathrm{x_k} - \mathrm{x_l})}{\lambda_{Pk} - \lambda_{Pl}}\right). \tag{3.71}$$

Changing the sign of the interaction affects only the overall sign of the wavefunction, without altering its internal structure. Combining this observation with the possibility of adiabatic evolving between states within the same energy branch, it becomes clear that one can transform a state at one interaction strength into another — via the pumping protocol — as long as both states are labeled by the same set of Bethe numbers.

To continue that analysis let us examine the lower part of the spectrum, which includes non-self-bound states of a system with $N = 5$ atoms (see Fig. 3.15(a)). As shown, the energy spectrum is composed of multiple branches. Fortunately, some of these branches are connected at the point where $g = 0$ (see Fig. 3.15(b)). In the case investigated here, the branch connected to the ground state (labeled by $\mathbf{I^0} = \{-2, -1, 0, 1, 2\}$) is indexed by $\mathbf{I^1} = \{-6, -3, 0, 3, 6\}$. Then, that branch is connected to the higher one indexed by $\mathbf{I^2} = \{-10, -5, 0, 5, 10\}$, et cetera.

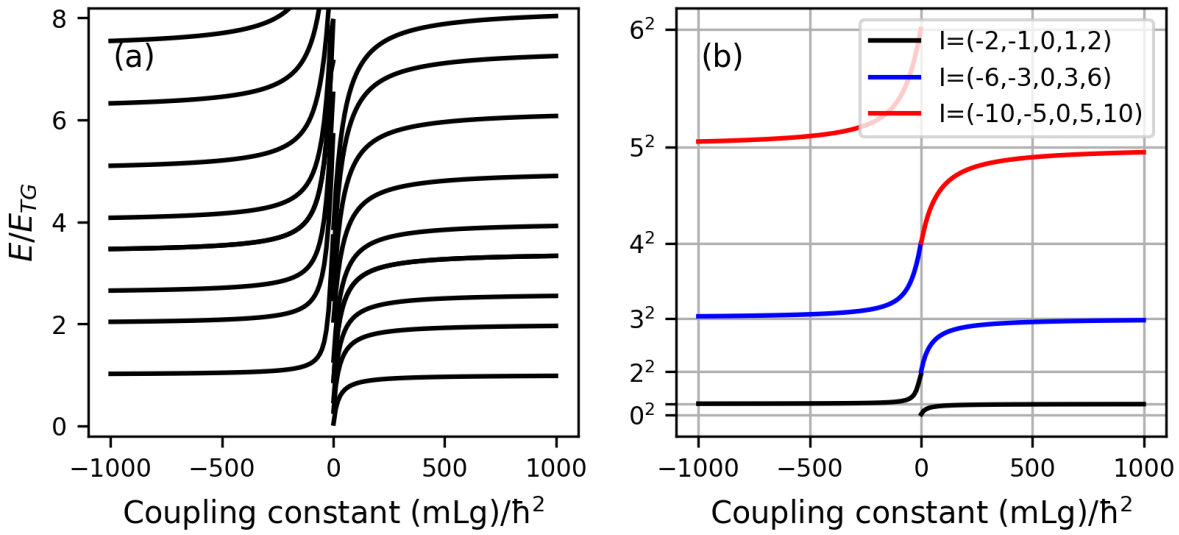

Figure 3.15: (a) Lowest energy levels of the non-self-bound states in the Lieb-Liniger model for $N = 5$ bosons. As observed, several energy branches are connected at the point $g = 0$, corresponding to the non-interacting limit. (b) A detailed view of the energy branches connected to the ground state, highlighting their evolution with interaction strength.

A clear pattern emerges here. As observed, the ground state — characterized by an uniform and symmetric distribution of Bethe numbers with a spacing of $d = I_{n+1} - I_n = 1$ — is connected to a state with the same uniform and symmetric structure but with a spacing of $d = 3$. This state, in turn, connects to another wavefunction where the Bethe numbers are again uniformly and symmetrically distributed, but with an increment of $d = 5$.

As can be proven, this observation is correct, and the pattern can be generalized to systems with any number of atoms and for higher branches. To demonstrate this, let us take a closer look at the energy of states corresponding to uniformly distributed

Bethe numbers of the form $I = \{0, \pm d, \pm 2d, ..., \pm(N-1)d/2\}$. The rapidities in this case are given by

$$L\lambda_j \xrightarrow{\tilde{g}\to 0} 2\pi I_j - \pi \sum_{i=1}^{N} \text{sign}\Big(g(\lambda_j - \lambda_i)\Big). \tag{3.72}$$

This equation can be simplified by realizing that j-th element of the set equals $I_j = -(N-2j-1)d/2$ and that the summation results in $\sum_{i=1}^{N} \text{sign}\Big(\tilde{g}(\lambda_j - \lambda_i)\Big) = \text{sign}(\tilde{g})(N-2j+1)$. Substituting these equalities into Eq. (3.72) one obtain

$$\begin{cases} L\lambda_j \xrightarrow{\tilde{g}\to 0^-} -\pi(N-2j+1)(d+1) + 2\pi d \\ L\lambda_j \xrightarrow{\tilde{g}\to 0^+} -\pi(N-2j+1)(d-1) + 2\pi d. \end{cases} \tag{3.73}$$

As can be seen, in the limit of vanishing interactions ($\tilde{g} \to 0$), the rapidities in the branch where the spacing between neighboring numbers in the set $\{I_j\}$ is $I_{j+1} - I_j = d$ are equal to those in the branch $\{I'_j\}$, where the differences are given by $I'_{j+1} - I'_j = d + 2$. It means that the branch corresponding to the ground state of atoms in the regime of positive coupling constants, characterized by Bethe numbers with an increment of $d = 1$, has the same rapidity distribution for $\tilde{g} \to 0^+$ as the distribution in the branch with $d = 3$. This branch will then connect to the branch with a spacing of $d = 5$. As the energy of the system is proportional to the sum of the squared rapidites, so the equality of their distribution explains observed in Fig. 3.15 similarities in the energy.

Noteworthy, not only energies of these states converges at $\tilde{g} \to 0$. The analogous convergence can be observed in the wavefunctions. By incorporating Lieb's quasimomenta found in Eq. (3.73) to the general formula Eq. (3.63), one can simply prove that at this point wavefunctions labelled by appropriate sets of Bethe numbers are identical

$$\begin{cases} \Psi_{I=\{0,\pm 1,\pm 2,...\}}(\mathbf{x}, \tilde{g} \to 0^-) = \Psi_{I'=\{0,\pm 3,\pm 6,...\}}(\mathbf{x}, \tilde{g} \to 0^+) \\ \Psi_{I=\{0,\pm 3,\pm 6,...\}}(\mathbf{x}, \tilde{g} \to 0^-) = \Psi_{I'=\{0,\pm 5,\pm 10,...\}}(\mathbf{x}, \tilde{g} \to 0^+) \\ ... \\ \Psi_{I=\{0,\pm d,\pm 2d,...\}}(\mathbf{x}, \tilde{g} \to 0^-) = \Psi_{I'=\{0,\pm(d+2),\pm 2(d+2),...\}}(\mathbf{x}, \tilde{g} \to 0^+). \end{cases} \tag{3.74}$$

Adding this information to our existing knowledge, it becomes clear that the pumping process should be feasible for a system with any number of atoms N.

2 Changes in internal structure of the gas in the process of pumping

In this section, I will examine in greater detail the internal structural changes of the state that occur during the pumping process. I begin by analyzing the distribution of rapidities. Continuing with the case of $N = 5$ atoms, the structure observed in the Bethe quantum numbers leads to a characteristic distribution of Lieb's quasi-momenta, as illustrated in Fig. 3.16(c). As shown in the figure, in

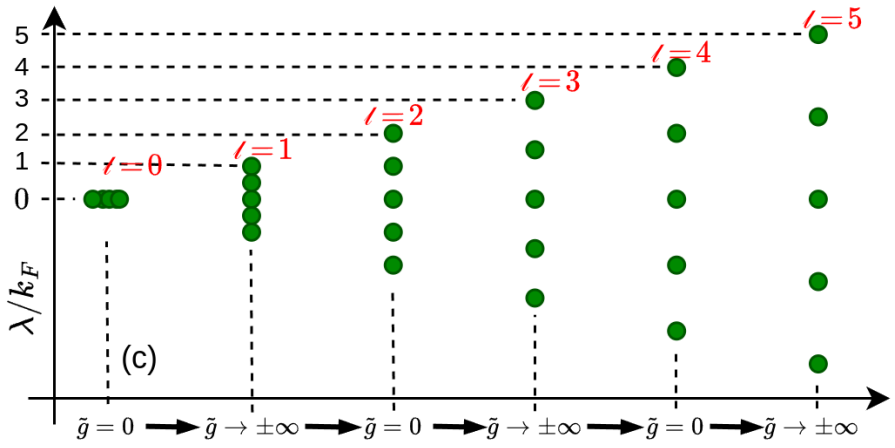

Figure 3.16: The evolution of rapidities (Lieb's quasimomenta) in a system of $N = 5$ bosons interacting via a contact potential during the pumping process. Here, we define Fermi momentum as $k_F = (N-1)\pi/L$

the ground state of a non-interacting gas ($\tilde{g} = 0$, $\ell = 0$), all quasi-momenta are zero ($\lambda_i = 0$), reflecting a macroscopic occupation of the zero-momentum mode. For a finite and positive interaction strength ($\tilde{g} > 0$), rapidities begin to separate. Then, as the system approaches the fermionization limit ($\tilde{g} \to \infty$, $\ell = 1$), it enters the Tonks-Girardeau regime, where the quasi-momenta adopt a uniform distribution, mirroring the momentum distribution of the ground state of non-interacting fermions.

This distribution remains unchanged during the quench; however, when the interaction strength is tuned back from $\tilde{g} = -\infty$ to $\tilde{g} = 0$, the quasi-momentum distribution further broadens and ultimately, for non-interacting bosons once again resembles distribution of non-interacting fermions, but with twice lager the spacing. Specifically, it consists of equally spaced values with spacing increased by a factor of $\ell = 2$, i.e. $2 \cdot (2\pi/L)$. As the system undergoes successive pumping cycles, the quasi-momentum distribution experiences a continuous stretching.

In conclusion, during the pumping process, the states at the special interaction points $\tilde{g} = 0$ and $\tilde{g} = \pm\infty$ exhibit rapidity distributions that correspond to the momentum distribution of the ground-state Fermi gas, but scaled by a factor of ℓ.

The rescaling of the quasi-momentum distribution is reflected in the structure of the wave function of excited states. By introducing the operator $\hat{S}$, defined as

$$\hat{S}\Psi(x_1, \ldots, x_N) = \prod_{i<j} \mathrm{sign}(x_j - x_i)\, \Psi(x_1, \ldots, x_N), \tag{3.75}$$

the wave function at successive stages of the evolution, corresponding to $\ell = 0, 1, \ldots$, can be expressed as follows

$$\begin{array}{c} \underbrace{|\ldots, 0, 0, N, 0, 0, \ldots\rangle^B}_{\text{Ground state, } \ell=0} \xrightarrow{g\to\infty} \hat{S}\ \underbrace{|\ldots, 1, 1, 1, \ldots\rangle^F}_{\text{Tonks-Girardeau, } \ell=1} \\ 0 \leftarrow -\infty \leftarrow g \\ \rightarrow |\ldots, \underbrace{1, 0}_{\ell=2}, 1, 0, 1 \ldots\rangle^B \xrightarrow{g\to\infty} \hat{S}|\ldots, \underbrace{1, 0, 0}_{\ell=3}, 1, 0, 0, 1 \ldots\rangle^F \rightarrow \ldots \end{array} \tag{3.76}$$

where, $|\ldots\rangle^{B(F)}$ is the bosonic (fermionic) Fock state, where single particle orbitals are the plane waves.

3 Momentum distribution

Finally, having discussed the quasi-momenta, we are well-positioned to begin the discussion of real momenta in the system. By definition, the momentum distribution $n(p)$ — the expected number of atoms occupying a given momentum — can be defined as

$$n(p) = \int_0^L e^{-ip(x-x')} G_1(x, x') dx \tag{3.77}$$

where the single-particle density matrix is given by

$$G_1(x, x') = \int_0^L \Psi^*(x', x_2, x_3, ..., x_N)\Psi(x, x_2, x_3, ..., x_N) dx_2 ... dx_N. \tag{3.78}$$

Calculating this function for the Lieb-Liniger model with finite interactions ($g \neq 0$) is relatively complex and requires numerical attempts. However, for few-body systems, such as model with $N = 9$ atoms, it is feasible. By applying the procedure described in detail in [76], I computed the single-particle density matrices and subsequently the momentum distributions for several characteristic points in the pumping process. The results are presented in Fig. 3.17.

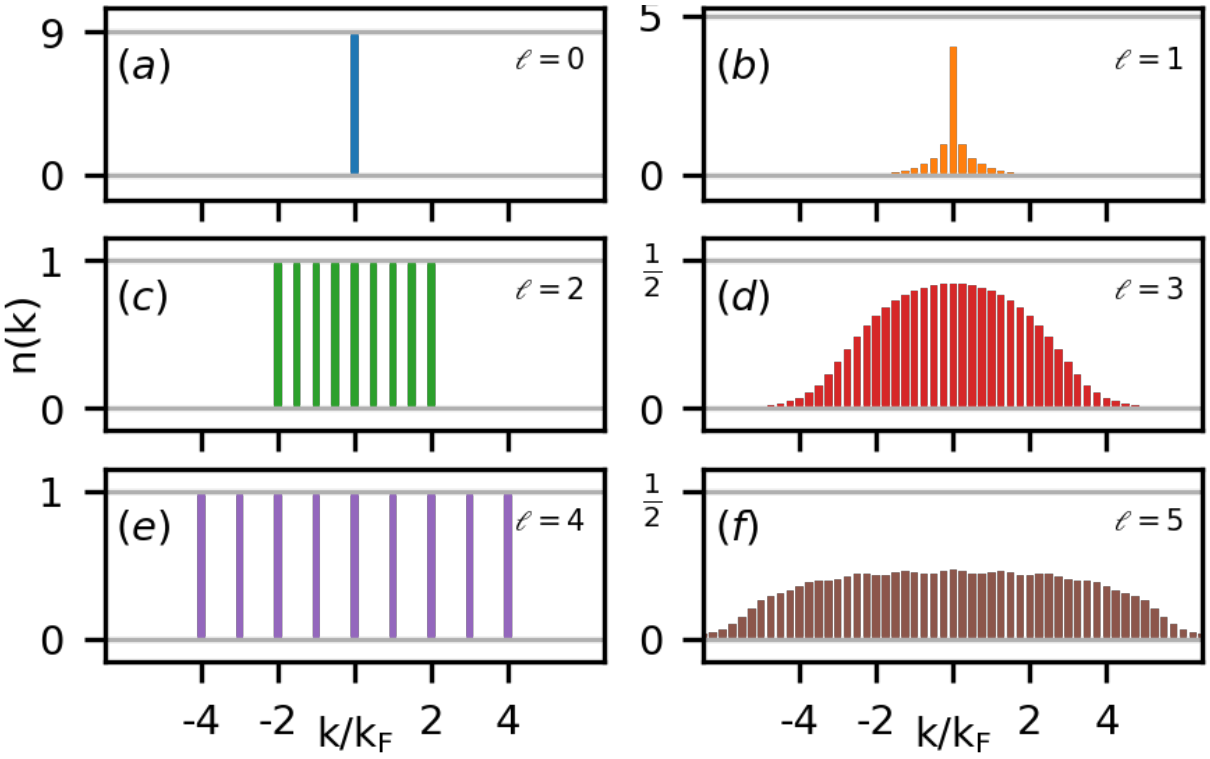

Figure 3.17: Momentum distributions of states appearing in the process of pumping at $\tilde{g} = 0$ (left column) and $\tilde{g} = \pm\infty$ (right column) at the subsequent branches of the pumping labeled with $\ell = 0, 1, 2, 3, 4, 5$. Here, we considered $N = 9$ atoms and we define Fermi momentum as $k_F = (N-1)\pi/L$.

What can be observed there is that at the beginning of the pumping process, in the ground state, all atoms occupy the single-particle orbital with momentum equal to 0. As the interaction strength increases, the momentum spectrum broadens, eventually reaching a shape characteristic for the Tonks-Girardeau state [77, 78, 79]. Then, after a quench to the excited state, the momentum spectrum continues to getting wider. However, at a certain point, N distinct peaks emerge in the spectrum, and the momentum distribution between them begins to decay. Finally, for the excited state of non-interacting bosons ($\tilde{g} = 0$) labeled by $\ell = 2$, the momentum distribution consists of N peaks, each corresponding to a single occupying atom. As shown, the peaks correspond to momenta given by $0, \pm\frac{4\pi}{L}, \pm\frac{8\pi}{L}, \pm\frac{12\pi}{L}, \pm\frac{16\pi}{L}$. A similar behavior can also be observed for pumping to higher excited states, where the cycle eventually ends with peaks corresponding to momenta $0, \pm\frac{8\pi}{L}, \pm\frac{16\pi}{L}, \pm\frac{24\pi}{L}, \pm\frac{32\pi}{L}$.

As can be observed, in the non-interacting regime, the momenta of the atoms coincide with their rapidities. This observation is indeed accurate: for

non-interacting bosons, the rapidities directly correspond to the momenta of individual atoms. Consequently, the pumping process effectively enables the transformation of a system of non-interacting atoms from its ground state to a highly excited state of an ideal Bose gas, in which the momentum distribution resembles that of non-interacting fermions, scaled by a factor of ℓ.

It is worth of highlighting that this is not the only valid interpretation. The excited states reached through the pumping process, which exhibit a momentum distribution identical to a rescaled Fermi sea, can alternatively be understood as corresponding to a Fermi sea in a system with a rescaled spatial extent. For example, in the state labeled by $\ell = 2$, the momentum modes occupied by the atoms are precisely those that would be filled in the ground state of a non-interacting Fermi gas confined in a periodic box of length $L/2$.

4 Interparticle correlations in a pumping procedure

This intuition — the effective shortening of the box — appears to be correct. To show that, let us examine the spatial structure of the gas in more detail. Although the system is subject to periodic boundary conditions and experiences no external potential (despite the trapping one), the gas density remains uniform. However, the correlations between atoms do not share this uniformity.

Starting with the previously discussed first-order correlation function — as shown in Fig. 3.18 — we observe that as the pumping process crosses successive characteristic points, the function appears to become narrower. While this might sound like a colloquial and mathematically meaningless statement, it captures the underlying fact that the decay of correlations becomes faster, and the oscillations in the function become more frequent.

Moreover, at certain points the correlation structure becomes “self-similar“ in a sense that the function obtained at $\ell = 2$, namely $G_1(x, \ell = 2)$, is essentially a rescaled (twice as broad) version of the function corresponding to $\ell = 4$

$$G_1(x, \ell = 2) = G_1(2 \cdot x, \ell = 4). \tag{3.79}$$

This observation can be readily confirmed and generalized to systems of arbitrary size and to higher branches. In particular, it can be shown that for non-interacting

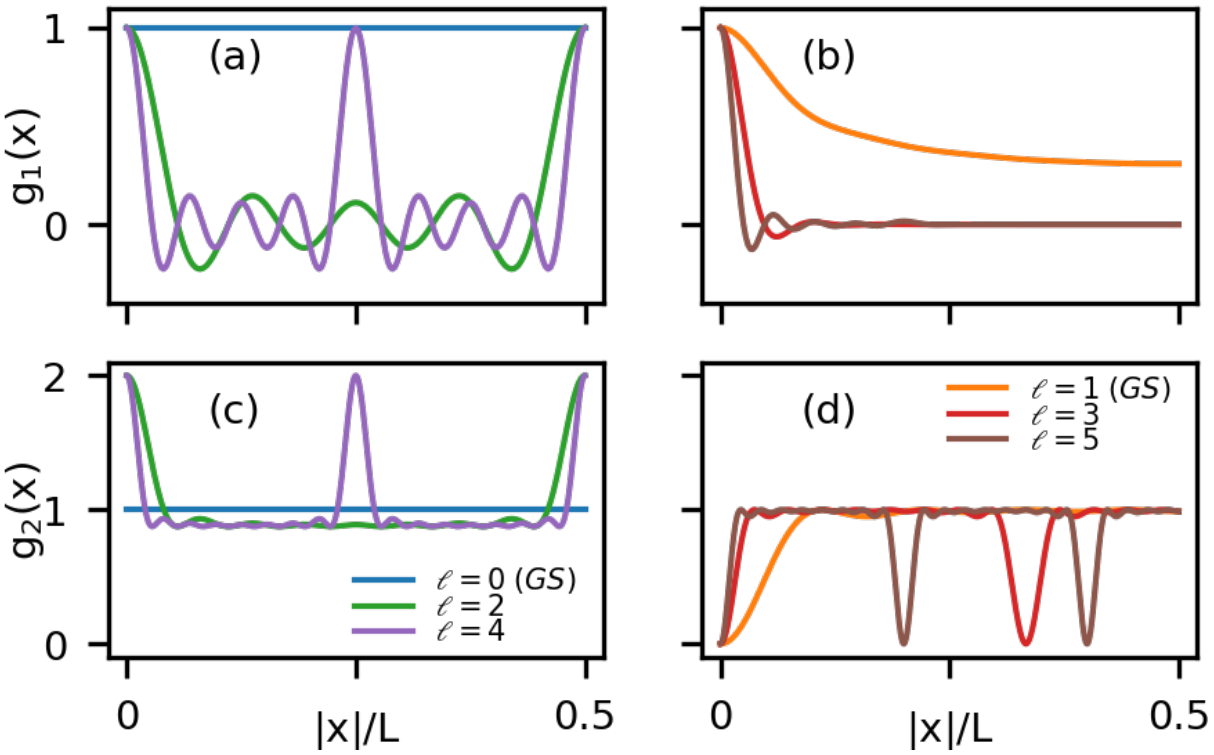

Figure 3.18: The first and the second order correlation functions of the states appearing in the process of pumping at $\gamma = 0$ (left column, $\ell = 0,\ 2,\ 4$) and $\gamma = \pm\infty$ (right column, $\ell = 1,\ 3,\ 5$). Top panels: the first-order correlation g_1, the bottom: g_2. Results shown for $N = 9$ atoms.

bosons, the OBDM takes the form

$$G_{1,\text{even }\ell}(x) = \frac{1}{L}\sum_{j=-\lfloor N/2\rfloor}^{\lfloor N/2\rfloor} e^{\frac{i2\pi j\ell x}{L}} = \frac{\sin(N\pi\ell x/L)}{L\sin(\pi\ell x/L)}. \tag{3.80}$$

As one can see there, rescaling of the momenta in that equation yields the same result as scaling the spatial coordinates.

Contrary, in the regime of strongly repulsive interactions, the scaling patterns become more subtle and harder to observe. However, the short-range behavior of the correlation function still obeys a simple scaling property. Specifically, it can be shown that function $g_1(x) = G_1(x)/\rho$ is given by

$$\begin{cases} g_{1,even\ \ell}(x) = 1 - \frac{(\pi\ell)^2(1-\frac{1}{N^2})}{6}(\rho x)^2 + O(x^4) \\ g_{1,odd\ \ell}(x) = 1 - \frac{(\pi\ell)^2(1-\frac{1}{N^2})(\rho x)^2}{6} + \frac{(\pi\ell)^2(1-\frac{1}{N^2})|\rho x|^3}{9} + O(x^4). \end{cases} \tag{3.81}$$

As one can see, in the regime of $x \ll L$ the correlation decay rate scales proportionally with the pumping level.

Second-order correlation function

A similar type of "scaling" behavior can also be observed in the second-order correlation function, defined as

$$G_2(x, x') = \iint_{\mathcal{S}} dx_3 \dots dx_N \, |\Psi(x, x', x_3, x_4, \dots, x_N)|^2, \tag{3.82}$$

As shown in Fig. 3.18(c,d), the excited states exhibit "self-similar" segments in the correlation function. In the case of a noninteracting Bose gas, these segments are characterized by local maxima, which can be interpreted as an enhanced probability of finding two particles either in close proximity or at well-defined distances given by $x - x' = nL/\ell$, where $n \in \mathbb{Z}$. Conversely, for the case of infinitely strong repulsion, the system exhibits local minima in the G_2 function at those same distances, indicating that it is forbidden to find two particles at the same location or at distances $x - x' = nL/\ell$.

What is particularly interesting is that the G_2 function for noninteracting bosons is qualitatively different from that of free fermions. In the excited states of the Bose gas, we observe significant bunching, a feature that cannot occur for free fermions. This is especially intriguing in the context of the first-order correlation function, which in these states closely resembles that of free fermions. This contrast can be intuitively understood as a novel form of fermionization: for strongly repulsive bosons in the Tonks–Girardeau regime, both the second-order correlation function and the energy resemble those of a noninteracting Fermi gas. In contrast, here, the excited states of the ideal Bose gas, while exhibiting first-order correlations and energy spectra similar to the fermionic case, display fundamentally different second-order correlations.

3.4 Summary

In this chapter, I have discussed the effects of a quench of either the potential or the interatomic interaction strength from strongly repulsive to highly attractive values. I have shown that, regardless of whether one considers a single atom or a larger ensemble of ultracold particles, such a quench leads to the formation of highly excited, stable states. When combined with adiabatic changes of the interaction parameter, this procedure, called as *pumping*, enables the preparation of strongly correlated, highly excited many-body states with nontrivial internal structure. Notably, in the regime of non-interacting bosons, the resulting states exhibit properties closely resembling those of free fermions confined in spatially

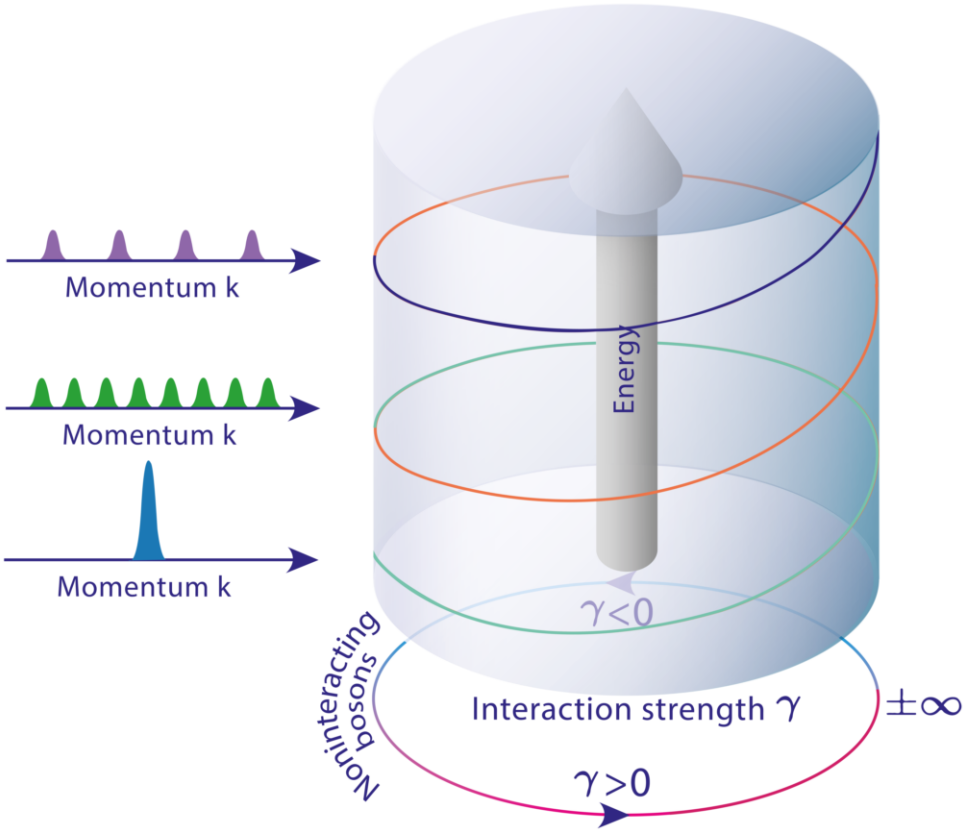

Figure 3.19: Illustration of the "tower of states" emerging during cyclical changes in the interaction parameter $\gamma = \tilde{g}/\rho$, shown as a circle on the bottom in a stereographic representation with $\pm\infty$ being a single point. Left panels: the characteristic comb-like momentum distribution in the appearing excited states of an ideal Bose gas. The colors of the helical line correspond to different pumping cycles.

compressed traps. A simple but entirely accurate summary of these results may be provided by a schematic illustration shown in Fig. 3.19, depicting the "tower of states" formed during the pumping process.

Despite these findings, the completion of this study leaves me with more questions than I had at the beginning. The interpretation of the unusual interatomic correlations observed in the pumped states remains an open and intriguing problem. Moreover, it is still unclear how the presence of a trapping potential affects the nature of these states. The current work focused primarily on systems with either periodic boundary conditions or no external confinement in one dimension. However, the observed structural similarities to bosonic systems confined in

hard-wall boxes [80] suggest that analogous phenomena may also emerge in such settings.

Furthermore, experimental realizations of the pumping protocol, as described in Refs. [43, 41, 42], indicate that similar effects may occur even in harmonic traps. This is supported by several theoretical investigations [24, 81], which reinforce the probability of such behavior. Nevertheless, a rigorous mathematical understanding of this mechanism in systems with a significant number of particles is still lacking. It remains an open question whether the behavior observed there would be fundamentally connected to the peculiar form of “fermionization“ characteristic of the systems analyzed in this work.

Chapter 4

Super-Tonks-Girardeau effect in models with two types of interactions

This chapter is dedicated to the analysis of a second nontrivial phenomenon emerging in many-body quantum systems, closely related to the super-Tonks-Girardeau quench — the so-called *super-evaporation* effect.

Before going further, I would like to highlight that most of the material presented here was gathered as part of a project concluded in the work [82], in collaboration with my supervisor and teammates, whose contributions greatly influenced the final structure of the project. In this thesis, for educational purposes I added the section explaining the rudiments of the effect described in the original work for a single atomic case. Additionally, I have made slight adjustments to the notation, particularly to align it with the description of the pumping procedure. However, most of the figures and the logical structure of the text remain in the form presented in the original article.

4.1 Single atom and three delta potential

Following a successful strategy employed previously, to lay the groundwork for this discussion, I begin by considering a simplified model: a single particle of mass m in an infinite one-dimensional space. In contrast to the earlier scenario discussed in Chapter 3, this time the external potential consists of three Dirac delta functions symmetrically distributed around the point $x = 0$ (see Fig. 4.1). Consequently,

Hamiltonian of the system can be expressed as Eq. (4.1)

$$\hat{H} = -\frac{\hbar^2}{2m}\partial_x^2 + g_c\delta(x) + g_s\Big(\delta(x-d) + \delta(x+d)\Big), \tag{4.1}$$

where d denotes the distance between the potential peaks, while the parameters g_c and g_s represent the coefficients of the central and side delta potentials, respectively. In this study, I focus on scenarios where the side potentials are weakly attractive while the central one is strongly attractive or strongly repulsive ($g_s < 0$ and $0 < |g_s| \ll |g_c|$)

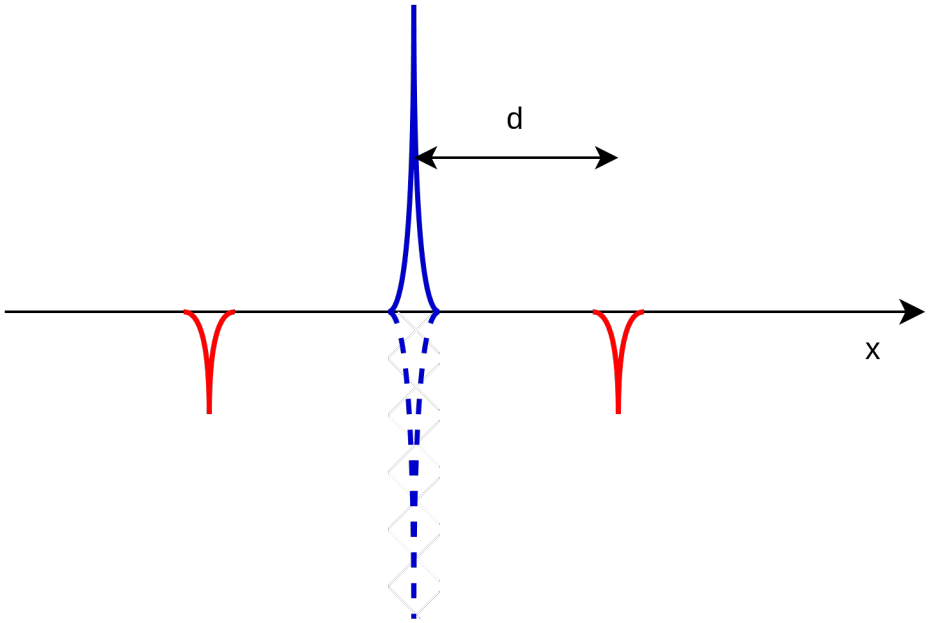

Figure 4.1: Schematic presentation of a symmetric three-delta potential, where distances between potential peaks equal d. This study focuses on configurations where the side potential coefficients are negative (attractive potentials, red lines), while the central potential coefficient is varied across both strongly attractive and repulsive regimes (blue dashed and solid lines, respectively).

The functions fulfilling the Schrödinger equation $\hat{H}\Psi(x) = E\Psi(x)$ can be obtained using an approach analogous to that employed for the single delta potential case in Sec. 3.1. As before, we primarily focus on symmetric states satisfying $\Psi(x) = \Psi(-x) = \Psi(|x|)$. In the regions between the delta potentials, the wavefunction must correspond to an eigenfunction of the free-particle Hamiltonian. Given that the potential is nonzero only at three discrete points, it is convenient to express the

wavefunction in the form of

$$\Psi(x) = \begin{cases} A_1 e^{\kappa|x|} + B_1 e^{-\kappa|x|}, \ |x| \leq d \\ A_2 e^{\kappa|x|} + B_2 e^{-\kappa|x|}, \ |x| > d \end{cases} \tag{4.2}$$

where the exponent is defined as $\kappa = \sqrt{-2E}$, and without loss of generality can be restricted to $\mathrm{Re}\{\kappa\} \geq 0$.

The effect of external delta potentials on the wavefunction can be incorporated through modified boundary conditions imposed on the wavefunction's derivatives $\Psi'(x) = \frac{\partial}{\partial x}\Psi(x)$ at the positions $x = 0$ and $x = d$. Together with the requirement of wavefunction continuity, this yields the following matching conditions

$$\begin{cases} \Psi(d^-) = \Psi(d^+) \\ \frac{\hbar^2}{2m}\Big(\Psi'(0^+) - \Psi'(0^-)\Big) = g_c \Psi(0) \\ \frac{\hbar^2}{2m}\Big(\Psi'(d^+) - \Psi'(d^-)\Big) = g_s \Psi(d). \end{cases} \tag{4.3}$$

By applying them to the general form of the function given in Eq. (4.2) one obtains following relations

$$\begin{cases} A_1 e^{2\kappa d} + B_1 = A_2 e^{2\kappa d} + B_2 \\ \frac{\hbar^2 \kappa}{m}\Big(A_1 - B_1\Big) = g_c\Big(A_1 + B_1\Big) \\ \frac{\hbar^2 \kappa}{2m}\Big((A_2 - A_1)e^{2\kappa d} - (B_2 - B_1)\Big) = g_s\Big(A_2 e^{2\kappa d} + B_2\Big) \end{cases} \tag{4.4}$$

which for $\kappa \neq 0$ and $\kappa \neq \tilde{g}_c$ can be then reduced to

$$\begin{cases} -\frac{\tilde{g}_s}{\kappa}\Big(e^{2\kappa d} - \frac{\tilde{g}_c - \kappa}{\tilde{g}_c + \kappa}\Big)A_1 - \frac{\tilde{g}_c - \kappa}{\tilde{g}_c + \kappa}A_1 = B_2 \\ -\frac{\tilde{g}_c - \kappa}{\tilde{g}_c + \kappa}A_1 = B_1 \\ \frac{\tilde{g}_s}{\kappa}\Big(1 - e^{-2\kappa d}\frac{\tilde{g}_c - \kappa}{\tilde{g}_c + \kappa}\Big)A_1 + A_1 = A_2. \end{cases} \tag{4.5}$$

where $\tilde{g} = \frac{mg}{\hbar^2}$. As can be seen from the equations, a natural length scale emerges — the distance between potential peaks. To simplify further analysis, I will henceforth adopt a system of units in which this characteristic unitary length is set to $d = 1$.

The same as in the case of a single delta potential, two types of eigenstates can be observed here. For positive energy values, where the exponent κ is imaginary, the probability of finding a particle does not decay to zero with distance from the center of the box. These correspond to unbound (scattering-like) states, which are not central to the subsequent analysis and will therefore not be discussed in detail.

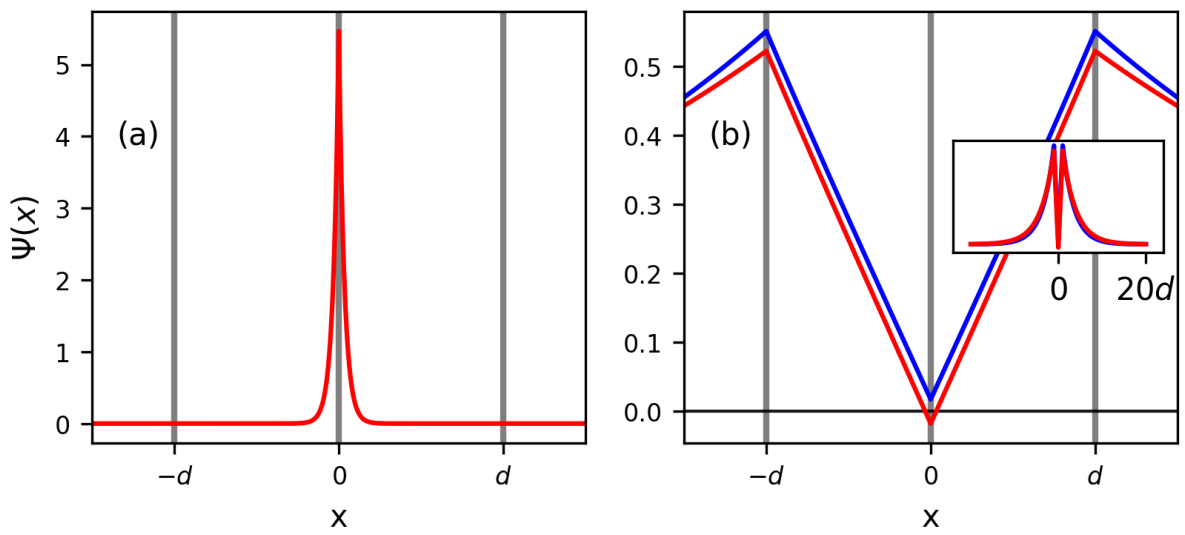

Figure 4.2: Three types of bound states that can appear in the systems with three delta potential, discussed in Sec. 1. Panel (a) illustrates a bound state of the first kind, corresponding to negative values of both potential coefficients $\tilde{g}_c d \ll \tilde{g}_s d < 0$. This state characterizes by a maximum probability density at the central potential and an exponential decay of the wavefunction with increasing distance from the origin. Panel (b) displays bound states of the second (blue line, $\tilde{g}_c d \gg 1$) and third (red line, $\tilde{g}_c d \ll 1$) kinds. In these cases, the probability of finding the atom at $x = 0$ is significantly lower than at positions corresponding to the side potentials. The wavefunction exhibits exponential decay for distances $|x| > d$. The third-kind bound state is distinguished by the presence of two nodes in the wavefunction. The data shown corresponds to potential parameters $\tilde{g}_c d = \pm 30$ and $\tilde{g}_s d = -0.7$. The vertical gray lines indicates positions of the potential peaks.

1 Bound states

The study presented in this chapter is devoted primarily to the bound states, where - as previously mentioned - the energy is negative, the parameter κ is a positive, real number, and, consequently, to avoid divergence in the wavefunction, the coefficient A_2 in Eq. (4.5) must be set to zero. Under these assumptions, the admissible values of κ are restricted to those that satisfy Eq. (4.6)

$$1 + e^{-2\kappa} \frac{\left(\kappa - \tilde{g}_c\right)}{\left(\kappa + \tilde{g}_c\right)} = -\frac{\kappa}{\tilde{g}_s}, \tag{4.6}$$

what for the domain $\kappa > 0$ can be simplified to

$$e^{2\kappa} = \frac{-\tilde{g}_s}{(\kappa + \tilde{g}_s)} \frac{\kappa - \tilde{g}_c}{\kappa + \tilde{g}_c}. \tag{4.7}$$

As it was mentioned earlier, we consider systems where $|\tilde{g}_c| < |\tilde{g}_s|$. Under these conditions three distinct types of bound states can be identified:

(i) The first of these occurs exclusively for $g_c < 0$, and resembles the bound state known from the single delta potential model. In that case, the probability density of finding the particle decays approximately exponentially with the distance from the central potential (see Fig. 4.2(a)). The energy associated with this state is highly negative, indicating a deeply bound configuration.

(ii) The second type of bound state, which arises when the central potential is repulsive ($g_c > 0$), differs substantially from the first one. As shown in Fig. 4.2(b), the wavefunction exhibits maxima at the locations of the side delta potentials. In this configuration, the probability density at the center ($x = 0$) decreases as the strength of the central repulsion increases, eventually approaching zero in the limit $\Psi(x = 0, \tilde{g}_c \to \infty) = 0$. The energy of this state remains negative, but is significantly higher (less negative) than that of the bound state of first kind. In that case, the decay parameter lies within the range $0 < \kappa < |\tilde{g}_s|$.

(iii) The third type of bound state is qualitatively similar to the second one. The key difference is that it arises for attractive central potentials ($g_c < 0$) and is characterized by the presence of two nodes in the wavefunction (see Fig. 4.2(b)). As in the second case, the probability density reaches maximum near the positions of the side delta potentials. The decay parameter κ again lies in the range $0 < \kappa < |g_s|$.

What is particularly important for further studies is that the bound states of the second and third kind are structurally nearly identical. The key difference lies in the values of the central potential coefficient required to support them: the second kind emerges for highly positive values of g_c, while the third kind appears only for highly negative g_c. This implies that a quench of the central potential — similar to that discussed in Chapter 3 — could induce a transition between these two bound states.

2 Critical potential coefficient values

Notably, bound states of the second and third kind exist only for specific values of the potential coefficients. To identify the parameter regions in which such states may emerge, it is instructive to examine Eq. (4.7) in more detail.

What can be found there is that the equation is satisfied for $\kappa = 0$. However, this value lies outside the admissible domain of the parameter κ. Furthermore, the exponential function on the left-hand side of the equation ($e^{2\kappa}$) is strictly positive and monotonically increasing with κ. The right-hand side part ($\frac{-\tilde{g}_s}{\kappa+\tilde{g}_s}\frac{\kappa-\tilde{g}_c}{\kappa+\tilde{g}_c}$) within the regime of interest, where $\kappa < |\tilde{g}_s|$, this expression is also positive and diverges to $-\infty$ as $\kappa \to -\tilde{g}_s$.

Under these conditions, one can demonstrate that bound states of the second and third kind can emerge only if the derivative of the right-hand side of Eq. (4.7) in the limit $\kappa \to 0$ is smaller than the derivative of the left-hand side

$$\frac{-\tilde{g}_c - 2\tilde{g}_s}{\tilde{g}_c\tilde{g}_s} < 2 \tag{4.8}$$

what is fulfilled for

$$\tilde{g}_s < \frac{1}{2 + \frac{2}{\tilde{g}_c}}. \tag{4.9}$$

Noteworthy, the critical value of the side potential coefficient, denoted as $\tilde{g}_{s,\mathrm{crit}}$, exhibits a slight asymmetry depending on the sign of the central potential coefficient. This subtle difference has surprising consequences, which are discussed in subsequent sections.

3 The missing bound state

The consequences of the differences in the critical values of $\tilde{g}_{s\mathrm{crit}}$ for opposite signs of $\tilde{g}_c$ are evident in the energy spectrum shown in Fig. 4.3(a). As can be observed, for large values of $|\tilde{g}_s|$, the energies of the two bound states converge. This convergence is accompanied by a similar trend in the structure of the wavefunctions, with the fidelity between these states approaching unity as the side potential strength increases (see Fig. 4.3(b)). However, an important point to note is that the bound state of the second kind appears for weaker side potentials compared to the third kind. This observation opens up intriguing possibilities for a theoretical thought experiment. Imagine that in the laboratory, a bound state of the second kind is prepared. In that configuration, the repulsive and attractive components of the

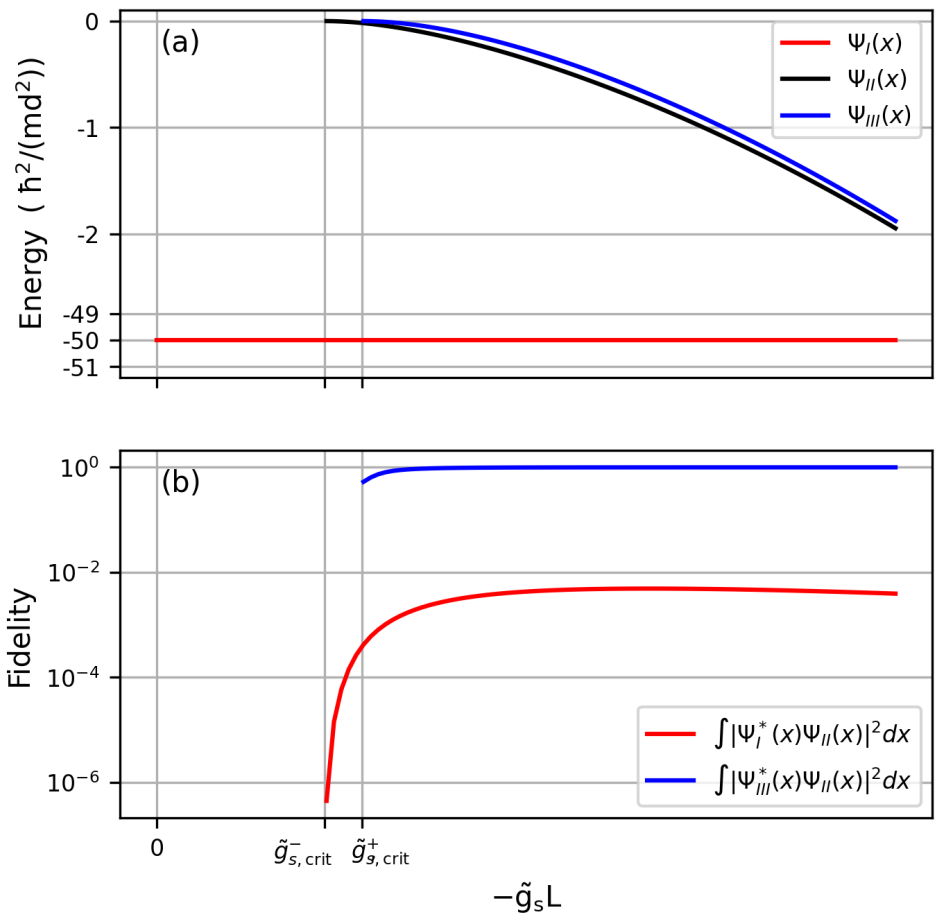

Figure 4.3: (a) Energies of the three types of bound states discussed in Sec. 1 as functions of the side potential coefficient $\tilde{g}s$. Three distinct regions can be identified. In the first region ($0 \leq \tilde{g}s < \tilde{g}s, \text{crit}^{+}$), only a single bound state of the first kind exists. In the intermediate region ($\tilde{g}^{+}_{s,\text{crit}} \leq \tilde{g}_s < \tilde{g}^{-}_{s,\text{crit}}$), both first- and second-kind bound states are supported. Finally, for stronger attraction ($\tilde{g}_s < \tilde{g}^{-}_{s,\text{crit}}$), all three types of bound states coexist. (b) Fidelity between the second-kind bound state and the remaining bound states. The overlap between the first- and second-kind bound states is negligible, whereas the fidelity between the second- and third-kind bound states remains high throughout the region where both are present.

potential balance each other, resulting in a bound state with a relatively large spatial width. Upon abrupt reversing the central potential, the post-quench state will become a superposition of the eigenstates of the new Hamiltonian where two possible outcomes can arise:

(i) if the side potential is sufficiently strong $\tilde{g}_s \leq \tilde{g}^+_{s,\mathrm{crit}}$, the superposition will contain significant contribution from the third type of bound state. In this case, the system will remain stable over long timescales following the quench.

(ii) conversely, if the side potential is too weak to support the third type of bound state, the superposition will primarily consist of non-bound states, and the atom will begin to evaporate. Notably, this eventual evaporation occurs despite the fact that all potentials are strongly attractive after the quench.

4.2 Super-evaporation in discrete systems

The analog of the aforementioned phenomenon, namely the delocalization of a single atom in a three-Dirac-delta potential, is expected to occur also in many-body systems, where two types of interactions come into play. However, to date, no research has been conducted for continuous-space systems. Fortunately, a comparable effect is expected to emerge in a system of atoms confined in a one-dimensional lattice, where the atoms possess a nonzero dipolar magnetic moment what allow them to interact non-locally.

In such a scenario, the appearance of a dominant sinusoidal periodic potential in the tight-binding regime forces the wavefunction to be expressed as a superposition of Wannier functions [83, 84, 85]. Consequently, it is convenient to employ second quantization (see Sec. 1) for describing the systems of interest, as will be done in the following sections.

1 Model and phase diagram

In the second-quantized notation the system of interest $-$ a model of N bosons confined in a one-dimensional lattice interacting via both on-site and nearest-neighbor interactions is well described by the extended Bose-Hubbard Hamiltonian

$$\hat{H} = -J\sum_{j=-N_h}^{N_h-1}\left(\hat{b}_j\hat{b}^\dagger_{j+1} + h.c.\right) + \frac{U}{2}\sum_{j=-N_h}^{N_h}\hat{n}_j(\hat{n}_j-1) + V\sum_{j=-N_h}^{N_h-1}\hat{n}_j\hat{n}_{j+1}, \tag{4.10}$$

where $\hat{b}_j$ ($\hat{b}^\dagger_j$) represents a bosonic annihilation (creation) operator at site j, $\hat{n}_j = \hat{b}^\dagger_j\hat{b}_j$, $N_h = \lfloor N_s/2 \rfloor$, N_s is a number of lattice sites, J is the tunneling coefficient between the neighboring lattice sites ($J > 0$), U characterizes the strength of on-site interactions and V stands for the strength of nearest-neighbor interactions.

It is worth emphasizing that the setup considered here is nonstandard: the number of particles N is fixed and significantly smaller than the number of lattice sites N_s. As a result, the phase diagram of this system does not contain the famous Mott insulator (with exactly one atom in each lattice site [84]).

Throughout our work, we assume the nearest-neighbor forces to be weak and attractive. Regarding on-site forces, we are interested in two limiting cases - either strong local repulsion or strong local attraction. We first analyze the static properties in both cases to understand later the dynamics of the system after a quench in the on-site interaction strength. Note that after such a quench the two interactions — the on-site and nearest-neighbor ones, are attractive.

To explicitly indicate the sign of U in the Hamiltonian Eq. (4.10) — corresponding to either strong on-site repulsion ($U \gg J$) or strong on-site attraction ($U \ll -J$) — we introduce the notations H^+ and H^-, respectively. Specifically, the Hamiltonians H^+ and H^- share identical values of the tunneling and nearest-neighbor interaction parameters, J and V, while their on-site interaction parameters, U, differ only in sign.

The extended Bose-Hubbard model in the regime of strong local interactions exhibits a rich and non-trivial ground-state phase diagram. Even in the absence of nearest-neighbor interactions ($V = 0$), the ground state can realize one of three distinct phases: (i) a bright soliton for attractive on-site interactions ($U < 0$), (ii) a superfluid phase in the regime of weak repulsion ($J \gg U > 0$), or (iii) a lattice analog of the Tonks-Girardeau gas for strong repulsion ($U \gg J > 0$) [86].

As shown in [87, 88, 89], the inclusion of nearest-neighbor interactions in the extended Bose-Hubbard model with strong local interactions leads to the emergence of novel phases, called the self-bound liquid and the self-bound Mott insulator (bMI). In both phases, the ground-state energy per particle is lower than that of an ideal gas, and the corresponding density profiles are localized in position space, justifying the term *self-bound*. Furthermore, in both cases, the density profile exhibits a flat-top structure (see Fig. 4.4(b,c)) , reminiscent of quantum droplets studied extensively in the one-dimensional Bose gas [90, 91]. In the bMI phase, in contrast to the liquid phase, each lattice site is either empty or singly occupied, with negligible particle-number fluctuations, similar to the conventional Mott insulator.

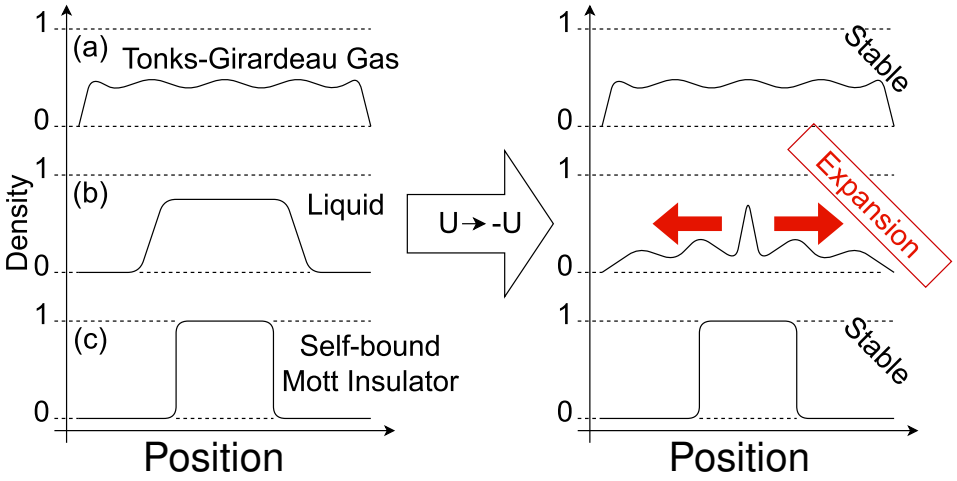

Figure 4.4: Schematic illustration of the three possible phases in the extended Bose–Hubbard model under strong on-site repulsion and their expected post-quench dynamics.

In this study, we focus on the regime of strong on-site interactions ($|U| \gg J, |V|$) and consider sudden quenches from H^+ to H^-, corresponding to a change of the interaction sign. For $V = 0$, the situation is straightforward: there exists only a single phase — a lattice equivalent of the Tonks-Girardeau state — and the interaction quench results in standard dynamics familiar from continuous models discussed in previous sections (see Chapter 3). In this case, the system exhibits minimal evolution and rapidly reaches a metastable sTG state.

However, when $V \neq 0$ and if the system is initially prepared close to either the TG or bMI state, the density profile remains stable following the quench. By contrast, a system initially prepared in the liquid phase displays a counter-intuitive behavior, similar to the one observed for a single atom in three-delta potential: despite the attractive character of all interactions, the liquid begins to evaporate rather than collapsing, as might be expected naively. To investigate and understand these phenomena, we first present analytical results for a two-particle system. Building on this foundation, we progressively extend that analysis to systems with larger particle numbers.

2 Two particles

For two bosons, one can find the eigenstates and eigenenergies of the eBH Hamiltonian analytically [92, 93], which can be used to understand the rudiments

of possible outcomes of the sTG quench. Here, we use the position representation

$$|\Psi\rangle = \sum_{j,j'=-\infty}^{\infty} \Psi(j,j') \, |j,j'\rangle \, , \tag{4.11}$$

where the summation extends over all lattice sites. We consider an infinite lattice, which allows the decoupling of the center-of-mass motion, defined as $R = (j+j')d/2$, and the relative coordinate $r = (j - j')d$, where d denotes the lattice spacing. As a result, each eigenstate can be written as a product state of the form $\Psi(j,j') = e^{iKR}\psi_K(r)$, with K representing the center-of-mass momentum. Substituting this Ansatz into the Schrödinger equation, $\hat{H}\,|\Psi\rangle = E_K\,|\Psi\rangle$, yields the following equation

$$-J_K\left[\psi_K(r-d) + \psi_K(r+d)\right] + \left[U\delta_{r,0} + V(\delta_{r,d} + \delta_{r,-d}) - E_K\right]\psi_K(r) = 0, \tag{4.12}$$

where $J_K = 2J\cos(Kd/2)$ and E_K denotes the energy of the state. The difference equation Eq. (4.12) can be solved analytically, yielding explicit expressions for both scattering and self-bound states [93].

When analyzing the ground state of the system, it is sufficient to consider the case where the center-of-mass momentum is zero. The $K = 0$ spectrum is schematically illustrated in Fig. 4.5 for both strong repulsive (a) and attractive (b) on-site interactions. In this figure, the shaded regions represent the continuum energy of scattering states, while the solid and dashed lines correspond to self-bound states. To explore the parameter space of the model, we fix the on-site interaction strength U and vary the nearest-neighbor attraction V. It can be observed that both the number of self-bound solutions and the nature of the ground state depend on the value of V. In general, there exist at most two bound states. Moreover, there exists a critical value of the nearest-neighbor attraction

$$V_c = -\frac{2JU}{U+4J}, \tag{4.13}$$

for which the energy of the second bound state drops below the continuum spectrum of scattering states. At this point, we note that the corresponding value of the nearest-neighbor attraction, denoted by V_c, will play a crucial role in our subsequent analysis. In analogy to the notation $H^{\pm}$, we introduce $V_c^{\pm}$ to distinguish between the two critical cases. In the following subsection, we investigate the implications of these observations for the outcome of the sTG quench. Since the ground state for $U \gg J$ — which serves as the initial state for the sTG quench — can be either a scattering state or a bound state, we divide our analysis into two parts, revealing clearly visible differences between them.

Super-Tonks-Girardeau quench from a scattering state

For strong on-site repulsion and sufficiently weak nearest-neighbor attraction (specifically, $0 \leq |V| < |V_c^+|$), the ground state corresponds to a scattering state (region I in Fig. 4.5(a)). To understand the system's behavior under a $U \to -U$ super-Tonks–Girardeau quench, below we examine the properties of the scattering wave functions. The two-body scattering states have the following form

$$\psi_{K,k}(r \neq 0) = \cos\left(k|r| + \delta_{K,k}\right) \tag{4.14a}$$

$$\psi_{K,k}(0) = \cos\delta_{K,k}^{(0)} \frac{\cos(kd + \delta_{K,k})}{\cos\left(kd + \delta_{K,k}^{(0)}\right)} \tag{4.14b}$$

where the phase shifts are given by

$$\tan\delta_{K,k} = \frac{J_K + V\cos(kd) + \frac{2J_K V}{U}\cos^2(kd)}{V\sin(kd) - \frac{2J_K^2 - 2J_K V\cos(kd)}{U}\sin(kd)}, \tag{4.15}$$

and where

$$\tan\delta_{K,k}^{(0)} = -\frac{U}{2J_K\sin(kd)}. \tag{4.16}$$

The quasi-momenta k are continuous and belong to the interval $[0, \pi/d]$. The energies of the scattering states equals $E_{K,k} = -2J_K\cos(kd)$. The solution Eq. (4.14) remains valid for arbitrary values of the interaction parameters U, V, and the tunneling amplitude J. In the regime of primary interest, characterized by strong on-site interactions ($|U| \gg J, |V|$), the phase shift $\delta_{K,k}$ becomes independent of U. Specifically, in the limit $U \to \pm\infty$, the phase shift approaches

$$\lim_{U\to\pm\infty}\tan\delta_{K,k} = \frac{J_K + V\cos(kd)}{V\sin(kd)}, \tag{4.17}$$

while the contribution from the on-site interaction satisfies

$$\lim_{U\to\pm\infty}\delta_{K,k}^{(0)} = \mp\frac{\pi}{2}. \tag{4.18}$$

As a result, the scattering states for infinitely strong repulsive and attractive on-site interactions become identical. This implies, in particular, that the ground state of the system in the limit $U \to +\infty$ coincides with a highly excited eigenstate of the system for $U \to -\infty$. Consequently, after a quench from $U = +\infty$ to $U = -\infty$, the state of the system is unchanged.

An expansion in the small parameter $J/|U|$ indicates that the qualitative features of the infinite-interaction limit persist for large but finite on-site interactions. In this regime, the phase shifts acquire corrections of order $1/|U|$. Specifically, the phase shift becomes

$$\delta_{K,k}^{(0)} \approx \mp\frac{\pi}{2} \pm \frac{2J_K \sin(kd)}{|U|}, \tag{4.19}$$

and the total phase shift takes the form

$$\tan\delta_{K,k} \approx \frac{J_K + V\cos(kd)}{V\sin(kd)} \pm \frac{2J_K^3}{V^2|U|}, \tag{4.20}$$

where the upper (lower) sign corresponds to positive (negative) values of U. These expressions demonstrate that, although small on-site-interaction-dependent corrections appear, the overall structure of the scattering states remains approximately conserved under the transformation $U \to -U$ when $|U| \gg J, |V|$.

The observed similarity between the ground state of the repulsive Hamiltonian H^+, denoted $\left|H_0^+\right\rangle$ and corresponding to the scattering state with $k = 0$, and a particular excited state of the attractive Hamiltonian H^-, is a manifestation of the aforementioned super-Tonks-Girardeau effect. The post-quench stability arises from the existence of an excited eigenstate of H^-, which closely resembles $\left|H_0^+\right\rangle$; this state will hereafter be referred to as the *superpartner*. Following a sudden quench from strong repulsive to strong attractive interactions, the initial state $\left|H_0^+\right\rangle$ becomes an eigenstate of the new Hamiltonian H^-, resulting in trivial time evolution characterized by a global phase accumulation only.

The scattering state properties discussed above are consistent with general expectations for systems governed by purely local interactions [94]. However, the model considered here is more intricate due to the presence of additional nearest-neighbor terms. This raises a more compelling question: does a similar phenomenon persist in regimes where the nearest-neighbor attraction is sufficiently strong for the ground state to become self-bound? In such cases, the system transitions from a delocalized scattering regime to one characterized by bound states, potentially altering the post-quench dynamics in a nontrivial way.

Super-Tonks-Girardeau quench from self-bound state

All two-body self-bound eigenstates of the eBH Hamiltonian with nearest-neighbor interactions Eq. (4.10) take the form of exponentially localized wave functions [92]

$$\begin{cases} \psi_K(0) = \mathcal{N}\frac{4\alpha_K}{U\alpha_K+2(\alpha_K^2+1)} \\ \psi_K(r_i \neq 0) = \mathcal{N}\alpha_K^{|i|-1} \end{cases} \tag{4.21}$$

where $\mathcal{N}$ denotes the normalization constant of the bound-state wave function and corresponding energies are given as

$$E_K = -J_K\frac{1+\alpha_K^2}{\alpha_K}. \tag{4.22}$$

The base of the exponential (α_K) depends on the system parameters and can be determined by substituting the Ansatz from Eq. (4.11) into the Schrödinger equation. This procedure yields the following condition for α_K

$$J_K V\alpha_K^3 + (UV - J_K^2)\alpha_K^2 + J_K(U+V)\alpha_K + J_K^2 = 0. \tag{4.23}$$

The resulting eigenenergies of the self-bound states are shown as lines in Fig. 4.5(a,b). The corresponding coefficients α_K that satisfy the equation (with the additional condition $|\alpha_K| < 1$, ensuring the decay of the wave function) are depicted in Fig. 4.5(d). For simplicity, we focus on the case $K = 0$ and, for brevity, omit the index K, i.e. $\alpha \equiv \alpha_{K=0}$ in the subsequent discussion.

Upon examining Fig. 4.5(d), it becomes evident that the values of the coefficients α form two distinct pairs of branches. The lower pair — corresponding to a strongly localized state with energy $E \approx U$ — is present throughout the entire range of V, while the upper pair emerges for $|V| \geq |V_c|$. That upper branch is of particular interest for our studies: for repulsive on-site interactions ($U > 0$), it corresponds to the ground state of the system (see Fig. 4.5(a)), whereas for attractive interactions ($U < 0$), it corresponds to a certain excited state with a similar wave function, as shown in Fig. 4.5(c_{III}). Crucially, the appearance of the upper pair is dependent on U, as

$$V_c^{\pm} \overset{|U|\gg 1}{\approx} -2J \pm \frac{8J^2}{|U|} \tag{4.24}$$

and for Hamiltonians characterized by large and finite $|U|$ differs slightly for $U < 0$ and $U > 0$, fulfilling the relation $V_c^- < V_c^\infty < V_c^+$, where $V_c^\infty = -2J$. This distinction implies that for $V_c^- < V < V_c^+$ (region II in Fig. 4.5), the ground state of H^+ does not have a superpartner among the eigenstates of H^-. A superpartner appears in region III, and its energy gradually approaches the branch of H^+ states.

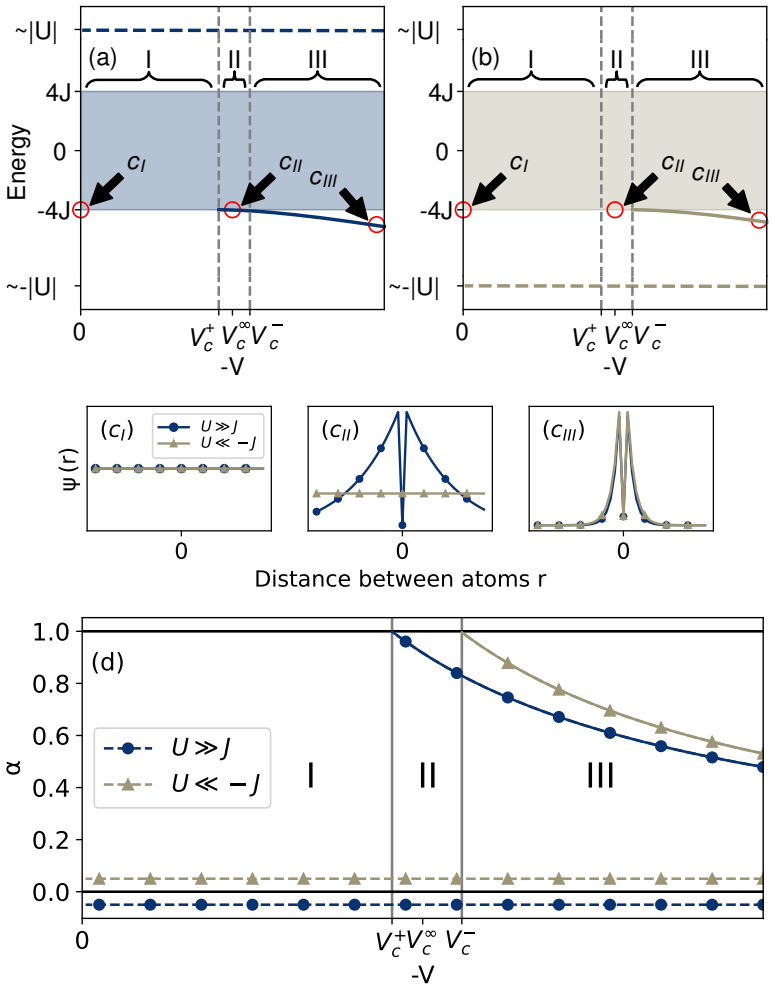

Figure 4.5: The upper panels show the $K = 0$ energy spectrum of the eBH model for two atoms in an infinite lattice as a function of the nearest-neighbor interaction strength V for (a) $U \gg J$ and (b) $U \ll -J$. The energies correspond either to the continuum spectrum of the scattering states (the shaded bands) or to self-bound states (solid and dashed lines). There are three relevant regions of the coupling V: in (I), the ground state of H^+ is a scattering state, in contrast to (II) and (III), where the ground state of H^+ is the self-bound state. The difference between (II) and (III) is that in the latter, there exists an excited, self-bound eigenstate of H^- with energy close to the energy of a ground state of H^+. The panels in the middle show three pairs of eigenstates for three different values of nonlocal attraction V corresponding to aforementioned regions (marked in the upper panels by c_I, c_{II} and c_{III}). We show the ground states of the Hamiltonians H^+ (blue lines with circles) and the eigenstates of H^- (yellow lines with triangles) with the energy closest to the energy of H^+ GS. The bottom panel (d) shows the coefficients α characterizing the two-body self-bound eigenstates. In region II there is no self-bound eigenstate of H^- (solid yellow lines with triangles) with α similar to that of H^+.

From this simple analysis, we can identify three distinct ranges of the nearest-neighbor interaction parameter V, each associated with different dynamics following a super-Tonks-Girardeau quench. In regions I and III, where the ground state $\left|H_0^+\right\rangle$ has a superpartner, the system will remain stable after the quench. In contrast, we do not expect the same stability when the system is initialized in the ground state from region II. Since there is no self-bound state that would be similar to the initial one (the deeply self-bound state differs significantly) quench there leads to the expansion of atoms that were previously bound together. The sTG quench diagram is presented in Fig. 4.6. The existence of three regions in

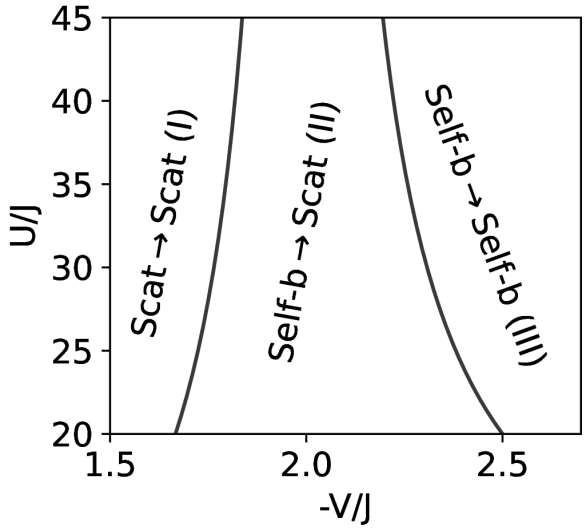

Figure 4.6: Super-Tonks-Girardeau quench diagram for the two-body system. In region I, the ground state of the system is a scattering state (Scat), which is stable in sTG quench. Region II corresponds to self-bound states (Self-b), which expand after the quench to strong attraction. Finally, in region III the self-bound ground state survives the change of interactions and is stable after the quench.

the sTG quench diagram can be intuitively understood as follows. It is well known that the sTG state exhibits stronger correlations than the Tonks-Girardeau system. Specifically, the sTG state is characterized by a higher pressure compared to the TG gas for the same density. In region II, the initial state for the quench, $|H_0^+\rangle$, is *weakly bound* — its energy is slightly below that of the non-interacting system, $E_{free} = -4J$, and the nearest-neighbor attraction just barely compensates the local repulsion. When the system is quenched to stronger sTG correlations, the contribution to the *pressure* from on-site interactions is effectively increased. In region II, where the nearest-neighbor attraction is weak, this increase results in the destruction of the initial bound state. However, as the attraction strength is

increased, it becomes more difficult to disrupt the bound state, and it survives the quench — this occurs in region III. We believe that this intuition, based on the increase in pressure induced by the quench, also applies to larger systems, as we will explore in the following sections.

3 Few-body systems

The effect described above is scalable and is expected to occur also in setups consisting of more atoms. This section is devoted to presenting the effect of *super-evaporation* in few-body systems. Systems consisting of more than two

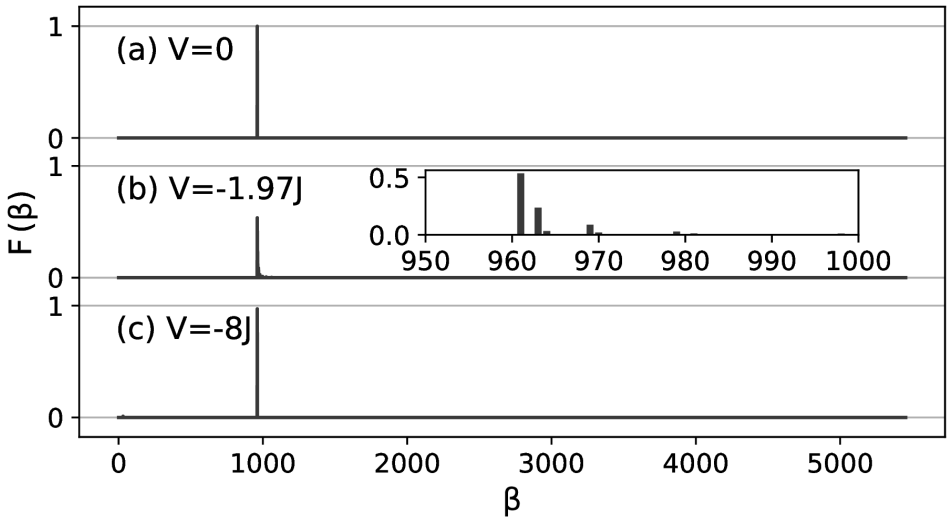

Figure 4.7: Fidelity $F(\beta)$ between the ground state of H^+ and eigenstates of H^- for $N = 3$ atoms in lattice with $N_s = 31$ sites, with $|U| = 40J$. For $V = 0$ (scattering state) and $V = -8J$ (deeply self-bound state), there is a highly excited eigenstate, the superpartner, practically equal to $|H_0^+\rangle$. In contrast, the ground state of H^+ with an intermediate value of $V = -1.97J$ (weakly self-bound) is a superposition of several states with different energies, which makes it unstable after the quench.

atoms are significantly more complex to analyze — wavefunctions cannot be obtained analytically, necessitating the use of numerical methods. However, as far as number of atoms is low, it is feasible to numerically diagonalize the Hamiltonian given in Eq. (4.10). We use this technique here, to find the ground state of the Hamiltonian H^+ and then search for eventual superpartners among the eigenvectors of H^-. To do so, we compute the fidelity between the ground state of $|H^+\rangle$ and the eigenstates of H^-

$$F(\beta) = |\langle H_0^+ | H_\beta^- \rangle|^2, \tag{4.25}$$

where $|H^-_\beta\rangle$ denotes the β-th eigenstate of H^-.

The outcomes of that procedure for few distinct cases are presented in Fig. 4.7. What can be seen there is that for fixed ratio $|U|/J = 40$ depending on the nonlocal attraction coefficient V three outcomes can be obtain:

(i) for $V = 0$, the ground state of H^+ is a scattering state. This state has a clearly visible superpartner among the eigenstates of H^-, as shown in Fig. 4.7(a). The fidelity plot for this case reveals a distinct peak approaching unity, indicating a strong correspondence between the two states;

(ii) for $V = -1.97J$, the ground state of H^+ is a self-bound state that does not possess a superpartner. As shown in Fig. 4.7(b), this state is a superposition of many eigenstates of H^-, with the highest fidelity reaching only about $\max F(\beta) \approx 0.5$;

(iii) finally, for $V = -8J$ the GS is the self-bound state, but it posses a superpartner, as can be seen in Fig. 4.7(c).

A broader perspective on these results is provided in Fig. 4.8, which shows the maximal fidelities between the ground states of H^+ and the eigenstates of H^-. Three distinct regimes can be identified: Regime I, where the ground state is a scattering state and possesses a superpartner; Regime II, where the ground state is self-bound and lacks a superpartner; and Regime III, where the self-bound ground state has a superpartner. This structure closely resembles the case of two atoms, where a similar division into three regions was observed.

Evaporation in *ab initio* dynamics

The predictions based on the spectral analysis can be verified by studying the full dynamical problem. Specifically, we prepare the ground states of the systems discussed in the previous section, then quench the on-site interactions and track the resulting dynamics of the density profiles and second-order correlation functions defined as $G_2(j, j') = \frac{1}{N^2}\langle \hat{b}^\dagger_j \hat{b}^\dagger_{j'} \hat{b}_{j'} \hat{b}_j \rangle$.

The results of such a time evolutions are presented in Fig. 4.9. As expected, the systems corresponding to states from regions I and III remain stable after the quench. This is not the case for the system with parameters from region II, where we observe a clear expansion, both in the density profile and in the two-body correlation function.

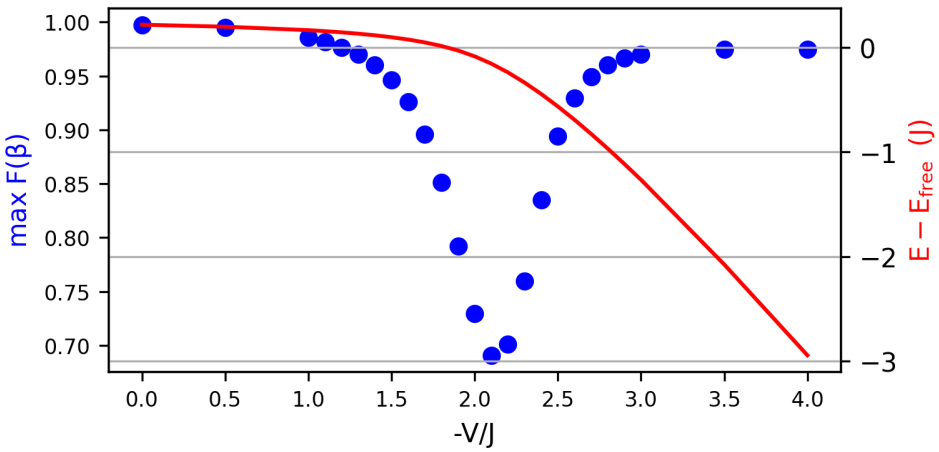

Figure 4.8: Energy (red line) and maximal overlap between the ground state of H^+ and the eigenstates of H^- (blue dots). For weak nonlocal attraction V, a superpartner — an eigenstate of H^- with high fidelity to the ground state of H^+ — exists. As the system approaches the point where the ground state of H^+ becomes self-bound (indicated by negative energy), the fidelity drops significantly, signaling the absence of a superpartner. For stronger nonlocal attraction, the fidelity rises again, which indicates the reappearance of a superpartner. The data were obtained numerically for $M = 21$, $N = 3$, and $|U| = 40J$.

Remarkably, this phenomenon — the delocalization of the state despite a drastic increase in the attractive interaction between atoms — persists also in larger systems. In Fig. 4.10 we present time evolution of second-order correlation functions for $N = 4, 6,$ and 8 bosons with parameters from region II. As one can see, observables presented there exhibit qualitatively the same behavior as these obtained for the $N = 3$ case — the quenched system appears to undergo super-evaporation.

It is worth noting that for systems with $N > 3$, we use DMRG [66] to determine the corresponding ground states, and then employ TDVP to study the post-quench dynamics (see Sec. 2.2). Although these methods are unquestionably powerful, they did not allow us to perform calculations for larger particle numbers. In the case analyzed here, the post-quench state is a superposition of many highly excited eigenstates, leading to a rapid growth of entanglement entropy during the evolution. This, in turn, results in a rapid growth of the Hilbert space required to continue the simulation, limiting us to very limited system sizes. However, the results presented here confirm that the phenomenon of super-evaporation should

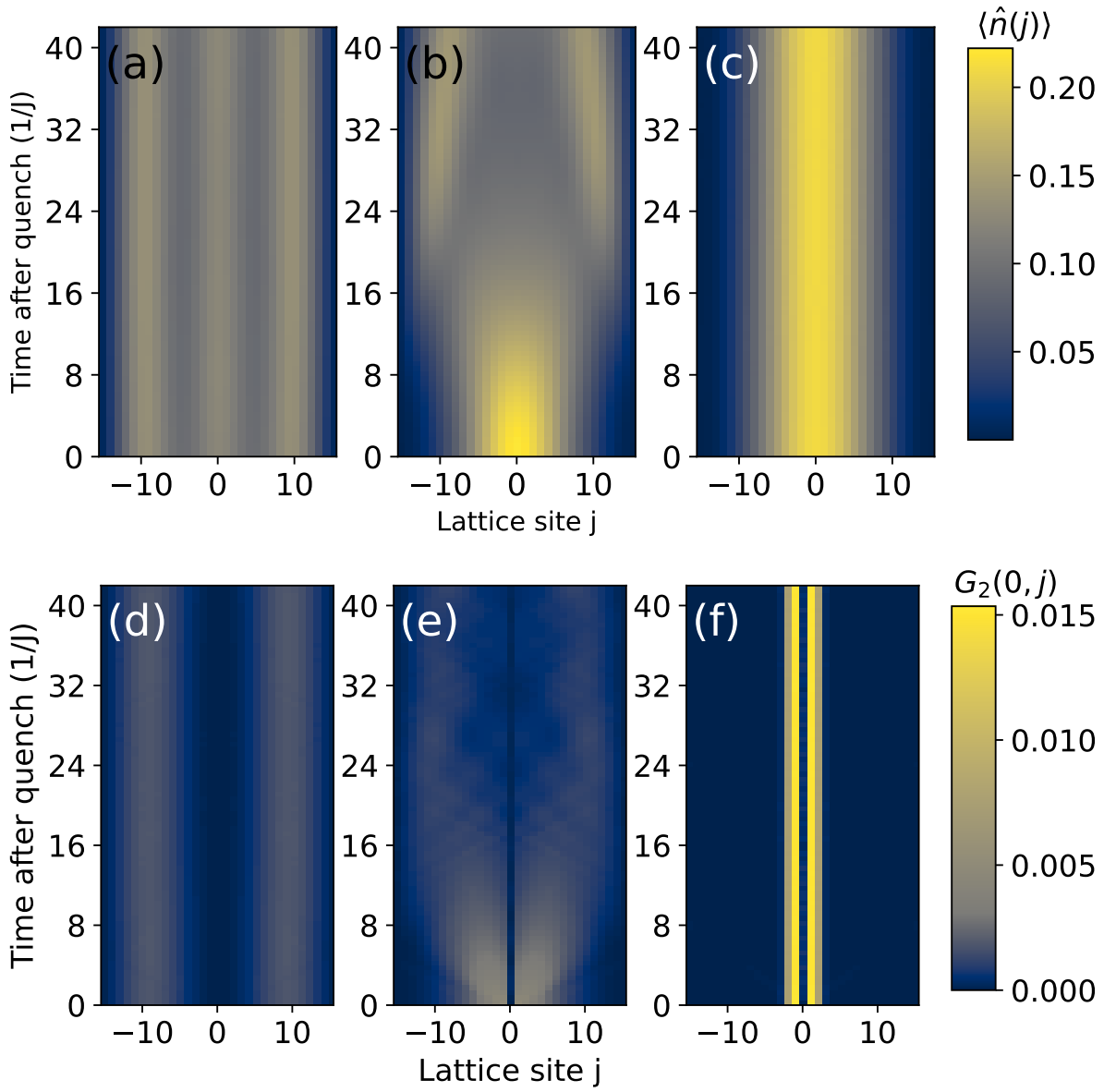

Figure 4.9: Density profiles (top panels) and density-density correlations (bottom panels) as a function of time for the quenched system initiated in the ground state of H^+. The nearest-neighbor interaction strengths are (a,d) $V = 0$, (b,e) $V = -1.97J$, and (c,f) $V = -8J$. It can be seen that for the weak (a, d) and very strong (c, f) attraction, both the density profile and the correlations remain unchanged for a long time. At the same timescale, the weakly bound state corresponding to $V = -1.97J$ fully evaporates (b, e). All figures correspond to the number of atoms $N = 3$ and $|U| = 40J$.

occur in few-body systems and suggest that similar processes may also arise in larger systems.

4 Perturbative analysis for macroscopic systems

In this section, we aim to describe super-TG quench in macroscopic systems, for which the numerical methods applied to few-body systems become impractical. In such cases, we lack access to both the many-body energy spectrum and the exact quench dynamics. Nevertheless, we gain insight through an approximate, perturbative description of the system, developed in a closely related context in [87]:

Since we consider a system of strongly repulsive bosons ($U \gg J$), the system governed by Hamiltonian Eq. (4.10) can be effectively mapped onto a fermionic one

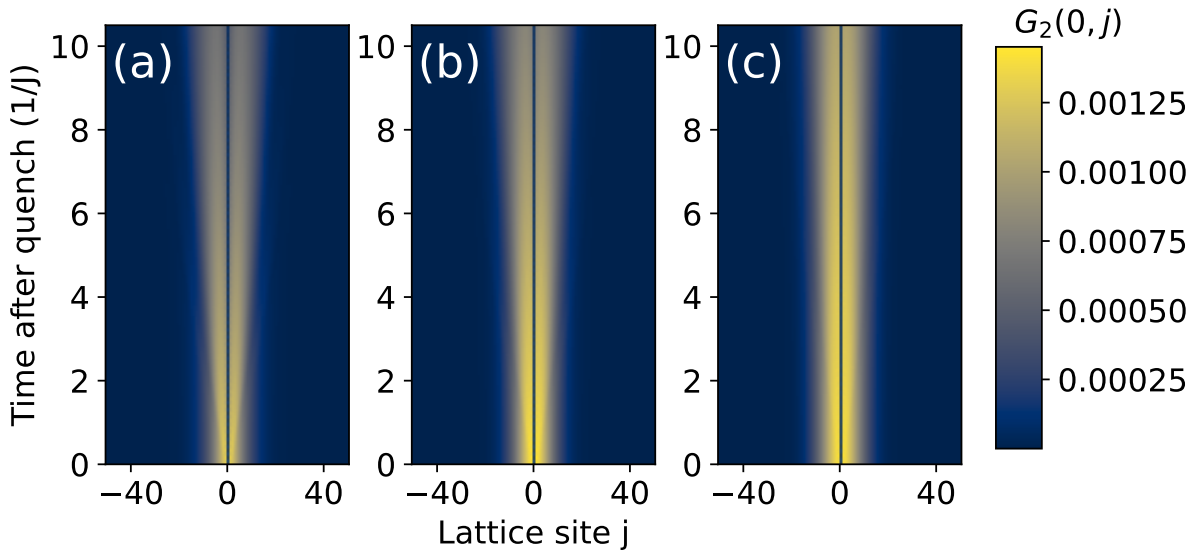

Figure 4.10: Second order correlations of a weakly self-bound ground states of H^+ in a systems consist of (a) $N = 4$, (b) $N = 6$ and (c) $N = 8$ atoms. As for the weakly self-bounded ground state of the three-atomic system, also here we can see a rapid increase in the distance between the atoms after quenching. This observation may be interpreted as a gradual evaporation of the self-bound state. Here $|U| = 40J$ and $V = -1.97J$. The data in this figure were obtained by using DMRG and TDVP methods [66, 95].

with an effective Hamiltonian $\hat{H}_{\text{eff}}$ [96]

$$\begin{aligned}\hat{H}_{\text{eff}} = &-J\sum_{j=-N_h}^{N_h-1}\left(\hat{c}_j^\dagger\hat{c}_{j+1}+h.c.\right)-\frac{4J^2}{U}\sum_{j=-N_h}^{N_h-1}\hat{n}_j\hat{n}_{j+1}\\ &+\frac{2J^2}{U}\sum_{j=-N_h+1}^{N_h-1}\left(\hat{c}_{j-1}^\dagger\hat{n}_j\hat{c}_{j+1}+h.c.\right)+V\sum_{j=-N_h}^{N_h-1}\hat{n}_j\hat{n}_{j+1},\end{aligned} \tag{4.26}$$

where $\hat{c}_j(\hat{c}_j^\dagger)$ represents a fermionic annihilation (creation) operator acting on site j ($\{\hat{c}_j,\hat{c}_{j'}^\dagger\}=\delta_{j,j'}$).

The energy of such system can be obtained perturbatively, using the ground state of non-interacting lattice fermions as the unperturbed reference state. In the thermodynamic limit, the ground-state energy can be estimated by evaluating the expectation value of the effective Hamiltonian Eq. (4.26) with respect to the Fermi gas ground state. This yields the following energy functional

$$E(n)/N=-2J\frac{\sin(\pi n)}{\pi n}-\frac{4J^2n}{U}\left(1-\frac{\sin(2\pi n)}{2\pi n}\right)+Vn\left(1-\frac{\sin^2(\pi n)}{\pi^2n^2}\right), \tag{4.27}$$

where n denotes the global density defined as average number of atoms in the lattice sites. In considered model, this density is bounded above by one particle per lattice site, reflecting an effective Pauli exclusion principle due to strong on-site repulsion.

A closer look at Eq. (4.27) reveals that for $|U|\gg|V|$, three distinct phases emerge: (i) a gaseous phase, (ii) a liquid, and (iii) a self-bound Mott insulator. Following Ref. [87], these phases can be identified by analyzing the energy functional Eq. (4.27) with respect to the density n (see Fig. 4.11). If the global minimum of the energy occurs at vanishing density, the system resides in the gaseous phase — physically, it is energetically favorable for the bosons to delocalize and spread over the entire lattice. A qualitatively different situation arises when the optimal density that minimizes the energy, n_{opt}, approaches unit filling, i.e., $n_{\text{opt}}=1$; in this case, the system is in the self-bound Mott insulator phase.

The third, intermediate phase — the liquid — appears within a relatively narrow range of nearest-neighbor coupling values V, for which $0<n_{\text{opt}}<1$ [1]. The boundary separating the liquid and bMI phases can be obtained analytically from Eq. (4.27) and corresponds to the critical coupling strength between adjacent lattice sites $V_{\text{bMI}}=-2J$. The full phase diagram can be found in Fig. 4.12(a).

[1] Notably, the emergence of liquid phase is a consequence of so-called *superexchange* processes, which yield the J/U correction to the energy [87]. In the absence of this term — i.e., without this effective additional attraction — the functional Eq. (4.27) does not support a stable liquid phase.

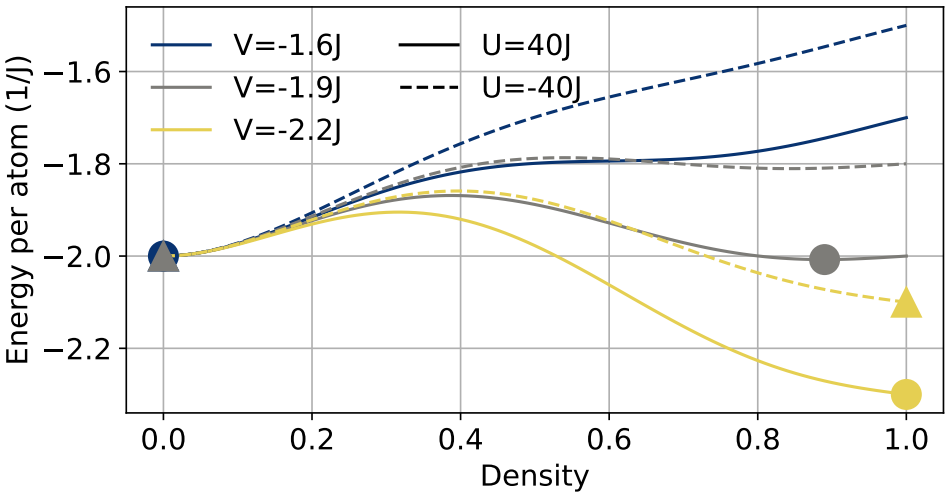

Figure 4.11: The energy of the dipolar bosons in a one-dimensional lattice for distinct values of the nearest-neighbor interactions V with a fixed on-site interaction $U = 40J$ (solid lines) or $U = -40J$ (dashed lines). The equilibrium phase of a system is dependent on the optimal density, i.e., the density for which the energy reaches a minimum. If $n_{\text{opt}} = 0$ a system finds itself in the gas phase, if $0 < n_{\text{opt}} < 1$ a system is a liquid and for $n_{\text{opt}} = 1$, it matches the bMI. It is worth noting that for both $U = 40J$ and $-40J$ positions on energy minimum are the same for gas and deeply self-bound Mott insulator, but for liquid, it jumps to 0. What may be found is that this effect occurs every time the ground state of H^+ is liquid (vide Fig. 4.12).

Equation (4.27) offers a fundamental understanding of the system with $U > 0$ and attractive nearest-neighbor interactions ($V < 0$), providing a perturbative description of the many-body ground state of H^+. However, at this point we face the second issue: how can we extend the analysis to attractive systems in our search for superpartners? Without access to the full spectrum, it is unable to fully address these questions — the states after quench correspond to highly excited eigenstates.

A partial solution to this problem lies in the observation that a potential superpartner of the state we quench, must share a very similar structure. Additionally, we know that the energy functional Eq. (4.27) was derived under the assumption that the ground state structure in a system with strong repulsive U is similar to the fermionic state. This implies that if a superpartner exists, the same functional should provide a quantitatively accurate estimation of its energy as well.

While this method cannot capture all aspects of the system's dynamics in every case, it can be used as a tool to potentially exclude the possibility of the existence of a

superpartner. Specifically, if the phase before and after the quench (determined based on the optimal density n_{opt}) is the same, it is possible that a superpartner exists and that the system may remain stable after sTG quench. If the phases differ, this serves as a strong indication that no superpartner exists. An example of such an analysis is presented in Fig. 4.11, where we show the energies of hypothetical superpartners obtained using this approach.

One may observe there that the optimal densities for weak (gas) and strong (bMI) nearest-neighbor attraction are identical for both positive and negative coefficients U. In contrast, for the intermediate value of nearest-neighbor attraction, $V = -1.9J$, the optimal densities differ significantly. For $U > 0$, the optimal density equals $n_{\mathrm{opt}} \approx 0.9$, corresponding to a liquid phase, whereas for $U < 0$, we find $n_{\mathrm{opt}} = 0$, which indicates a gaseous phase. This observation suggests that if $|H_0^+\rangle$ exhibits gaseous or bMI-type characteristics, it may have a superpartner and therefore remain stable after the quench. In contrast, the liquid phase is expected to evaporate, what is consistent with predictions made for few-body systems.

To summarize this analysis, we present a phase diagram for the hypothetical superpartners in Fig. 4.12(b). It is clearly visible that the entire liquid phase (and part of the bMI phase) for $U \gg J$ is replaced by a gaseous phase for $-U$. In other words, we expect that systems with large, negative U do not exhibits liquid-like eigenstates – the liquid phase is expected to evaporate after sTG quench, contrary to the gaseous and main part of bMI phases, which are expected to be stable (see Fig. 4.12(c)). Notably, a strong resemblance to the two-body case is evident (see Fig.4.6). However, the many-body case exhibits four distinct dynamical regions instead of three. Two of these correspond to post-quench stability, while the remaining two are associated with the evaporation of localized structures.

This distinction arises from the emergence of an additional phase in the many-body phase diagram. While the two-body scenario requires only a classification into bound and scattering states, the many-body system supports a richer structure, allowing for classification into gas, liquid, and bMI phases. As the particle number N increases and we transition from the two-body diagram (see Fig.4.6) to the many-body case (see Fig.4.12(c)), the phase boundaries shift, and the central region splits into two domains — both corresponding to dynamical evaporation of initially localized states.

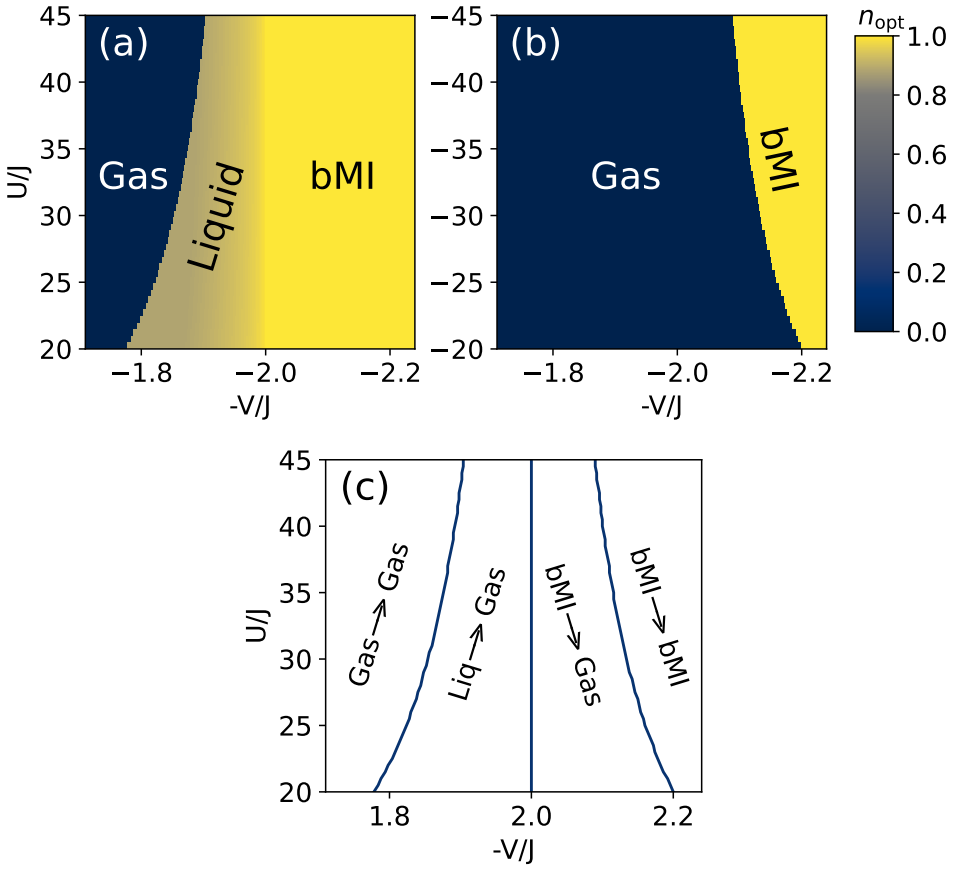

Figure 4.12: (a,b) The figures present the gas density at which the energy functional Eq. (4.27) reaches a minimum (n_{opt}). There are three possible states: gas ($n_{\mathrm{opt}} = 0$), liquid ($0 < n_{\mathrm{opt}} < 1$), and a self-bound Mott insulator ($n_{\mathrm{opt}} = 1$). Note that the liquid appears only for positive values of U (left picture). If the sign of on-site interactions is reversed (right image) the liquid and a part of the bMI are replaced by gas. This leads us to the conclusion that a sudden change of parameters from $U \gg J$ to $-U$ causes the evaporation of the liquid to the gaseous state. The parameters where phase transitions induced by sTG quench is expected are presented in panel (c).

5 Local density approximation for inhomogenous system

In this section, we continue the analysis of many-body systems based on the perturbatively obtained energy functional Eq. (4.27). This time, however, we adopt the local density approximation (LDA) to construct a dynamical theory. In this way, the results presented above — with appropriate modifications — can be extended to large but finite systems, where the density is no longer uniform. To account for the lack of translational invariance, we introduce a position-dependent density profile, symmetrize the nearest-neighbor interaction terms, and incorporate the

contribution from the density envelope into the total energy. These modifications led us to

$$E[\mathbf{c},\mathbf{c}^*]=-J\sum_{k=-N_h}^{N_h-1}\left(c_kc_{k+1}^*-2n_k+c_k^*c_{k+1}+2\frac{\sin(\pi n_k)}{\pi}\right)-\sum_{k=-N_h}^{N_h}\frac{4J^2n_k^2}{U}\left(1-\frac{\sin(2\pi n_k)}{2\pi n_k}\right)$$
$$+V\sum_{k=-N_h}^{N_h-1}n_kn_{k+1}\left(1-\frac{1}{2}\frac{\sin^2(\pi n_k)}{\pi^2n_k^2}-\frac{1}{2}\frac{\sin^2(\pi n_{k+1})}{\pi^2n_{k+1}^2}\right), \tag{4.28}$$

where c_k denotes the complex density amplitude at the k-th lattice site, with the local occupation given by $n_k = |c_k|^2$.

The energy functional can be used to construct the Lagrangian of the system. From this, employing the Euler-Lagrange formalism, one can derive the equations of motion for the complex amplitudes $c_j(t)$, which can then be used both to find the ground state (via imaginary time evolution) and to study the dynamical properties of the system

$$i\frac{\partial}{\partial t}c_j = \frac{\partial}{\partial c_j^*}E[\mathbf{c},\mathbf{c}^*]. \tag{4.29}$$

As the result, we find that the resulting density profiles agree well with the predictions derived from the analysis presented in the previous section (see Sec. 4). In particular, in regimes where a uniform system is expected to exhibit a liquid phase, the simulated finite system develops a droplet-like state characterized by a flat-top density profile (i.e., a region of nearly constant density in the bulk, see Fig. 4.13(c,d)). These density values closely match the predictions for a homogeneous gas.

Furthermore, the system's time evolution following a quench is consistent with previous expectations. As illustrated in Fig. 4.13, where we examine two droplets with different atom numbers, after a sudden change in interactions from strong repulsion ($U \gg J$) to attraction ($-U$), the droplets begin to evaporate gradually, displaying dynamics in line with the anticipated behavior.

4.3 Summary

In this chapter, I have presented one of the highly non-intuitive effects that can emerge after an sTG quench in systems featuring two competing types of interactions. As an initial example, I considered a single atom in an infinitely long,

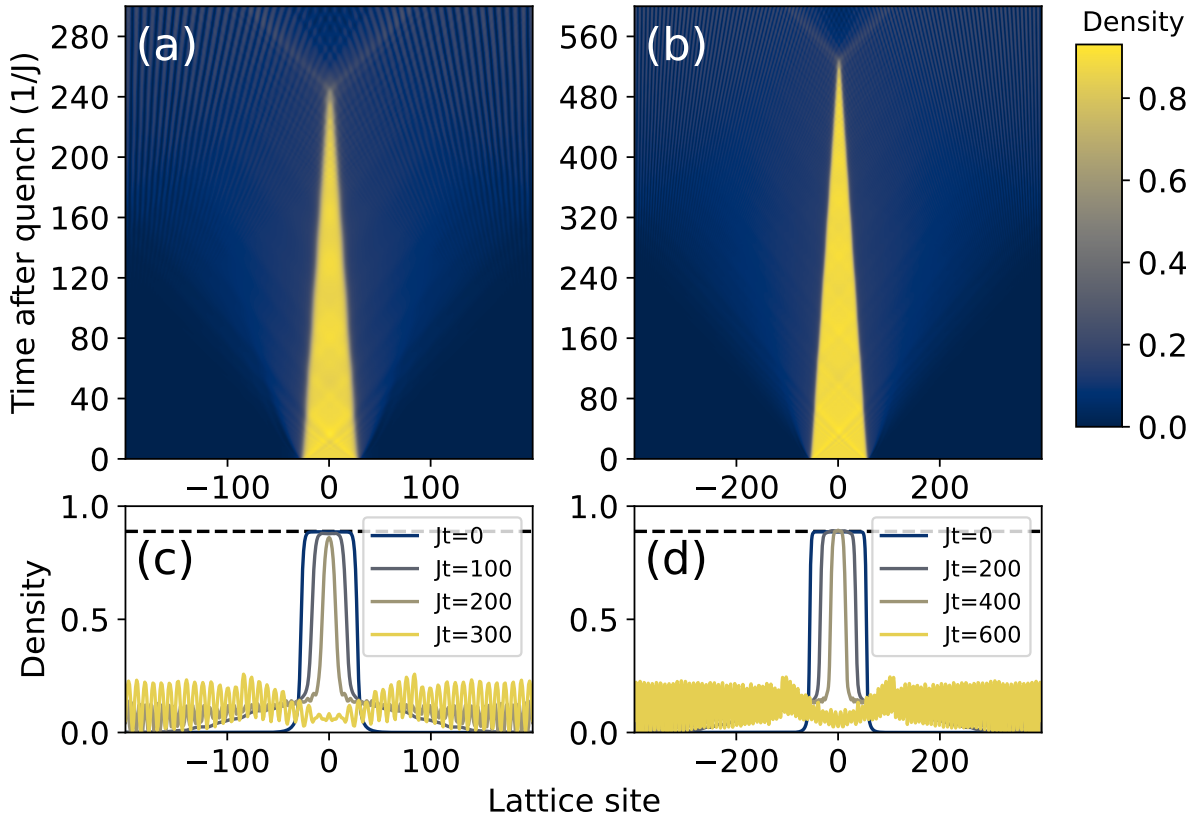

Figure 4.13: Dynamics of a droplet with (a, c) $N = 50$ and (b, d) $N = 100$ bosons after a sTG quench from $U = 40J$ to $U = -40J$ with $V = -1.9J$. As can be seen, after rapid change of interaction, droplets gradually evaporate and ends up in the gaseous phase. The time dependence of densities is described by Eq. Eq. (4.29). The dashed lines in lower panels indicates the optimal density n_{opt} of a uniform system corresponding to appropriate Hamiltonian coefficients.

one-dimensional space subject to a 3-delta potential, demonstrating that three distinct types of bound states can arise in such a setup: one for positive and and two for negative values of the central potential coefficients. Interestingly, the first of these states can remain stable following a sudden quench of the central potential to strongly negative values, depending on specific parameters. However, within a narrow parameter regime, this state can become delocalized, despite all potentials being strongly attractive.

A very similar phenomenon is also observed in many-body systems. Specifically, in the case of bosons in a one-dimensional optical lattice with nonlocal interactions (as

described by the extended Bose-Hubbard model), such a quench leads to instability and the *super-evaporation* of the self-bound liquid phase.

Chapter 5

Conclusions and outlook

The aim of this chapter is to present the large-scale outlook of the work presented throughout the thesis and suggest relevant directions in which the work can be extended in the future.

5.1 Conclusions

This thesis is essentially composed of two segments. The first part provided an introduction to the super-Tonks-Girardeau effect, presented mathematical methods that can be applied in its study, and offered arguments suggesting that this effect occurs in one-dimensional many-body systems. Additionally, it was shown that this effect can be applied (or, more precisely, has already been applied in a series of experiments) to carry out the so-called pumping process, through which highly excited states can be generated. These states, due to their particular nature, exhibit a remarkable resistance to thermalization. This chapter presents a theoretical explanation of this phenomenon, along with a discussion of the intriguing properties of the excited states that can be accessed through this process.

The second part presents the results of a separate project, which aim was to investigate the behavior of systems that, in addition to contact interactions, also exhibit non-local interactions. These interactions can give rise to complex self-bound states such as quantum droplets or, in optical lattices, self-bound analogues of the Mott insulator. By employing a combination of analytical methods, ab initio numerical simulations, and approximate descriptions of the system in the thermodynamic limit based on perturbation theory, we

demonstrated that in such systems, the states identified as quantum droplets do not exhibit typical super-Tonks-Girardeau effect, still. Interestingly, following a super-Tonks-Girardeau-like quench, these droplets do not collapse, as might be anticipated, but instead gradually evaporate.

5.2 Outlook

This dissertation serves as a summary of the main branch of my many-year research and, hopefully, will prove useful to those just beginning their adventure with quantum many-body physics and to those interested in the super-Tonks-Girardeau effect. Concerning the latter, there appears to be a wealth of open questions in this field. The rapid development of techniques for trapping and manipulating ultracold atomic systems, cooled to nanokelvin temperatures and composed not of millions or thousands, but now of just hundreds or dozens of atoms in sophisticated trap geometries, continually pushes the boundaries of technology, laying the foundation for a novel area of applied science: *atomtronics* [97, 98, 99].

Concurrently, as the complexity of experimentally accessible quantum systems increases, subtle and often highly counterintuitive many-body effects are becoming of a great significance. Two examples of such phenomena — pumping and super-evaporation — constitute the core focus of this dissertation. Their existence presents both a technological challenge and a source of physical intrigue. For instance, the narrow parameter window described in a context of super-evaporation, where the ground state of a repulsive system lacks a superpartner in the form of a corresponding sTG state, could pose a frustrating puzzle for an unsuspecting experimentalist: for no apparent reason, the self-bound state might sometimes evaporate and sometimes remain stable. On the other hand, these delicate processes also open up new possibilities for controlling matter: the pumping protocol can be applied to produce a strongly correlated ideal Bose gas — a system with potential applications in quantum metrology.

As in other fields of science, we must acknowledge the inherent uncertainty regarding the ultimate fruits of this research. It may lead to breakthrough discoveries — maybe in medicine, clean energy or more powerful computational technologies, or, perhaps. Or, it may yield no practical outcomes at all. What remains certain, however, is that progress along this path will demand sustained and rigorous effort, both from theoretical and experimental sides. Such

commitment will be crucial not only to avoid unforeseen technological limitations but also to uncover any hidden “holy grails“ that may lie ahead.

Based on my experience gained during the research presented in this thesis, I am able to identify several topics whose further investigation could meaningfully contribute to the broader advancement of atomtronics. For the sake of clarity, a selection of the most significant among them is presented below:

- In the present study, we focused on analyzing the system’s dynamics under a symmetric interaction quench, defined as a sudden change in the interaction strength to a value equal in magnitude but opposite in sign. However, in many relevant contexts, it would be of significant interest to investigate the system’s response to asymmetric quenches or quenches starting from interactions that are not strongly repulsive. Although this direction has been partially explored in [25], the problem remains open and important—particularly with regard to identifying the parameter regimes in which the system retains its dynamical stability.
- Another promising avenue of inquiry concerns the peculiar interatomic correlations observed in the states emerging in pumping process (see Fig. 3.18). In contrast to standard fermionization under strong repulsive interactions (Tonks-Girardeau states) — where particles tend to maximize their spatial separation and coherence decays with distance — the behavior in the fermionized regime of an ideal Bose gas is notably different. In particular, the second-order correlation function reveals pronounced bunching behavior, evidenced by correlation maxima, alongside a rapid decay of first-order correlation function. Such behavior is highly counterintuitive in a noninteracting Bose gas and encourage deeper investigation.
- Another open question concerns the feasibility of implementing topological pumping in systems confined by harmonic trapping potentials. Some existing theoretical works [24, 100] and recent experimental realizations [43, 41, 42] indicate that such pumping should indeed be achievable. However, it is unlikely to be accompanied by the fermionization of an ideal Bose gas, as was observed in systems with periodic boundary conditions.
- A further line of study concerns the role of nonlocal interactions in the stability and dynamics of pumping procedure. Experimental evidence suggests that systems with purely short-range interactions may lack the stability required to complete a full pumping cycle. This issue could be mitigated by employing particles that, in addition to quenched contact interactions,

also exhibit weak, repulsive nonlocal forces. A detailed analysis of how such long-range interactions influence the pumping mechanism remains an open and compelling question.

- In the context of super-evaporation, we observe that not only the liquid phase is susceptible to evaporation following a quench of on-site interactions. Parts of the system that initially exhibit self-bound Mott Insulator phase may also undergo evaporation. A detailed description of this transition could yield valuable insights into the underlying mechanisms driving the evaporation process.
- Finally, the consequences of an sTG quench in systems with continuous geometries remain largely unexplored. It would be particularly interesting to determine whether quantum droplets in quasi-1D setups remain stable or undergo evaporation following such a quench. Preliminary analysis presented in Sec. 4.1 suggests that a behavior analogous to that observed in the Bose-Hubbard model may occur in this setting as well, but a more rigorous study is needed to confirm this.

I hope this thesis shows both the beauty and the challenges of quantum many-body physics, and will help future researchers in their scientific pursuits.

Bibliography

[1] M. Planck, "Ueber das Gesetz der Energieverteilung im Normalspectrum," *Ann. Phys.*, vol. 309, pp. 553–563, Jan. 1901.

[2] Bose, "Plancks Gesetz und Lichtquantenhypothese," *Z. Phys.*, vol. 26, pp. 178–181, Dec. 1924.

[3] W. Pauli, "Über den Zusammenhang des Abschlusses der Elektronengruppen im Atom mit der Komplexstruktur der Spektren," *Z. Phys.*, vol. 31, pp. 765–783, Feb. 1925.

[4] E. Schrödinger, "Quantisierung als eigenwertproblem," *Annalen der Physik*, vol. 384, no. 4, pp. 361–376, 1926.

[5] E. Schrödinger, "Über das verhältnis der heisenberg-bornschen quantenmechanik zu der meinen," *Annalen der Physik*, vol. 384, no. 8, pp. 734–756, 1926.

[6] R. Jastrow, "Many-Body Problem with Strong Forces," *Phys. Rev.*, vol. 98, pp. 1479–1484, June 1955.

[7] R. B. Dingle, "LI. The zero-point energy of a system of particles," *London, Edinburgh, and Dublin Philosophical Magazine and Journal of Science*, May 1949.

[8] W. L. McMillan, "Ground state of liquid he^4," *Phys. Rev.*, vol. 138, pp. A442–A451, Apr 1965.

[9] W. M. C. Foulkes, L. Mitas, R. J. Needs, and G. Rajagopal, "Quantum monte carlo simulations of solids," *Rev. Mod. Phys.*, vol. 73, pp. 33–83, Jan 2001.

[10] L. P. Pitaevskii, "Vortex lines in an imperfect Bose gas," *Sov. Phys. JETP*, vol. 13, p. 646, 1960. [Zh. Eksp. Teor. Fiz., **40**, 451 (1961)].

[11] E. P. Gross, "Structure of a quantized vortex in boson systems," *Nuovo Cim.*, vol. 20, pp. 454–477, May 1961.

[12] M. Girardeau, "Relationship between systems of impenetrable bosons and fermions in one dimension," *J. Math. Phys.*, vol. 1, p. 516–523, Nov. 1960.

[13] E. H. Lieb and W. Liniger, "Exact analysis of an interacting Bose gas. I. The general solution and the ground state," *Phys. Rev.*, vol. 130, pp. 1605–1616, 5 1963.

[14] E. H. Lieb, "Exact analysis of an interacting Bose gas. II. The excitation spectrum," *Phys. Rev.*, vol. 130, pp. 1616–1624, 5 1963.

[15] H. Bethe, "Zur theorie der metalle. i. eigenwerte und eigenfunktionen der linearen atomkette," *Zeitschrift für Physik*, vol. 71, no. 3-4, pp. 205–226, 1931.

[16] J. B. McGuire, "Study of Exactly Soluble One-Dimensional N-Body Problems," *J. Math. Phys.*, vol. 5, pp. 622–636, May 1964.

[17] G. E. Astrakharchik, J. Boronat, J. Casulleras, and S. Giorgini, "Beyond the Tonks-Girardeau gas: Strongly correlated regime in quasi-one-dimensional Bose gases," *Phys. Rev. Lett.*, vol. 95, p. 190407, Nov 2005.

[18] M. Srednicki, "Chaos and quantum thermalization," *Phys. Rev. E*, vol. 50, pp. 888–901, Aug. 1994.

[19] L. D'Alessio, Y. Kafri, A. Polkovnikov, and M. Rigol, "From quantum chaos and eigenstate thermalization to statistical mechanics and thermodynamics," *Adv. Phys.*, May 2016.

[20] I. E. Mazets and J. Schmiedmayer, "Thermalization in a quasi-one-dimensional ultracold bosonic gas," *New J. Phys.*, vol. 12, p. 055023, May 2010.

[21] Y. Tang, W. Kao, K.-Y. Li, S. Seo, K. Mallayya, M. Rigol, S. Gopalakrishnan, and B. L. Lev, "Thermalization near Integrability in a Dipolar Quantum Newton's Cradle," *Phys. Rev. X*, vol. 8, p. 021030, May 2018.

[22] E. A. Donley, N. R. Claussen, S. L. Cornish, J. L. Roberts, E. A. Cornell, and C. E. Wieman, "Dynamics of collapsing and exploding Bose–Einstein condensates," *Nature*, vol. 412, pp. 295–299, 2001.

[23] M. T. Batchelor, M. Bortz, X. W. Guan, and N. Oelkers, "Evidence for the super

Tonks–Girardeau gas," *J. Stat. Mech.: Theory Exp.*, vol. 2005, p. L10001, Oct. 2005.

[24] E. Tempfli, S. Zöllner, and P. Schmelcher, "Excitations of attractive 1D bosons: binding versus fermionization," *New J. Phys.*, vol. 10, p. 103021, Oct. 2008.

[25] S. Chen, L. Guan, X. Yin, Y. Hao, and X.-W. Guan, "Transition from a Tonks-Girardeau gas to a super-Tonks-Girardeau gas as an exact many-body dynamics problem," *Phys. Rev. A*, vol. 81, p. 031609, Mar. 2010.

[26] M. D. Girardeau and G. E. Astrakharchik, "Wave functions of the super-Tonks-Girardeau gas and the trapped one-dimensional hard-sphere Bose gas," *Phys. Rev. A*, vol. 81, p. 061601, June 2010.

[27] M. D. Girardeau and G. E. Astrakharchik, "Super-Tonks-Girardeau State in an Attractive One-Dimensional Dipolar Gas," *Phys. Rev. Lett.*, vol. 109, p. 235305, Dec. 2012.

[28] M. Łebek, A. Syrwid, P. T. Grochowski, and K. Rzążewski, "Repulsive dynamics of strongly attractive one-dimensional quantum gases," *Phys. Rev. A*, vol. 105, p. L011303, Jan. 2022.

[29] M. Greiner, I. Bloch, O. Mandel, T. W. Hänsch, and T. Esslinger, "Exploring Phase Coherence in a 2D Lattice of Bose-Einstein Condensates," *Phys. Rev. Lett.*, vol. 87, p. 160405, Oct. 2001.

[30] M. Greiner, I. Bloch, T. W. Hänsch, and T. Esslinger, "Magnetic transport of trapped cold atoms over a large distance," *Phys. Rev. A*, vol. 63, p. 031401, Feb. 2001.

[31] I. Bloch, J. Dalibard, and W. Zwerger, "Many-body physics with ultracold gases," *Rev. Mod. Phys.*, vol. 80, pp. 885–964, July 2008.

[32] B. Paredes, A. Widera, V. Murg, O. Mandel, S. Fölling, I. Cirac, G. V. Shlyapnikov, T. W. Hänsch, and I. Bloch, "Tonks–Girardeau gas of ultracold atoms in an optical lattice," *Nature*, vol. 429, pp. 277–281, May 2004.

[33] T. Kinoshita, T. Wenger, and D. S. Weiss, "Observation of a One-Dimensional Tonks-Girardeau Gas," *Science*, vol. 305, pp. 1125–1128, Aug. 2004.

[34] S. Eckel, J. G. Lee, F. Jendrzejewski, N. Murray, C. W. Clark, C. J. Lobb, W. D. Phillips, M. Edwards, and G. K. Campbell, "Hysteresis in a quantized superfluid

'atomtronic' circuit," *Nature*, vol. 506, pp. 200–203, Feb. 2014.

[35] E. Haller, R. Hart, M. J. Mark, J. G. Danzl, L. Reichsöllner, M. Gustavsson, M. Dalmonte, G. Pupillo, and H.-C. Nägerl, "Pinning quantum phase transition for a Luttinger liquid of strongly interacting bosons," *Nature*, vol. 466, pp. 597–600, July 2010.

[36] E. Haller, M. Gustavsson, M. J. Mark, J. G. Danzl, R. Hart, G. Pupillo, and H.-C. Nägerl, "Realization of an Excited, Strongly Correlated Quantum Gas Phase," *Science*, vol. 325, pp. 1224–1227, Sept. 2009.

[37] S. Sinha and L. Santos, "Cold Dipolar Gases in Quasi-One-Dimensional Geometries," *Phys. Rev. Lett.*, vol. 99, p. 140406, Oct. 2007.

[38] F. Deuretzbacher, J. C. Cremon, and S. M. Reimann, "Ground-state properties of few dipolar bosons in a quasi-one-dimensional harmonic trap," *Phys. Rev. A*, vol. 81, p. 063616, June 2010.

[39] F. Deuretzbacher, J. C. Cremon, and S. M. Reimann, "Erratum: Ground-state properties of few dipolar bosons in a quasi-one-dimensional harmonic trap [Phys. Rev. A 81, 063616 (2010)]," *Phys. Rev. A*, vol. 87, p. 039903, Mar. 2013.

[40] L. Chomaz, I. Ferrier-Barbut, F. Ferlaino, B. Laburthe-Tolra, B. L. Lev, and T. Pfau, "Dipolar physics: a review of experiments with magnetic quantum gases," *Rep. Prog. Phys.*, vol. 86, p. 026401, Dec. 2022.

[41] K.-Y. Li, Y. Zhang, K. Yang, K.-Y. Lin, S. Gopalakrishnan, M. Rigol, and B. L. Lev, "Rapidity and momentum distributions of one-dimensional dipolar quantum gases," *Phys. Rev. A*, vol. 107, p. L061302, June 2023.

[42] K. Yang, Y. Zhang, K.-Y. Li, K.-Y. Lin, S. Gopalakrishnan, M. Rigol, and B. L. Lev, "Phantom energy in the nonlinear response of a quantum many-body scar state," *arXiv*, Aug. 2023.

[43] W. Kao, K.-Y. Li, K.-Y. Lin, S. Gopalakrishnan, and B. L. Lev, "Topological pumping of a 1D dipolar gas into strongly correlated prethermal states," *Science*, vol. 371, pp. 296–300, Jan. 2021.

[44] A. Shabat and V. Zakharov, "Exact theory of two-dimensional self-focusing and one-dimensional self-modulation of waves in nonlinear media," *Sov. Phys. JETP*, vol. 34, no. 1, p. 62, 1972.

[45] D. S. Petrov, "Quantum mechanical stabilization of a collapsing bose-bose mixture," *Phys. Rev. Lett.*, vol. 115, p. 155302, 2015.

[46] C. R. Cabrera, L. Tanzi, J. Sanz, B. Naylor, P. Thomas, P. Cheiney, and L. Tarruell, "Quantum liquid droplets in a mixture of bose-einstein condensates," *Science*, vol. 359, no. 6373, pp. 301–304, 2018.

[47] H. Kadau, M. Schmitt, M. Wenzel, C. Wink, T. Maier, I. Ferrier-Barbut, and T. Pfau, "Observing the rosensweig instability of a quantum ferrofluid," *Nature*, vol. 530, pp. 194–197, 2016.

[48] I. Ferrier-Barbut, H. Kadau, M. Schmitt, M. Wenzel, and T. Pfau, "Observation of quantum droplets in a strongly dipolar Bose gas," *Phys. Rev. Lett.*, vol. 116, p. 215301, May 2016.

[49] G. Semeghini, G. Ferioli, L. Masi, C. Mazzinghi, L. Wolswijk, F. Minardi, M. Modugno, G. Modugno, M. Inguscio, and M. Fattori, "Self-Bound Quantum Droplets of Atomic Mixtures in Free Space," *Phys. Rev. Lett.*, vol. 120, p. 235301, June 2018.

[50] F. Böttcher, J.-N. Schmidt, J. Hertkorn, K. S. H. Ng, S. D. Graham, M. Guo, T. Langen, and T. Pfau, "New states of matter with fine-tuned interactions: quantum droplets and dipolar supersolids," *Reports on Progress in Physics*, vol. 84, p. 012403, dec 2020.

[51] R. Ołdziejewski, W. Górecki, K. Pawłowski, and K. Rzążewski, "Strongly correlated quantum droplets in quasi-1D dipolar Bose gas," *Phys. Rev. Lett.*, vol. 124, p. 090401, Mar 2020.

[52] J. Kopyciński, M. Łebek, M. Marciniak, R. Ołdziejewski, W. Górecki, and K. Pawłowski, "Beyond Gross-Pitaevskii equation for 1D gas: quasiparticles and solitons," *SciPost Phys.*, vol. 12, p. 023, Jan. 2022.

[53] W. E. ARNOLDI, "The principle of minimized iterations in the solution of the matrix eigenvalue problem," *Quarterly of Applied Mathematics*, vol. 9, no. 1, pp. 17–29, 1951.

[54] C. Lanczos, "An iteration method for the solution of the eigenvalue problem of linear differential and integral operators," *J.Res.Natl.Bur.Stand.B*, vol. 45, pp. 255–282, 1950.

[55] S. R. White, "Density matrix formulation for quantum renormalization

groups," *Phys. Rev. Lett.*, vol. 69, pp. 2863–2866, Nov. 1992.

[56] S. R. White, "Density-matrix algorithms for quantum renormalization groups," *Phys. Rev. B*, vol. 48, pp. 10345–10356, Oct. 1993.

[57] G. Catarina and B. Murta, "Density-matrix renormalization group: a pedagogical introduction," *Eur. Phys. J. B*, vol. 96, pp. 1–30, Aug. 2023.

[58] U. Schollwöck, "The density-matrix renormalization group," *Rev. Mod. Phys.*, vol. 77, pp. 259–315, Apr. 2005.

[59] U. Schollwöck, "The density-matrix renormalization group in the age of matrix product states," *Ann. Phys.*, vol. 326, pp. 96–192, Jan. 2011.

[60] A. Haller, "M at r i x p r o d u c t s tat e s a variational approach to strongly correlated systems," Master's thesis, Johannes Gutenberg University Mainz, 2014.

[61] M. Ganahl, J. Beall, M. Hauru, A. G. M. Lewis, T. Wojno, J. H. Yoo, Y. Zou, and G. Vidal, "Density Matrix Renormalization Group with Tensor Processing Units," *PRX Quantum*, vol. 4, p. 010317, Feb. 2023.

[62] B. Bauer, L. D. Carr, H. G. Evertz, A. Feiguin, J. Freire, S. Fuchs, L. Gamper, J. Gukelberger, E. Gull, S. Guertler, A. Hehn, R. Igarashi, S. V. Isakov, D. Koop, P. N. Ma, P. Mates, H. Matsuo, O. Parcollet, G. Pawłowski, J. D. Picon, L. Pollet, E. Santos, V. W. Scarola, U. Schollwöck, C. Silva, B. Surer, S. Todo, S. Trebst, M. Troyer, M. L. Wall, P. Werner, and S. Wessel, "The ALPS project release 2.0: open source software for strongly correlated systems," *J. Stat. Mech.: Theory Exp.*, vol. 2011, p. P05001, May 2011.

[63] M. Dolfi, B. Bauer, S. Keller, A. Kosenkov, T. Ewart, A. Kantian, T. Giamarchi, and M. Troyer, "Matrix product state applications for the ALPS project," *Comput. Phys. Commun.*, vol. 185, pp. 3430–3440, Dec. 2014.

[64] M. Fishman, S. White, and E. M. Stoudenmire, "The ITensor Software Library for Tensor Network Calculations," *SciPost Phys. Codebases*, p. 004, Aug. 2022.

[65] E. R. Davidson, "The iterative calculation of a few of the lowest eigenvalues and corresponding eigenvectors of large real-symmetric matrices," *J. Comput. Phys.*, vol. 17, pp. 87–94, Jan. 1975.

[66] M. Fishman, S. R. White, and E. M. Stoudenmire, "The ITensor Software Library

for Tensor Network Calculations," *SciPost Phys. Codebases*, p. 4, 2022.

[67] R. Orús, "A practical introduction to tensor networks: Matrix product states and projected entangled pair states," *Annals of Physics*, vol. 349, pp. 117–158, 2014.

[68] S. Montangero, *Introduction to Tensor Network Methods*. Cham, Switzerland: Springer International Publishing, 2018.

[69] J. Haegeman, J. I. Cirac, T. J. Osborne, I. Pižorn, H. Verschelde, and F. Verstraete, "Time-Dependent Variational Principle for Quantum Lattices," *Phys. Rev. Lett.*, vol. 107, p. 070601, Aug. 2011.

[70] B. Kloss, Y. B. Lev, and D. Reichman, "Time-dependent variational principle in matrix-product state manifolds: Pitfalls and potential," *Phys. Rev. B*, vol. 97, p. 024307, Jan. 2018.

[71] M. Yang and S. R. White, "Time-dependent variational principle with ancillary Krylov subspace," *Phys. Rev. B*, vol. 102, p. 094315, Sept. 2020.

[72] M. Marciniak, G. E. Astrakharchik, K. Pawłowski, and B. Juliá-Díaz, "Fermionizing the ideal Bose gas via topological pumping," *arXiv*, Apr. 2025.

[73] G. E. Astrakharchik, J. Boronat, J. Casulleras, and S. Giorgini, "Beyond the Tonks-Girardeau Gas: Strongly Correlated Regime in Quasi-One-Dimensional Bose Gases," *Phys. Rev. Lett.*, vol. 95, p. 190407, Nov. 2005.

[74] M. Girardeau, "Relationship between systems of impenetrable bosons and fermions in one dimension," *J. Math. Phys.*, vol. 1, pp. 516–523, 11 1960.

[75] T. Dorlas, "Orthogonality and completeness of the bethe ansatz eigenstates of the nonlinear schroedinger model," *Communications in Mathematical Physics*, vol. 154, p. p. 347–376., Jun 1993.

[76] J. C. Zill, T. M. Wright, K. V. Kheruntsyan, T. Gasenzer, and M. J. Davis, "A coordinate Bethe ansatz approach to the calculation of equilibrium and nonequilibrium correlations of the one-dimensional Bose gas," *New J. Phys.*, vol. 18, p. 045010, Apr. 2016.

[77] A. Lenard, "Momentum Distribution in the Ground State of the One-Dimensional System of Impenetrable Bosons," *J. Math. Phys.*, vol. 5,

pp. 930–943, July 1964.

[78] M. Olshanii and V. Dunjko, "Short-Distance Correlation Properties of the Lieb-Liniger System and Momentum Distributions of Trapped One-Dimensional Atomic Gases," *Phys. Rev. Lett.*, vol. 91, p. 090401, Aug. 2003.

[79] A. Takács, Y. Zhang, P. Calabrese, J. Dubail, M. Rigol, and S. Scopa, "One-body correlations and momentum distributions of trapped one-dimensional Bose gases at finite temperature," *Phys. Rev. A*, vol. 111, p. 033317, Mar. 2025.

[80] M. T. Batchelor, X. W. Guan, N. Oelkers, and C. Lee, "The 1D interacting Bose gas in a hard wall box," *J. Phys. A: Math. Gen.*, vol. 38, p. 7787, Aug. 2005.

[81] S. Chen, X.-W. Guan, X. Yin, L. Guan, and M. T. Batchelor, "Realization of effective super Tonks-Girardeau gases via strongly attractive one-dimensional Fermi gases," *Phys. Rev. A*, vol. 81, p. 031608, 3 2010.

[82] M. Marciniak, M. Łebek, J. Kopyciński, W. Górecki, R. Ołdziejewski, and K. Pawłowski, "Super-Tonks-Girardeau quench in the extended Bose-Hubbard model," *Phys. Rev. A*, vol. 108, p. 043304, Oct. 2023.

[83] K. M. Rabe and U. V. Waghmare, "Localized basis for effective lattice Hamiltonians: Lattice Wannier functions," *Phys. Rev. B*, vol. 52, pp. 13236–13246, Nov. 1995.

[84] D. Jaksch, C. Bruder, J. I. Cirac, C. W. Gardiner, and P. Zoller, "Cold Bosonic Atoms in Optical Lattices," *Phys. Rev. Lett.*, vol. 81, pp. 3108–3111, Oct. 1998.

[85] M. Greiner, O. Mandel, T. Esslinger, T. W. Hänsch, and I. Bloch, "Quantum phase transition from a superfluid to a mott insulator in a gas of ultracold atoms," *Nature*, vol. 415, Jan 2002.

[86] I. Bloch, J. Dalibard, and W. Zwerger, "Many-body physics with ultracold gases," *Rev. Mod. Phys.*, vol. 80, pp. 885–964, Jul 2008.

[87] I. Morera, R. Ołdziejewski, G. E. Astrakharchik, and B. Juliá-Díaz, "Superexchange liquefaction of strongly correlated lattice dipolar bosons," *Phys. Rev. Lett.*, vol. 130, p. 023602, 1 2023.

[88] T. Sowiński, O. Dutta, P. Hauke, L. Tagliacozzo, and M. Lewenstein, "Dipolar molecules in optical lattices," *Phys. Rev. Lett.*, vol. 108, p. 115301, Mar 2012.

[89] M. Maik, P. Hauke, O. Dutta, M. Lewenstein, and J. Zakrzewski, "Density-dependent tunneling in the extended bose–hubbard model," *New Journal of Physics*, vol. 15, p. 113041, nov 2013.

[90] R. Ołdziejewski, W. Górecki, K. Pawłowski, and K. Rzażewski, "Strongly correlated quantum droplets in quasi-1D dipolar Bose gas," *Phys. Rev. Lett.*, vol. 124, p. 090401, Mar 2020.

[91] D. Petrov and G. Astrakharchik, "Ultradilute low-dimensional liquids," *Phys. Rev. Lett.*, vol. 117, p. 100401, 9 2016.

[92] M. Valiente and D. Petrosyan, "Scattering resonances and two-particle bound states of the extended Hubbard model," *J. Phys. B*, vol. 42, p. 121001, 6 2009.

[93] M. V. Cifuentes, *Few quantum particles on one dimensional lattices*. PhD thesis, Humboldt-Universität zu Berlin, Mathematisch-Naturwissenschaftliche Fakultät I, 2010.

[94] M. T. Batchelor, M. Bortz, X. W. Guan, and N. Oelkers, "Evidence for the super Tonks–Girardeau gas," *J. Stat. Mech.*, vol. 2005, pp. L10001–L10001, 10 2005.

[95] M. Yang and S. R. White, "Time-dependent variational principle with ancillary krylov subspace," *Phys. Rev. B*, vol. 102, p. 094315, Sep 2020.

[96] M. A. Cazalilla, "One-dimensional optical lattices and impenetrable bosons," *Phys. Rev. A*, vol. 67, p. 053606, May 2003.

[97] B. T. Seaman, M. Krämer, D. Z. Anderson, and M. J. Holland, "Atomtronics: Ultracold-atom analogs of electronic devices," *Phys. Rev. A*, vol. 75, p. 023615, Feb. 2007.

[98] R. A. Pepino, J. Cooper, D. Z. Anderson, and M. J. Holland, "Atomtronic Circuits of Diodes and Transistors," *Phys. Rev. Lett.*, vol. 103, p. 140405, Sept. 2009.

[99] L. Amico, M. Boshier, G. Birkl, A. Minguzzi, C. Miniatura, L.-C. Kwek, D. Aghamalyan, V. Ahufinger, D. Anderson, N. Andrei, A. S. Arnold, M. Baker, T. A. Bell, T. Bland, J. P. Brantut, D. Cassettari, W. J. Chetcuti, F. Chevy, R. Citro, S. De Palo, R. Dumke, M. Edwards, R. Folman, J. Fortagh, S. A. Gardiner, B. M. Garraway, G. Gauthier, A. Günther, T. Haug, C. Hufnagel, M. Keil, P. Ireland, M. Lebrat, W. Li, L. Longchambon, J. Mompart, O. Morsch, P. Naldesi, T. W. Neely, M. Olshanii, E. Orignac, S. Pandey, A. Pérez-Obiol, H. Perrin, L. Piroli, J. Polo, A. L. Pritchard, N. P. Proukakis, C. Rylands, H. Rubinsztein-Dunlop, F. Scazza,

S. Stringari, F. Tosto, A. Trombettoni, N. Victorin, W. v. Klitzing, D. Wilkowski, K. Xhani, and A. Yakimenko, “Roadmap on Atomtronics: State of the art and perspective,” *AVS Quantum Sci.*, vol. 3, Sept. 2021.

[100] P. D’Amico and M. Rontani, “Three interacting atoms in a one-dimensional trap: a benchmark system for computational approaches,” *J. Phys. B: At. Mol. Opt. Phys.*, vol. 47, p. 065303, Feb. 2014.